UNIVERSITÀ DI PARMA

UNIVERSITÀ DEGLI STUDI DI PARMA

DOTTORATO DI RICERCA IN
INGEGNERIA INDUSTRIALE

CICLO XXXVII

On Singularities in Linear Elasticity

Coordinatore:

Chiar.mo. Prof. Gianni Royer-Carfagni

Tutore:

Chiar.mo. Prof. Gianni Royer-Carfagni

Dottorando: **Salman Zandekarimi**

ANNI ACCADEMICI 2021/2022-2023/2024

UNIVERSITÀ DI PARMA

UNIVERSITÀ DEGLI STUDI DI PARMA

PH.D. COURSE IN
INDUSTRIAL ENGINEERING

XXXVII CYCLE

On Singularities in Linear Elasticity

Ph.D. Course Coordinator:

Cl. Prof. Gianni Royer-Carfagni

Thesis Advisor:

Cl. Prof. Gianni Royer-Carfagni

Candidate: **Salman Zandekarimi**

ACADEMIC YEARS 2021/2022-2023/2024

I would like to dedicate this thesis to my beloved wife, whose unwavering support and love made this journey possible.

I hereby declare that except where specific reference is made to the work of others, the contents of this dissertation are original and have not been submitted in whole or in part for consideration for any other degree or qualification in this, or any other university. This dissertation is my own work and contains nothing which is the outcome of work done in collaboration with others, except as specified in the text and Acknowledgements. This dissertation contains fewer than thirty thousand words, including appendices, bibliography, footnotes, tables and equations and has fewer than thirty figures.

I am profoundly grateful to my esteemed supervisor, Professor Gianni Royer-Carfagni, whose insightful guidance, unwavering support, and intellectual rigor have been instrumental in the completion of this thesis. His mentorship has been a beacon of inspiration throughout this academic journey.

Abstract

This thesis investigates stress singularities within the framework of linear elasticity, focusing on their occurrence, interpretation, and implications in two fundamental cases: an infinite elastic wedge under a moment at its vertex and an elastic disk subjected to sectorial thermal expansion. Stress singularities, where stresses theoretically approach infinity, represent critical regions that influence material failure. Although singularities are mathematical idealizations, they highlight the limitations of classical elasticity and provide insights into real-world structural behavior.

The first study addresses the wedge problem, where an infinite elastic wedge is subjected to a concentrated couple at its vertex. Classical solutions, such as Carothers' formulation, predict a quadratic singularity in the stress field. However, at a critical wedge angle, this solution exhibits spurious behavior known as the wedge paradox. This work proposes a novel interpretation of the stress states by reframing the problem in terms of auxiliary wedges and dipole forces, offering a generalized solution that remains valid for all wedge angles. This approach resolves the paradox by demonstrating that the singular stress state corresponds to a system of dipoles with no resultant moment at the critical angle.

The second study explores thermal stress singularities in an infinite elastic disk with a sector experiencing uniform temperature rise. The thermal mismatch between the heated sector and the surrounding material generates stress discontinuities, leading to a logarithmic singularity at the sector boundary. While classical analysis of this infinite geometry yields divergent solutions, introducing a finite length scale, such as the disk radius, constrains the stress field. The study employs dislocation arrays to model thermal mismatches and validates the theoretical predictions using finite element simulations. This approach bridges the gap between idealized infinite models and finite geometries encountered in engineering applications, such as glass panels subjected to differential heating.

This research emphasizes that stress singularities, while mathematically infinite, can be interpreted to provide physically meaningful insights into structural reliability and failure mechanisms. By combining analytical, numerical, and dimensional analysis techniques, the study offers robust frameworks for addressing singularities in practical engineering contexts, including fracture mechanics, thermal stress analysis, and material design.

Contents

List of Figures

List of Tables

Chapter 1

Introduction

1.1 Stress singularities in theory of elasticity

One of the main goals of the linear theories of elasticity is to predict the initiation and propagation of the failure in elastic medias. Paramount importance of failure in structures made of different materials and subjected to complex thermal and/or mechanical loads is simply in direct connection to the safety of human and financial resources. Failures of components and structures during service have become increasingly common across various industries, often occurring without prior warning. While some failures may be minor, others can have severe repercussions, including:

- Loss of lives
- Personnel injuries
- Property damage
- Complete plant shutdowns
- Disruption of production
- Environmental issues, such as hazardous material release
- Costly and lengthy legal disputes, which can harm the reputation of manufacturers and the reliability of their products.

Catastrophic effects of failure in variety of structures from electronic devices to bridges and airplanes have been well documented during the past decades [1]. Singular points and their importance in theory of elasticity and consequently in applied engineering, as the stem of failure initiation, will be the departure point of the current study. Study of singularity in the realm of linear elasticity can be started by giving a definition of a singular stress state and categorizing different types of singular problems.

Stress singularities refer to points, lines or regions of an elastic body over that the components of the stress become unbounded. Here, it should be noticed that according to this idealistic classical definition, stress singularities are not real phenomena and indicate the limits of elasticity theory and idealized models because infinite stresses are physically meaningless. Since, they are the outcomes of the mathematical analysis, they should be taken into consideration when those mathematical models are supposed to be used in real cases [2].

1.2 Singularity sources

The principal sources of singularities can be addressed as load, boundary conditions, elastic body's shape and material discontinuities [3]. Another type of singularity that should be taken into account, in some cases, excluded from the general sources of singularities, is related to dislocation problems. Behavior of this kind of singular problems stems from the discontinuities in the displacement field and later in the present work, will be discussed in detail. Stress near a singularity often follows a power-law behavior, such as:

$$\sigma \sim 1/r^{\alpha}, \tag{1.1}$$

where σ and r stand correspondingly for the stress, distance from the singularity and α is a parameter related to the geometry and loading. Amongst various types of stress singularities those involving 'Concentrated Loads' holds significant importance in the linear theory of elasticity due to its critical role in numerous engineering applications. As a result, this topic has garnered considerable attention from researchers and engineers alike. Furthermore, the study of concentrated loads extends beyond their direct applications, serving as a foundation for understanding and generalizing more complex cases involving singularities in elastic materials.

In a notable two-part study, Sinclair [2, 4] explored stress singularities arising from concentrated loads within the framework of classical elasticity. This work holds significant importance in the field, as it provides a comprehensive perspective on various stress singularities caused by concentrated loads and proposes strategies to address singular stress fields in both theoretical contexts and engineering applications. Figures 1.1 and 1.2, illustrate two categories of stress singularities related to different types of singularity sources [2].

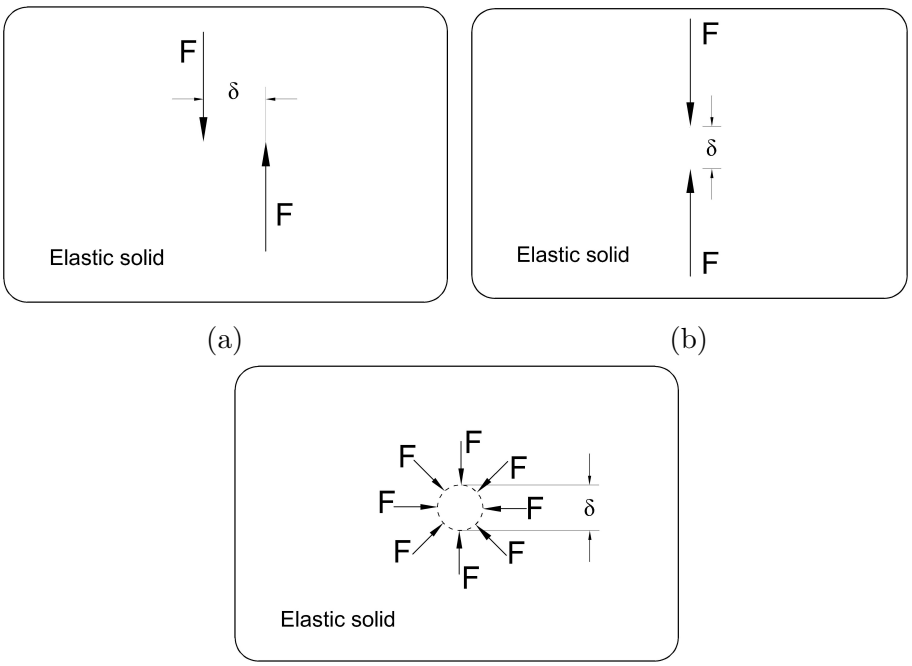

Figure 1.1: Some limiting configurations for doublet states (a) concentrated moment, (b) force doublet without a moment, (c) center of compression (see reference [2]).

Singular loads arise in concentrated loading scenarios where finite stress resultants, such as forces or moments, are applied to regions with negligible dimensions, as illustrated in Figure 1.1. Table 1.1, exhibits singularity orders due to these set of fundamental singularities, where, r indicates the distance from the point of application of a singular load.

Table 1.1: Basic singular loads of classical elasticity [2].

Load type	3D stress state at load ($r \to 0$)	2D stress state at load ($r \to 0$)
Isolated force	ord (r^{-2})	ord (r^{-1})
Doublets	ord (r^{-3})	ord (r^{-2})

The starting point for evaluating the singularity orders of the cases depicted in Figure 1.1 would be stress state due to application of a single force to an elastic body. For a point force, evaluating the tractions over the surface of a small sphere with radius r, centered at the application point, results in a stress product proportional to r^2. Consequently, the stresses are expected to scale as to maintain a finite force as $r \to 0$. Similarly, for a line load, the stresses are anticipated to scale as r^{-1}. For doublet states, which are derived by differentiating their corresponding isolated loads, the expected behavior is r^{-3} in three dimensions and r^{-2} in two dimensions. Nevertheless, achieving these limiting behaviors through sequences of finite stress fields over finite regions requires careful consideration to align with the physical interpretation of singular loads.

Examples of solutions for isolated force problems in three dimensions include Kelvin's (Thomson) solution for a point load in an infinite elastic medium [5], Boussinesq's solution for a normal point load on the surface of an elastic half-space [6], and Mindlin's work on point loads within a half-space [7]. A comprehensive collection of these closed-form solutions is provided in Section 2.1 of Poulos and Davis [8]. Examination of these solutions confirms their agreement with the singularity orders for point loads listed in Table 1.1.

Doublet state examples are illustrated in Figure 1.1. The first example (Figure 1.1a) demonstrates a method to generate a concentrated moment M, achieved by taking the limit as $\delta \to 0$, where δ is the horizontal distance between two vertical forces of magnitude $F = M/\delta$. This concept is adopted in Section 2 of Chapter 5 of the present study. The second configuration (Figure 1.1b) represents a complementary case with no net force or moment in the limit but exhibits a non-trivial stress field when $\delta \to 0$. This requires extending the conventional concept of a load to include "singular loads." The third case (Figure 1.1c) involves a center of compression formed by arranging the second configuration in an angular pattern, which similarly represents a generalized load concept. A formal definition of doublet states is provided in Sternberg and Eubanks [9]. Closed-form solutions for three-dimensional doublet states are available in Love [10], Sternberg and Eubanks [9] also, Turteltaub and Sternberg [11]. For two-dimensional doublet states, solutions can be found in Love [10] and Timoshenko and Goodier [12].

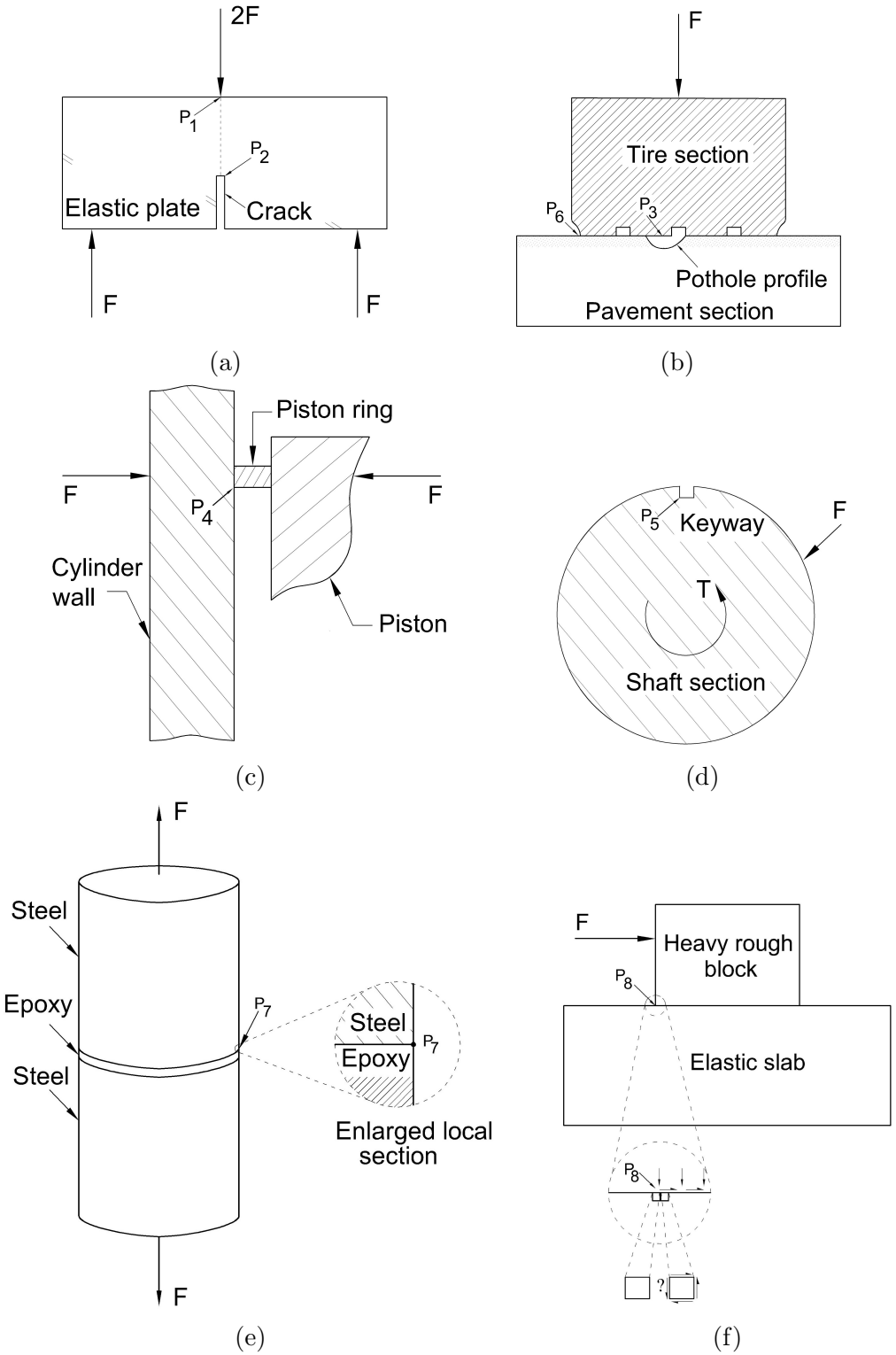

Figure 1.2: Some singular configurations: (a) three-point-bend test piece of fracture mechanics, (b) section through a tire on a relatively rigid pavement, (c) section through a piston with a ring pressed into a cylinder wall, (d) section of a shaft with a stress-free keyway under torsion and lateral loading, (e) adhesive butt joint under tension, (f) rough heavy block sticking to an elastic base (see reference [2]).

Singular loads are often used to represent highly localized forces, such as those experienced beneath a knife edge in a three-point bend test in fracture mechanics (e.g., point P_1 in Figure 1.2a). In this case, the line load serves as one of the set of three components that influence a moment applied to the crack. However, this load is not the primary focus in terms of localized failure potential; instead, the crack tip depicted as P_2 in Figure 1.2a, becomes the critical area of interest.

Figure 1.2a illustrates a cracked elastic plate under three-point bending, exhibiting an inverse-square-root stress singularity at the crack tip (e.g., point P_2). For a crack in a large plate under transverse tension, this singularity can be derived by taking the limit as an elliptical hole becomes a sharp slit, as shown by Inglis [13]. Williams [14] extended this idea, demonstrating the asymptotic stress behavior for angular plates or wedges, which applies to the crack tip in Figure 1.2a. When the plate consists of two bonded elastic materials with a straight interface ahead of the crack (indicated by the dashed line), the stress singularity becomes more complex. The inverse-square-root singularity gains oscillatory multipliers, $\cos(\eta \ln r)$ and $\sin(\eta \ln r)$, which oscillate infinitely as $r \to 0$ if $\eta \neq 0$. Here, η is a material constant dependent on shear modulus μ, and Poisson's ratios ν, of the two materials. For identical materials ($\eta = 0$), the oscillatory effect disappears. Williams [15] first described these oscillatory singularities for interface cracks.

Figure 1.2b focuses on a tire lightly loaded against a stiff pavement at the edge of a pothole, with point P_3 as the area of interest. In the first scenario, where the pavement is icy and frictionless, the setup resembles an elastic half-space being indented by a flat, rigid strip without friction. Sadowsky [16] solved this problem, showing that the stress field near the contact edge has an inverse-square-root singularity, as seen in Table 1.2. This singularity is comparable to that of a crack in a homogeneous material. By reflecting the half-space symmetrically about the strip, the problem becomes equivalent to a full space with stress-free cracks outside the contact area of the strip.

In the second scenario, with a dry surface where the tire adheres perfectly to the pavement, the system mimics a flat, rigid strip adhering to and indenting the elastic half-space. Abramov [17] provided the solution, revealing an inverse-square-root singularity accompanied by oscillatory multipliers (in Table 1.2). Here, the oscillations are determined by the material constant η , derived from Equation (1.2) by taking $\mu_2 \to \infty$, that leads to Equation (1.3).

$$\eta = \frac{1}{2\pi} \ln \frac{\mu_1 + \kappa_1 \mu_2}{\mu_2 + \kappa_2 \mu_1}, \tag{1.2}$$

$$\eta = \frac{1}{2\pi} \ln \kappa, \tag{1.3}$$

Where κ is Kolosov's constant, $\kappa = 3 - 4\nu$ or $(3 - \nu)/(1 + \nu)$ for plane strain or plane stress respectively, ν being Poisson's ratio, μ is the shear modulus and the subscripts distinguish the different materials on each side of the interface crack.

Figure 1.2c illustrates a lubricated piston ring pressed into a cylinder wall, an axisymmetric configuration different from the previous plane strain examples. If the piston ring is assumed to be much stiffer than the cylinder, the stress field near the contact point P_4 exhibits the same inverse-square-root singularity as in the frictionless, flat strip indentation case in Figure 1.2b. On the other hand, if

the ring and cylinder are made of the same material, a weaker singularity arises, as detailed in Table 1.2. This weaker singularity, caused by the inclusion of the ring's deformation, can be determined by solving the relevant eigenvalue equation provided in Dempsey and Sinclair [18].

Figure 1.2d shows a keyway in a shaft under torque and transverse load , with multiple singularities at the 90° reentrant corner (P_5). For torque, the stress singularity has an exponent of 1/3, weaker than the 1/2 for a crack under torsion, as identified by Thomson and Tait [19]. Under transverse loading, two singularities occur: a stronger one for symmetric loading about the bisector of the angle at the reentrant corner and a weaker one for antisymmetric loading. Both are weaker than crack singularities and are derived by Williams [14] using "free-free" wedge conditions for wedge angle of $3\pi/2$.

As the angle at a reentrant corner increases, the singularity strength diminishes and vanishes when the corner becomes a stress-free half-space. However, mixed boundary conditions can retain singularities. For example, in the tire case (Figure 1.2b) at the pavement's outer edge (P_6), perfect adhesion with the rigid pavement creates a right-angled corner in plane strain, with one side stress-free and the other fixed. This produces a singularity described by Knein [20] and alternatively can be obtained from Williams' "clamped-free" wedge solution [14] for wedge angle of $\pi/2$, adapted to plane strain.

A comparable case is seen in the butt joint under tension (Figure 1.2e), where attention focuses on the interface between the steel adherend and the epoxy adhesive near the outer free surface (e.g., point P_7). Although the configuration is axisymmetric, a plane strain analysis remains valid. Given the greater stiffness of steel compared to epoxy, the problem can be modeled as a "clamped-free" right-angled corner in plane strain, as outlined by Williams [14]. Assuming a Poisson's ratio of $\nu = 3/8$ for epoxy, the stress singularity corresponds to the value listed in Table 1.2. The singularity here is weaker than that of the rubber example ($\nu = 0.5$), due to epoxy's lower Poisson's ratio. Interestingly, for $\nu = 0$, such corners no longer exhibit a singularity.

Figure 1.2f illustrates a heavy, rough block under a lateral force, adhering to a horizontal elastic surface. At the point of interest (P_8, highlighted in the close-up), it is assumed that normal stresses cause a discontinuity in the surface shear. This results in a logarithmic stress singularity, with its coefficient proportional to the magnitude of the shear stress discontinuity. This behavior was first described by Kolossoff [21] and can also be derived using auxiliary fields associated with Williams [14], as further developed by Dempsey and Sinclair [22]. While normal stress discontinuities do not produce singularities, shear stress discontinuities on an elastic half-plane do. To illustrate this, consider the two small square elements near the discontinuity, shown in the close-up of Figure 1.2f. The left element maintains force and moment equilibrium without boundary shears, while the right element experiences constant shear stresses. At their intersection, the shear stress mismatch cannot be resolved by any regular elasticity fields known so far.

Table 1.2: Some elastic stress singularities away from singular loads [2].

Singular point in Fig.1.2	Local configuration description	Singular stresses at point ($r \to 0$)
P_2	Crack tip in 3-point bend specimen	ord $\left(r^{-1/2}\right)$
P_2	Interface crack tip in bend specimen	ord $\left(r^{-1/2}\cos(\eta \ln r)\right)$ ord $\left(r^{-\frac{1}{2}}\sin(\eta \ln r)\right)$ see (1.2) for η
P_3	Tire at pothole edge under icy conditions	ord $\left(r^{-1/2}\right)$
P_3	Adhering nylon tire at pothole edge	ord $\left(r^{-1/2}\cos(\eta \ln r)\right)$ ord $\left(r^{-1/2}\sin(\eta \ln r)\right)$ see (1.3) for η
P_4	Edge of piston ring pressed into cylinder wall	ord $\left(r^{-0.23}\right)$
P_5	Reentrant corner in stress-free keyway	ord $\left(\mathrm{Tr}^{-1/3}\right)$ ord $\left(Fr^{-0.46}\right)$ ord $\left(Fr^{-0.09}\right)$
P_6	Edge of adhering rubber tire on pavement	ord $\left(r^{-0.41}\right)$
P_7	Circumference of an epoxy-steel interface	ord $\left(r^{-1/3}\right)$
P_8	Edge of a rough heavy block on an elastic slab	ord $(\ln r)$

1.3 Strategies in facing stress singularities

A fundamental question that naturally arises is: how should configurations involving stress singularities be managed to ensure structural reliability? Addressing this concern begins with the essential step of recognizing when a stress singularity is present. However, identifying such singularities is not always straightforward, particularly in the context of real-world engineering components. This complexity necessitates strategies either to **remove** these singularities or to **interpret** their implications in a meaningful way.

In many cases, the complexity of these components demands numerical methods, such as finite element analysis (FEA), for stress evaluation. Unlike analytical solutions, which can often reveal the singular behavior of stress fields through direct observation, numerical methods may obscure these features, making their detection less apparent.

Despite these challenges, it is crucial for stress analysts to develop an awareness of potential singular stress fields in their analyses. Failure to recognize such conditions can lead to critical oversights in the design and assessment of structures, compromising their reliability and safety. The ability to identify and appropriately address these singularities is a key aspect of ensuring robust engineering solutions.

1.3.1 Removing nonphysical stress singularities

The removal of stress singularities primarily involves improving the physical modelling of the stress fields or modifying the assumptions of classical elasticity. Here, several avenues are explored:

1. Smoothing Geometric Discontinuities: Simple adjustments, such as rounding sharp corners or crack tips, can reduce stress singularities by distributing the applied stresses more evenly. However, these changes often fail to produce physically relevant stress fields, particularly when the radii are extremely small. While stresses become finite, their magnitudes can still be unrealistically high and unrepresentative of the true behavior of the material.

2. Relaxing Assumptions in Classical Elasticity: The linear theory of elasticity makes several simplifying assumptions that contribute to the emergence of stress singularities:

   - Elastic Limits: The assumption that stresses remain within the elastic range disregards plastic deformation, which can reduce stress peaks. However, plasticity does not completely resolve the singularities, especially at the onset of loading where the elastic regime dominates.
   - Small Displacement Gradients: Allowing for large strains or large displacement gradients can modify the stress fields and mitigate singularities. For instance, large strain theories improve the physical representation but may still leave some singular behavior unresolved.
   - Load Application to Undeformed Structures: Incremental load applications that account for structural deformations, as proposed in Griffith's model for cracks [23], can weaken singularities. Nevertheless, even these advanced treatments often result in reduced but persistent singularities.

3. Improving Boundary Conditions: Traditional boundary conditions, such as stress-free or clamped constraints, are often simplifications that lead to singular behavior. Replacing those classical boundary conditions with cohesive or adhesive stress boundary conditions, e.g., cohesive laws applied to the sharp edges of cracks, or enforcing inequality constraints on the boundaries that transform singular stresses into finite and physically interpretable values, the singularities can be eliminated or significantly reduced.

   - Cohesive Stress Models:

     A more sophisticated approach is to incorporate cohesive stress models, which introduce intermolecular forces at regions of high stress. These models, such as Barenblatt's cohesive zone model [24], replace the idealized stress-free crack surfaces with stress-separation laws that negate singularities near the crack tip. While effective, cohesive stress models rely heavily on assumptions about the stress distribution and require careful calibration to the specific material and loading conditions.
   - Enforcing Inequality Constraints:

     Inequality constraints ensure that material boundaries adhere to realistic physical behaviors, such as preventing interpenetration, overlapping

or excessive deformation. This approach replaces overly simplified or unrealistic boundary conditions with constraints that reflect true material interactions, leading to stress fields that are finite and physically meaningful. These constraints are particularly effective in eliminating singularities that arise from sharp geometries, contact problems, or inappropriate modeling assumptions. This method is widely used in finite element analysis (FEA) to address stress singularities in structural modeling and contact mechanics. It helps simulate realistic interactions in situations such as crack propagation, adhesive bonding, or the contact between rigid and elastic bodies that consequently, enhances the accuracy and physical relevance of stress predictions, enabling engineers to design safer, more reliable structures and materials by mitigating localized stress concentrations.

Despite these strategies, not all configurations lend themselves to complete singularity removal. Continued research into combining advanced material modelling, numerical techniques, and boundary condition refinements is essential.

1.3.2 Interpretation of singular stresses

When stress singularities cannot be entirely eliminated, they must be carefully analyzed and interpreted to extract valuable engineering insights. Understanding these singularities enables engineers to assess critical stress concentrations and develop strategies for mitigating potential failures in structural systems.

The study of singular stresses often combines analytical and numerical methods to achieve a comprehensive understanding. Analytical techniques, such as asymptotic analysis [25], are employed to describe the localized behavior of stress fields in the vicinity of singularities. These methods provide exact solutions in simplified models and are particularly useful for theoretical investigations. On the other hand, numerical tools, such as finite element analysis (FEA), enable engineers to model complex geometries and simulate the interaction of singular stresses within larger structures. By integrating these approaches, researchers can accurately capture both local and global stress responses, enhancing the reliability of engineering predictions.

Furthermore, while singular stresses are mathematically infinite and cannot exist in real materials, their implications are profound. The presence of singularities highlights zones of intense stress concentration, which are often the precursors to material failure. Understanding these regions allows engineers to take preventive measures, such as reinforcing high-stress areas, altering designs to reduce stress intensification, or selecting materials that can withstand elevated stress conditions. Moreover, singularities often influence the choice of manufacturing techniques, as certain processes can exacerbate stress concentrations.

Here, there is a critical link between theoretical models and experimental data that are the coefficients associated with singular stress fields. Coefficients such as T-stress, Energy Release Rate, and Intensity Factors play significant roles depending on the problem's context. Each coefficient provides unique insights into singular stress fields, their effects, and their implications for engineering design and failure prediction.

Stress Intensity Factors (SIFs) are the most widely recognized coefficients that encapsulate the intensity of singular stresses and provide engineers with actionable insights for design and analysis. Incorporating singularity coefficients into engineering calculations facilitates more precise estimations of stress thresholds, fatigue limits, and safety margins. This approach ensures that theoretical predictions align closely with real-world material behavior, leading to more robust and efficient structural designs.

1.3.2.1 Stress Intensity Factors (SIFs)

Stress intensity factors (SIFs) serve as fundamental parameters for quantifying the severity and characteristics of stress singularities, particularly at critical points such as crack tips or sharp corners. Fracture mechanics is amongst those engineering areas use SIFs to characterise the stress singularity at critical points. Stress singularities play a pivotal role in characterizing the behavior of materials under stress and form the foundation of linear elastic fracture mechanics (LEFM) particularly, in understanding crack propagation and predicting failure. These singularities are represented mathematically by (1.1), where r is the distance from the singularity and α is the singularity exponent. The most common singularity in fracture mechanics is the inverse square root singularity ($\alpha = 0.5$) for linear elastic materials, as seen in Mode I (opening), Mode II (sliding), and Mode III (tearing) crack loading scenarios.

By determining SIFs, engineers can evaluate whether a structure will remain intact under given loads or if it is at risk of crack propagation and catastrophic failure. From this point of view, SIFs are instrumental in assessing the safety and durability of materials, especially in high-stress environments. They also inform the design of joints, interfaces, and other structural elements where discontinuities are inevitable.

As the conclusion to this part, it is worth noting that the dual approaches of removing and interpreting stress singularities are complementary. While efforts to eliminate singularities focus on improving physical modelling and boundary conditions, interpretation techniques rely on extracting meaningful information from singular fields. Together, these methods provide engineers with robust tools to ensure structural reliability and optimize designs in the presence of complex stress configurations.

1.4 Current research focus and objectives

This study primarily investigates two cases of stress singularity. Notably, no effort was made to eliminate the singularities in either case. Instead, a paradigm shift was adopted by reframing the problems and redefining the sources of singularity. In this context, the focus is directed toward interpreting the stress singularities to derive results that are more physically meaningful and practically applicable.

1.4.1 First problem: an elastic wedge under a concentrated moment at its vertex

The first case revisits the classical problem of an elastic wedge subjected to a concentrated couple at its tip, initially introduced and solved by Carothers [26]. This solution, which exhibits a quadratic singularity in the stress field, encounters a spurious behavior at the critical angle $\alpha = 0.715\pi$, where the stress becomes unbounded within the wedge. This issue, commonly known as the "wedge paradox," highlights an inconsistency in the classical approach.

From a mathematical perspective, the paradoxical nature of Carothers' solution poses a fascinating challenge, encouraging the investigation of various alternative approaches. In linear elasticity, the characteristics of the stress field at the wedge tip are heavily influenced by the singularity's order, which, in turn, depends on the geometry and boundary conditions.

In practical terms, a wedge subjected to a concentrated couple at its tip serves as a fundamental case study for numerous engineering applications. This configuration acts as a mathematical model applicable to various scenarios, including cracks, anti-cracks, notches, bi-material interfaces, and reentrant corners. In these cases, failure is often linked to the coefficient of the singular term in the stress field. Consequently, understanding and interpreting stress singularities is critical not only for theoretical advancements but also for practical engineering applications.

To address the inconsistency of the classical theories in approaching the wedge paradox, the study introduces a new representation for the stress field in the wedge, capturing other states characterized by a quadratic singularity. This approach begins with an auxiliary problem where the wedge is conceptually divided into three wedges subjected to tip couples, determined through compatibility conditions for stress and displacement along their shared boundaries. Additionally, an alternative formulation based on the concept of strain nuclei indicates that, at the critical angle, the applied forces correspond to dipoles with no moment at the tip. The findings suggest that Carothers' original solution cannot represent all stress states associated with a quadratic singularity at the vertex. The proposed representation resolves the paradox naturally, offering a more comprehensive understanding of the stress behavior.

1.4.2 Second problem: an elastic disk under sectorial uniform temperature rise

The second analysis examines a linear elastic infinite disk, where a sector with an arbitrary opening angle 2β experiences a uniform temperature increase ΔT relative to the rest of the disk.

The problem is inspired by practical applications, particularly in architectural glazing, where one of the most common causes of glass failure is thermal stress resulting from uneven temperature distribution. The temperature field can be estimated using heat conduction equations if environmental parameters such as external and internal temperatures, solar radiation, material properties, and pane inclination are known [27].

A critical challenge arises when shading elements like sunshades, building parts, fins, or frames create cooler areas on the glass surface adjacent to warmer regions.

Numerical simulations [28, 29], indicate that while temperatures within both the shaded and sunlit zones are relatively uniform, a steep gradient forms at the narrow interface between them. Simplified engineering approaches, such as those outlined in the French NF DTU 39 P3 standard [30], are often used to estimate these temperature distributions. These methods assume uniform temperatures in both regions and disregard the narrow strip with the gradient, a simplification supported by detailed thermal investigations [28, 29]. Consequently, the glass surface can be treated as segmented into distinct areas with uniform but different temperatures for design purposes.

Thermal stress issues also occur in other contexts where thermal strain is neither spatially nor temporally smooth. Such cases include thermal shocks, localized heat sources, or materials with varying thermal properties. Additionally, stress concentrations can arise in uniform elastic materials with geometries such as cracks, sharp corners, inclusions, or notches. When subjected to temperature changes, these geometries behave similarly, producing stress concentrations due to non-uniform temperature distributions [31].

To derive the solution, the disk is conceptually divided along the boundary of the heated sector, allowing it to expand freely. Subsequently, the two parts are reassembled, and the thermal mismatch is resolved by introducing distributed arrays of glide dislocations along the interface.

The resulting approximate solutions reveal a logarithmic singularity in the stress field at the tip of the sector. However, except for the specific case of $2\beta = \pi$, the stress becomes unbounded as the dislocation arrays extend indefinitely. This outcome is consistent with dimensional analysis, which predicts unbounded stress due to the absence of an intrinsic length scale in the infinite disk. Conversely, for a finite disk, the radius R serves as an additional length parameter, expanding the range of possible solutions but complicating the analytical approach.

To bridge the gap, the study proposes relating the infinite disk solution to a finite dislocation array length determined by R. This approach demonstrates strong agreement with numerical results obtained using ABAQUS simulations. Such methods are particularly relevant for engineering applications where infinite-body assumptions, though analytically convenient, might yield unrealistic results.

The remainder of this dissertation is structured as follows:

Chapter 2 covers fundamental concepts related to stress singularities, along with a review of relevant literature.

Chapter 3 introduces two specific cases of singular stresses: an elastic wedge subjected to a tip couple and a circular plate subjected to sectorial thermal loading.

Chapter 4 focuses on the dimensional analysis of the cases presented in previous chapter.

Chapter 5 presents mathematical modeling, offers alternative solutions to the existing classical approaches, and discusses the pathological behavior of the wedge under a vertex-applied moment.

Chapter 6 provides an alternative mathematical model for a 2D elastic disk, specifically analyzing an arbitrary sector under uniform temperature rise. It also includes an analytical solution of the proposed model and a comparison between analytical results and finite element outcomes.

Chapter 2

Overview

In the realm of linearized equilibrium theory of elasticity, singular problems can be systematically categorized based on the principal sources of the singularities observed in the elastostatic field. These singularities, which represent localized regions of intense stress or displacement gradients, arise under distinct conditions, each reflecting unique physical phenomena. The primary categories of such problems are as follows [3]:

I. Load-induced singularities: These occur due to the application of concentrated forces or discontinuous load distributions. Examples [9, 11, 26, 32–36] include point loads or abrupt changes in surface tractions, where the stress field becomes unbounded near the point of application. Such singularities are particularly significant in the study of Green's functions and provide insight into the fundamental mechanics of deformable bodies under extreme localized forces.

II. Shape-induced singularities: These emerge from the geometry of the body, specifically at locations where sharp notches, corners, or cracks exist [20, 37–48]. The inherent sharpness or abruptness of such features intensifies stress concentrations, making them critical in the analysis of structural components, particularly in failure prediction and material design.

III. Singularities induced by mixed boundary conditions: These arise in problems where disparate boundary constraints are applied simultaneously [20, 41–48]. A common example is observed in contact and indentation problems, where one region of a boundary may be fixed while another is subjected to loading or displacement constraints. These mixed conditions create localized stress fields that are often difficult to predict without advanced analytical or numerical techniques.

IV. Material discontinuity-induced singularities: Singularities of this type occur at interfaces between different materials, such as in bonded assemblies of distinct homogeneous elastic materials [49–53]. These are characteristic of inclusion problems, where embedded regions of differing material properties lead to abrupt changes in stress and displacement fields. Such scenarios are frequently encountered in composite materials and load-transfer problems, where understanding the stress distribution is critical for ensuring structural integrity.

V. singularities due to discontinuities in displacement field: the most important cases in this class of singularities are those involving dislocations [54–60]. A dislocation is a line defect where atoms deviate from their regular lattice positions within a crystal structure. The first mathematical framework for describing the elastic field of a singularity caused by cutting and displacing a continuous body was introduced

by Volterra in 1907 [61]. The core characteristics of dislocations significantly impact the inherent ductility or brittleness of materials. Additionally, the interaction between dislocations and other defects in the crystal lattice is a key factor in shaping the mechanical properties of metals. This principle forms the foundation of the classical strengthening mechanism, which has guided advancements in understanding and controlling dislocation behavior to improve the mechanical performance of metals [62].

Concerning the complexity of singular problems lead to challenges in mathematical approaches, the following parts are dedicated to investigation of some general mathematical aspects of either category of stress singularities.

2.1 Stress singularities due to the concentrated forces

Among the various categories of singular problems in linear theory of elasticity, those involving concentrated loads occupy a particularly significant position. This prominence stems not only from their foundational role in the development of Green's Functions but also from the conceptual challenges inherent in incorporating such loads into the mechanics of deformable continua. Unlike particle systems and rigid bodies, where the concept of a "concentrated load" is intuitive and straightforward, its application in the context of elastic continua requires careful justification and mathematical precision.

2.1.1 Kelvin's solution

A fundamental and physically sound framework for dealing with concentrated loads in linear elasticity was pioneered by Kelvin [32]. His approach provides a conceptual foundation for addressing the singularities associated with point loads applied to an elastic body occupying infinite space. Kelvin's method begins by replacing the singular problem with a regularized one, where the concentrated load is approximated by a smooth, unidirectional distributed body force that vanishes outside a sphere centered at the load application point. The solution to this regular problem is unique under the condition that displacements vanish at infinity, and it admits an explicit integral representation. By contracting the region of load application to the center of the sphere while maintaining the resultant body force as the concentrated load, Kelvin derived a solution that is both physically meaningful and mathematically rigorous. This limiting process not only defines the problem unambiguously but also yields the familiar closed-form solution. Kelvin's solution serves as the elastostatic counterpart to the singular solution of Laplace's equation represented by the Newtonian potential of a point mass. The key properties of this solution are:

1. It satisfies the governing field equations in the absence of body forces everywhere except at the load point.

2. The displacement field diminishes to zero at infinity.

3. The resultant traction force on any spherical surface centered at the load point equals the prescribed concentrated load.

4. Displacements and stresses exhibit singular behaviors of $O(r^{-1})$ and $O(r^{-2})$, respectively, as the radial distance r approaches zero, highlighting the unbounded nature of these fields at the load point.

Despite the elegance of Kelvin's solution, subsequent treatments in the literature have often opted for a direct formulation of the problem based on its core properties-excluding the detailed limit process. This simplified approach typically considers only the first three conditions but does not impose constraints on the orders of displacement or stress singularities. However, this leads to a lack of uniqueness, as additional solutions can be constructed by adding higher-order singular fields, such as those corresponding to centers of dilatation [33, 63].

Importantly, this ambiguity does not violate the classical uniqueness theorem of elasticityt, which does not explicitly address singular formulations. Kelvin's full set of conditions, including the singularity order constraints, is necessary to uniquely characterize the solution, ensuring the exclusion of such pseudo-solutions. Extending Kelvin's methodology to problems involving concentrated surface loads introduces additional complexities. Analogous limiting processes can be applied to confirm that the singularities at the point of application of concentrated surface loads mirror those in Kelvin's original problem [11]. However, implementing such a process often leads to cumbersome and less practical solutions.

A significant advancement came with the development of a uniqueness theorem [9, 64, 65], that encompasses both concentrated surface and internal loads, as well as distributed tractions and body forces. This theorem establishes that a set of conditions, analogous to those in Kelvin's formulation [32], supplemented by boundary conditions and constraints at infinity for unbounded regions, uniquely determines the solution to these singular problems. This framework provides a direct formulation, bypassing the need for explicit limiting processes. Considering the pivotal role of Kelvin's solution in the analysis of stress singularities, it is beneficial to examine key aspects of its application in addressing singular problems within the framework of linear elasticity theory, including:

1. Pseudo-Solutions;
   The practical implications of theoretical advances in study of stress singularity based on Kelvin's solution are underscored by studies such as the analysis of an elastic sphere subjected to two equal and opposite concentrated surface loads [9, 11, 66]. This problem, relevant to the stress analysis of ball bearings, demonstrates the existence of pseudo-solutions that differ from the unique physical solution by exhibiting inadmissible higher-order singularities at the load points.
   Through rigorous limit processes starting with distributed loads, the physically accurate solution was validated and found to align with experimental results, such as those from photo-elastic studies of stress distributions in symmetrical configurations [34]. These findings highlight the utility of the concentrated load idealization, despite its mathematical abstraction.

2. Reduction of Singularities;
   Direct formulations of concentrated-load problems, Kelvin's solution, also facilitate the isolation and removal of singular parts from the desired solution, reducing the problem to one governed by finite and continuous tractions. The

solution includes a singular part that arises due to the nature of the concentrated load and leads to stress fields that become infinite at the point of application, in addition to a regular part that represents the finite and continuous response of the material. Direct formulations explicitly separate these components. By superposing the fundamental solution, in a closed-form representation, with the actual boundary conditions of the problem, the singularity associated with the concentrated load can be isolated. The remaining problem then focuses on the adjustment of the boundary conditions, which involves only finite and continuous tractions. These refinements provide a more complete understanding of stress fields and enhance the applicability of theoretical models to real-world geometries [2, 4, 67, 68].

2.1.2 Wedge problem

While singularities arising from concentrated forces are well-documented, Sternberg and Koiter's analysis [69], highlights that the inclusion of concentrated moments introduces even subtler and more intricate challenges in linear elasticity. Solutions to these problems rely on the direct formulation of boundary conditions, symmetry constraints, and the requirements for stress fields at infinity. However, singularities in such cases are influenced by the wedge angle, with a critical angle marking the transition to unbounded stresses throughout the body. Beyond this critical angle, the direct formulation of the problem becomes insufficient, necessitating the reintroduction of limiting processes to achieve meaningful solutions.

These findings reveal the limitations of idealizations such as concentrated couples in specific geometric configurations [22, 26, 70, 71]. Here, it is worth noting that, what mentioned above, was the main incentive to study the classical problem of wedge paradox in the next chapters of the present work. Regarding the integrity of study of wedge problem with the general topic of the current work also prominent importance of this type of singularities in solid mechanics, following paragraphs are dedicated to a brief review of the literature, concerning the wedge problem.

The linear elasticity solutions to wedge problem, generally use two distinct methodologies:

- firstly, a truncated wedge subjected to tractions distributed along an arc of radius r_0 that are equivalent to the applied action at the tip, followed by taking the limit as $r_0 \to 0$.

- secondly, a wedge experiencing distributed tractions along its flanks that are equivalent to the applied load, with the distribution length approaching zero.

Carothers [26] employed the first method. In contrast, Sternberg and Koiter [69] exemplify the second approach by considering finite segments $0 \leq r \leq r_0$ on the lateral faces $\theta = \pm\alpha$, where a distributed normal load, antisymmetric about the wedge axis and statically equivalent to a moment M, is applied. By applying the Mellin Integral Transformation with respect to r to the governing biharmonic equation for the stress function and allowing $r \to 0$, they derived an alternative solution that exhibits a different order of singularity compared to the r^{-2}. This alternative solution remains consistent even at the critical angle.

Similarly, Bogy [72] utilized the Mellin transform to examine how the order of singularity depends on the opening angle and Lamé constants in a bimaterial

wedge subjected to surface tractions. Dundurs and Markenscoff [73] took a different perspective by analyzing a wedge loaded by a concentrated couple approaching the vertex from within. Neuber [74] offered a more physical resolution to the paradox by proposing the onset of plasticity. He suggested that once the material yields, the shear stress plateaus, allowing the concentrated couple to be replaced by a distributed constant tangential stress acting around a small circular cavity centered at the wedge's vertex. This approach enables the construction of a general solution that avoids the unrealistic behavior at the critical angle, converging to the solution by Sternberg and Koiter [69] when certain terms become negligible. Following a similar methodology, Villaggio [75], by applying actions within cavities of various shapes, demonstrated through multiple examples that the paradox is not limited to wedges but also occurs in unbounded regions that resemble a rectilinear wedge at infinity, while differing near the vertex where the concentrated couple is applied.

Other techniques build upon the foundational work of Williams [14], who, through separation of variables in the Airy stress function, derived eigenfunctions for singular stress states that could be superimposed to formulate solutions for elastic wedges with free edges. Dempsey [76] identified the limitations of the stress function forms proposed by Williams [14], extending the results to wedges with surfaces under uniform pressure and determining stress states for all possible opening angles α, including the critical angle α^*. Leguillon [77] presented a solution that achieved the necessary equivalence with the tip couple at the critical angle. However, this solution was flawed as it resulted in an infinite moment resultant on arcs of arbitrary lengths at infinity, only converging to a finite limit when considering the entire wedge angle. Notably, Leguillon observed that eigenfunctions featuring a stress singularity of order r^{-2} had to be excluded because they produced a tip couple with zero moment at the critical angle.

From a purely mathematical standpoint, the paradoxical behavior observed in Carothers' solution presents an intriguing problem, prompting the exploration of a wide range of alternative methods. Solutions in linear elasticity are significantly influenced by the order of the singularity of the stress field at the wedge tip, depending on the geometry and boundary conditions. Here, the Mellin transform proves to be a valuable tool for the asymptotic analysis of the stress state [69, 78–81]. Another prevalent approach in studying singularity problems involves the use of asymptotic series [82, 83]. Gregory [84], utilizing a biharmonic Green's function for an infinite strip domain and subsequently generalizing the results to a wedge problem, reproduced the eigenfunctions identified by Williams [14]. Additionally, Green and Zerna [85] employed conformal transformations in the complex plane to map the wedge to an infinite strip region and addressed the problem through Fourier transformation.

2.1.3 Discontinuous loadings

Regarding the general class of singularities due to concentrated loads, a possible scenario could be any discontinuity in loading. The discussion about this class of loadings, exemplified by half-plane problems where normal or tangential tractions exhibit finite jump discontinuities. In these cases, the displacement field remains continuous, but stress components may display logarithmic singularities depending on the nature of the loading discontinuity. Direct formulations, accompanied by conditions ensuring bounded displacements at discontinuity points, firstly introduced

by Knowles and Pucik [39]. They provided a complete framework for analyzing such problems without requiring explicit limit processes throughout generalization of the classical uniqueness theorem in two-dimension elasticity. This extended theorem ensures that the boundedness of displacements alone, is sufficient to guarantee uniqueness in these formulations, offering a robust and economical approach to singular problems in planar elasticity. While analogous results are anticipated for three-dimensional problems, the existing proofs lack the flexibility to encompass line-singularities, highlighting an area for further theoretical development.

2.2 Shape-induced singularities

In this category of singularities, crack problems with a significant role in solid mechanics in general and fracture mechanics in particular, represent crucial examples of singular stresses. To illustrate, consider a traction-free, plane crack of constant width extending infinitely in an infinite elastic medium, subjected to various homogeneous loadings at infinity. Three modes of near-tip-deformation demonstrated in Figure 2.1.

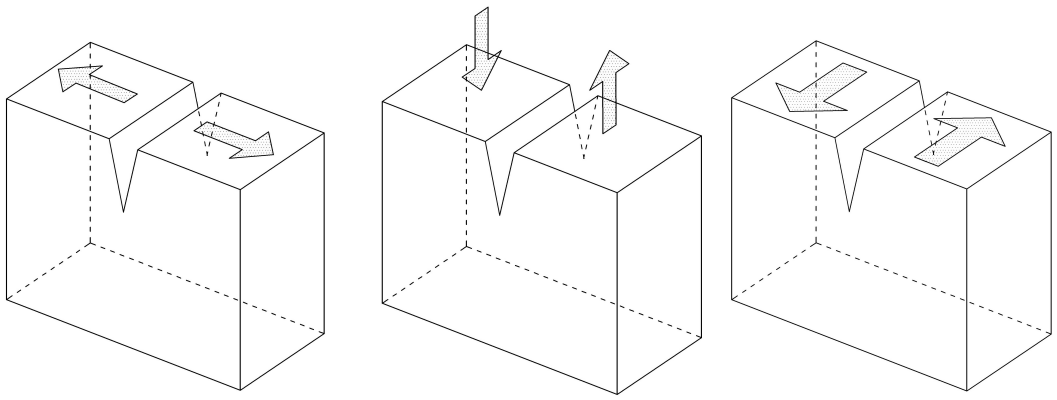

(a) (b) (c)

Figure 2.1: (a) Mode I: Opening Mode (b) Mode II: Sliding/Shearing Mode (c) Mode III: Tearing Mode

Three fundamental two-dimensional solutions for the singular stress states due to the above-mentioned deformation fields are presented according to Equation (2.1) [40, 43, 86, 87].

$$\sigma_{ij}^{m} = \frac{K_m}{\sqrt{2\pi r}} f_{ij}^{m}(\theta), \quad i,j = r,\theta, \quad \text{and} \quad m = \mathrm{I}, \mathrm{II}, \mathrm{III}. \tag{2.1}$$

where K_m is the Mode m^{th} stress intensity factor, and $f_{ij}(\theta)$ are angular functions of each mode dependent on the crack-tip geometry and loading.

The first two solutions deal with plane deformations orthogonal to the crack edges. These correspond to in-plane loading scenarios: one involving tension perpendicular to the crack faces, Mode I or Opening Mode, and the other involving pure shear on planes parallel and perpendicular to the crack faces, Mode II or Sliding/Shearing Mode. Since the scenario of uniaxial tension parallel to the crack faces is straightforward, these two modes suffice to address any uniform in-plane loading

at infinity compatible with a traction-free crack under the framework of linearized plane strain or generalized plane stress theories. The third fundamental solution pertains to anti-plane shear deformations caused by longitudinal shearing traction at infinity, acting along planes parallel to the crack faces, Mode III or Tearing Mode and in directions parallel to the crack edges. For all three modes, the displacement field remains finite and continuous at the crack tips, whereas the stress field diverges with an order of $\mathrm{O}\left(r^{-1/2}\right)$, where r represents the distance from the crack tip.

In Mode I, the resulting stress state is symmetric about the crack plane, while it is antisymmetric in Modes II and III. Furthermore, the latter two cases are termed "gliding modes," where the crack faces slide against one another without opening, as predicted by linear theory. These solutions align with the limiting forms of corresponding regular two-dimensional solutions for an infinite elastic body containing an elliptic cylindrical hole, which degenerates into a plane crack. This correspondence is frequently cited to validate the physical significance of such singular solutions. However, based on the generalized uniqueness theorem, the reliance on such a limiting process is unnecessary for formulating a coherent and physically consistent direct approach to plane crack problems in linear theory of elasticity.

- Barrenblatt's approach to negate crack-tip singularities

In crack-related scenarios, singularities arising from distant loading can be neutralized by compensating with the effects of forces acting on the crack's flanks. Barenblatt [88] acknowledges Khristianovitch as the first to recognize this phenomenon in his collaborative 1955 study with Zheltov [89]. Their research focused on analyzing a substantial rock layer, largely composed of oil-rich shale, to determine the conditions under which a pressurized imperfection within the layer would initiate fracturing. The rock layer is subjected to a uniform pressure, p_o, while the areas near the flaw tips are exposed to a higher internal pressure, p_i, as illustrated in 2.2 The problem is considered in two dimensions and assumes elastic behavior.

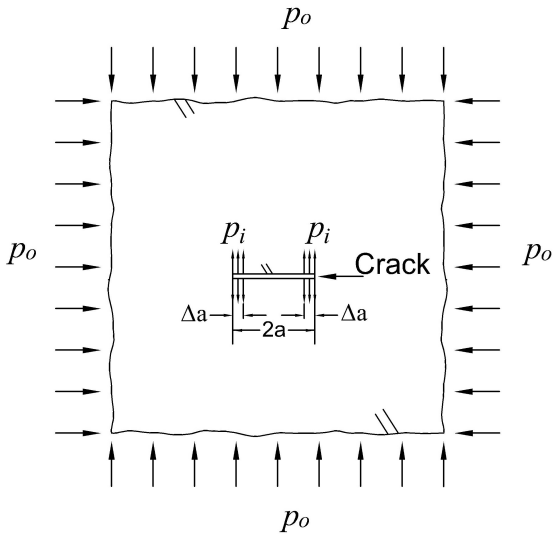

Figure 2.2: pressurized crack

When the portion of the flaw affected by p_i, represented by Δa, is an appropriate fraction of the total flaw width $2a$, the tensile stress singularity caused by p_i, can counteract the compressive stress singularity generated by p_o. Specifically, no

singularity occurs in the system shown in 2.2, if the condition defined by Equation (2.2) is satisfied.

$$\frac{\Delta a}{2a} = \sin^2\left(\frac{\pi p_0}{4p_i}\right), \quad (p_i > p_0)\,. \tag{2.2}$$

Barenblatt [88], introduced cohesive normal stresses as a replacement for the applied internal pressure p_i. His explanation includes the following points:

1. Cracks are generally much longer in relation to their height, allowing them to be represented as mathematically sharp slits.

2. Near the tip of the crack, the flanks are close enough for intermolecular cohesive stresses to develop between them.

3. These cohesive stresses can be distributed in a way that cancels out the tensile stress singularities caused by remote loading.

It is also assumed that the zone near the crack tip where cohesive stresses act is relatively small compared to the overall length of the crack.

2.3 Singularities due to mixed boundary conditions

This discussion delves into singular problems of 3rd class, using the mixed plane problem of a half-plane indented by a rigid, flat-ended punch as an example. The boundary conditions at the edge of the half-plane differ depending on whether the punch is "smooth" or "rough." For both cases, the normal displacement along the contact segment is constant, and the traction vector is zero elsewhere. However, a smooth punch eliminates shear tractions, while a rough punch prevents tangential contact displacement.

To maintain solution validity (uniqueness), the conventional formulation requires bounded displacements at the punch corners. This approach does not necessarily rely on physical justification through a regularization process, as mixed singular problems like this often defy straightforward regularization. Classical solutions to these punch problems predict unbounded stresses near the punch corners, with stresses behaving as $r^{-1/2}$, where r is the distance from the corner. Incompressible materials provide an exception where both smooth and rough punch solutions converge. However, in the rough punch case, oscillatory behavior emerges near the punch corners, with normal tractions alternating between compression and tension infinitely often. These oscillations, though confined to narrow regions, are incompatible with physical constraints and unilateral contact conditions.

A related issue arises in the plane problem involving two bonded semi-infinite elastic bodies separated by a finite-width crack under Mode I loading. The theoretical solution exhibits oscillatory displacements near the crack edges, leading to unphysical overlap of the crack faces.

For singularities of types (*iii*) in plane problems, Knein [20] and Williams [14], introduced an asymptotic approach that examines local singularities in two-dimensional elastostatic fields. This method uses a biharmonic stress function χ along with a harmonic displacement function ψ_1, as Equation (2.3), to construct global solutions for

generalized plane stress in wedge-shaped domains, accounting for various boundary conditions and body force-free regions.

$$\begin{aligned}\chi &= r^{(\lambda+1)}\left[b_1\sin(\lambda+1)\theta + b_2\cos(\lambda+1)\theta + b_3\sin(\lambda-1)\theta + b_4\cos(\lambda-1)\theta\right] \\ &\equiv r^{(\lambda+1)}\mathrm{F}(\theta;\lambda), \\ \psi_1 &= r^m\left(a_1\cos m\theta + a_2\sin m\theta\right) \equiv r^m G(\theta;m),\end{aligned} \tag{2.3}$$

where, χ is related to ψ_1 by

$$\nabla^2\chi = \frac{\partial}{\partial r}\left(r\frac{\partial\psi_1}{\partial\theta}\right), \tag{2.4}$$

According to Equation (2.3), compatibility of the powers of r requires $\lambda = \mathrm{m}+1$. Additionally, the coefficients are given as

$$a_1 = -\frac{4}{\lambda-1}b_3, \quad \text{and} \quad a_2 = \frac{4}{\lambda-1}b_4, \tag{2.5}$$

The solutions involve eigenvalue problems, with the eigenvalue λ, determining the singularity strength. Here, the Airy stress function $\chi(r,\theta)$, satisfies a fourth-order differential equation. These solutions form an infinite sequence of fields, each characterized by an eigenvalue and an undetermined amplitude parameter. Displacements remain bounded if the real part of λ, (β), satisfies $0 < \beta < 1$, but stresses are unbounded when $r \to 0$. Regarding the boundary conditions, three cases are considered for the wedge boundaries

1. Both boundaries are traction-free.
2. Both boundaries are fixed.
3. One boundary is traction-free while the other is fixed.

In all cases, there is at least one eigenvalue λ, with $0 < \beta < 1$, for wedge angles between π and 2π. In Cases 1 and 2, λ is real, while in Case 3 , it becomes complex, resulting in oscillatory stress fields with terms like $r^{\beta-1}[\cos(\kappa\log r)$ or $\sin(\kappa\log r)])$ where κ depends on Poisson's ratio ν.

The elastostatic fields associated with the smallest eigenvalue λ provide dominant asymptotic behavior near singular points in boundary-value problems. This aligns with global solutions to problems like the rough punch and plane crack scenarios. However, determining the amplitude parameter, which depends on global geometry, boundary conditions, and conditions at infinity, is crucial for solving such problems efficiently.

For crack problems, this parameter often represents the essential information about crack-tip singularities, potentially bypassing the need for global analysis. Rice [42] demonstrated an example where the amplitude parameter could be determined using a conservation law introduced by Eshelby [43], which applies to finite equilibrium theory. Freund [44] later expanded this concept by applying additional conservation laws to determine stress-intensity factors for specific crack and loading configurations. However, no universal framework exists for deriving the amplitude parameter, and existing conservation laws remain inadequate for general Mode I and Mode II crack problems.

2.4 Singularities due to material discontinuity

At the interface between an elastic material and a bonded inclusion with different elastic properties, singularities involve only finite discontinuities in stress and displacement gradients. However, displacements themselves remain smooth across the interface due to the bonding, and traction continuity is required to maintain equilibrium. A significant subset of class (iv) problems, known as "load-transfer problems," explores the mechanical interaction between two materials with differing elastic behaviors bonded along part of their boundary.

These scenarios often involve one material behaving as a quasi-one-dimensional elastic structure. For instance, plane load-transfer problems, such as those related to plate-stringer systems, are fundamental in the design of aircraft components. Similarly, problems involving load diffusion from or absorption by an elastic rod connected to a three-dimensional structure are crucial in civil engineering and key to understanding the mechanics of fiber-reinforced composites. For an overview of analytical studies on plane and spatial load-transfer problems up to 1970, see [90].

2.5 Singularities due to discontinuities in displacement fields

This section aims to highlight some important concepts and definitions related to dislocations. Considering that this concept has been adopted in the study at hand, (problem of an elastic disk subjected to sectorial thermal loading) a concise review of this topic would offer a clearer understanding of the subsequent problem. The following part, has been borrowed from the introductive and quite empirical work of Hull and Bacon [91] about "Dislocations". Dislocations are typically classified into two primary types:

Edge Dislocations: These occur when an extra half-plane of atoms is inserted into the crystal, causing a discontinuity in the lattice. The "edge" of this plane is the core of the dislocation.

Screw Dislocations: These arise when the lattice experiences a helical twist due to shear deformation, creating a displacement discontinuity parallel to the dislocation line.

Some dislocations exhibit mixed characteristics, combining elements of both edge and screw dislocations.

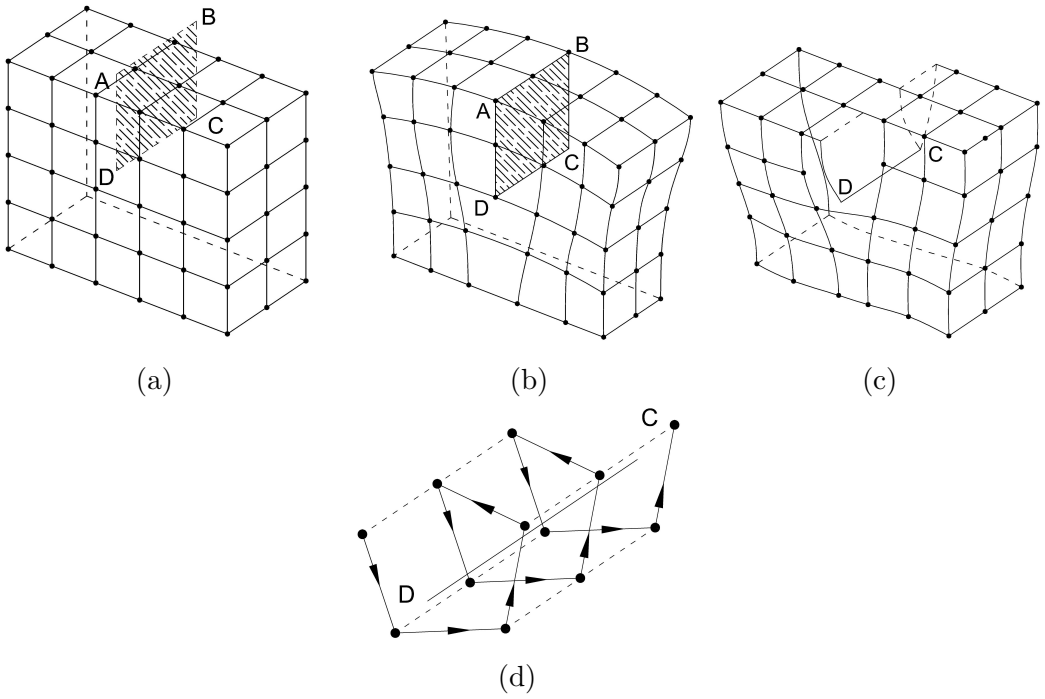

Figure 2.3: (a) Model of a simple cubic lattice; the atoms are represented by filled circles, and the bonds between atoms by springs, only a few of which are shown; (b) positive edge dislocation DC formed by inserting an extra half-plane of atoms in ABCD; (c) left-handed screw dislocation DC formed by displacing the faces ABCD relative to each other in direction AB ; (d) spiral of atoms adjacent to the line DC in (c) (see reference [91]).

The structure of atoms surrounding an edge dislocation can be represented by a sequence of actions. First, suppose that all bonds along the surface $ABCD$ are broken, and the crystal faces are moved apart to insert an additional half-plane of atoms into the resulting gap, as illustrated in 2.3b. This process displaces the faces of the gap by one atomic spacing, creating the greatest disruption near the line DC. Farther away from DC, the distortion of atomic bonds progressively decreases. The line DC, referred to as a positive edge dislocation, is symbolized by $\perp$. If the extra plane of atoms were instead introduced below the $ABCD$ plane, a negative edge dislocation would form, denoted by T.

For a screw dislocation, the atomic arrangement is modeled by shifting one side of the crystal along AB relative to the other, as depicted in 2.3c. This transformation produces a helicoidal shape, similar to a spiral staircase. Initially parallel planes perpendicular to DC are converted into a continuous surface, with the spiral pattern evident in the atom positions shown in 2.3d. The dislocation along DC is identified as a screw dislocation. If the spiral advances by one plane during a clockwise circuit around the dislocation line, it is classified as a right-handed screw dislocation; if the progression is reversed, it is left-handed. It is important to note that, in both edge and screw dislocations, the atomic arrangement across the interface $ABCD$ remains unchanged from its original configuration before the bonds were broken.

2.5.1 Burgers vector and circuit of a dislocation

The most practical way to define a dislocation is through the concept of the Burgers circuit. A Burgers circuit is a closed loop formed by tracing a path from atom to atom within a crystal containing dislocations.

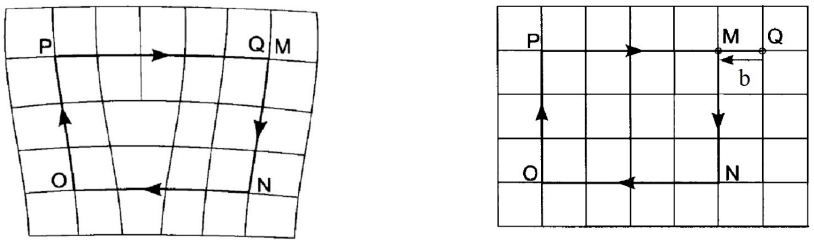

(a) Placeholder caption (b) Placeholder caption

Figure 2.4: (a) Burgers circuit round an edge dislocation with a positive line sense into the paper, (b) the same circuit in a perfect crystal. The closure failure is the Bergers vector **b** (see [91]).

This is illustrated in 2.4a with the path $MNOPQ$. If the same atom-to-atom path is traced in a perfect crystal without dislocations, as shown in 2.3b, and the circuit fails to close, it implies that the first circuit in 2.4a encircles one or more dislocations. The vector required to close the loop is known as the Burgers vector. For accuracy, the circuit in the actual crystal must pass only through undisturbed regions of the lattice.

To simplify, consider a Burgers circuit enclosing a single dislocation, as shown in 2.4a. The sequence of movements in the perfect crystal mirrors the circuit $MNOPQ$ in the dislocated crystal. The vector **b**, from point Q to M , which completes the loop, represents the Burgers vector and is perpendicular to the dislocation line (see 2.3b). For a screw dislocation, depicted in 2.5, the Burgers vector **b**, is instead aligned parallel to the dislocation line. This leads to two critical rules:

1. For an edge dislocation, the Burgers vector is perpendicular to the dislocation line.

2. For a screw dislocation, the Burgers vector is parallel to the dislocation line.

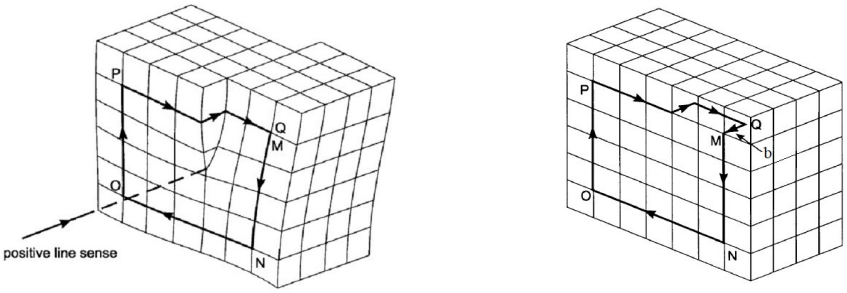

(a) Placeholder caption (b) Placeholder caption

Figure 2.5: (a) Burgers circuits around a screw dislocation with positive line sense in the direction shown. (b) the same circuite in a perfect crystal, the closure failure is the Bergers vector (see[91]).

In general, the dislocation line may lie at an arbitrary angle to the Burgers vector, combining edge and screw characteristics. Nonetheless, the Burgers vector of a single dislocation remains constant in magnitude and direction, regardless of the dislocation line's position or orientation.

For other defects, such as vacancies or interstitials, Burgers circuits do not result in closure failure. Two conventions arise from the Burgers circuit approach:

1. When viewed along the dislocation line, which defines its positive direction, the circuit is traced clockwise (as in 2.4a and 2.5a).

2. The Burgers vector is defined from the end to the start of the reference circuit in the perfect crystal, referred to as the right-hand/finish-start (RH/FS) convention.

Reversing the dislocation line's direction reverses the Burgers vector for that dislocation. Furthermore, dislocations with identical line senses but opposite Burgers vectors (or vice versa) are complementary. For example, a positive edge dislocation is the counterpart to a negative edge dislocation, and a right-handed screw dislocation is the opposite of a left-handed one. When such opposite dislocations meet, they cancel each other out, restoring the crystal to its perfect state. In simple cubic crystals, as shown in Figures 2.4 and 2.5, the Burgers vector corresponds to the shortest lattice translation vector connecting two lattice points. A dislocation whose Burgers vector is a lattice translation vector is classified as a perfect or unit dislocation [91].

2.5.2 Movement of dislocations

Dislocations in crystalline solids exhibit two primary modes of movement: glide or conservative motion and climb or non-conservative motion.

1. **Glide Motion**: This occurs when a dislocation moves within the plane that contains both its dislocation line and the Burgers vector. Dislocations capable of this movement are referred to as "Glissile", while those unable to glide are termed Sessile. Glide motion plays a pivotal role in the plastic deformation of crystalline materials, as the collective glide of multiple dislocations manifests as slip. Slip involves the sequential displacement of atomic planes over one another, occurring along specific crystallographic planes known as slip planes. This mechanism forms the foundation of how materials accommodate deformation under applied stress.

2. **Climb Motion**: Unlike glide, climb involves the movement of dislocations out of their glide plane, perpendicular to the Burgers vector. This non-conservative process requires the addition or removal of atoms at the dislocation core, facilitated by atomic diffusion. As a result, climb is particularly significant at elevated temperatures, where diffusion processes are more active.

The interaction between glide and climb dislocations determines the overall mechanical response of materials. While glide dominates at lower temperatures, enabling materials to deform plastically, climb contributes to phenomena such as creep and stress relaxation at higher temperatures, where diffusion-driven mechanisms become prominent.

In conclusion to this section, it is worth noting that dislocations serve as fundamental examples of singularities in elastic fields. They introduce abrupt displacement discontinuities while preserving the equilibrium of stress and strain. A thorough understanding of these singularities is crucial for accurately predicting and optimizing material performance in various engineering applications. Dislocations are particularly significant in the study of plastic deformation, where they facilitate the movement of material layers and enable plastic flow under applied stress. Their role is equally critical in material strength assessments, as the density and mobility of dislocations directly influence properties such as yield strength, hardness, and ductility.

Additionally, in the context of fracture mechanics, the interactions between dislocations and cracks play a pivotal role in determining material toughness and resistance to failure. These insights underscore the importance of dislocations in the broader study of mechanical behavior, offering essential tools for the design and analysis of advanced materials.

2.6 Numerical analysis of stress singularities

Previously in the present chapter, stress singularities arising from different sources introduced. It is worth nothing that, accurately modeling these singularities and solving the associated equations presents significant challenges in structural analysis. The primary difficulty lies in the localized and theoretically infinite nature of stress concentrations, which traditional analytical approaches fail to capture effectively. As highlighted briefly in Section 1.3.2 of Chapter 1, these challenges have led researchers to study singularities more deeply due to their critical role in structural integrity and predicting failure mechanisms.

In this context, numerical methods play an essential role. Advanced approaches such as the Boundary Finite Element Method (BFEM), the Extended Finite Element Method (XFEM), and other adaptive techniques offer precise solutions for analyzing stress singularities. By employing these advanced numerical techniques, engineers can improve the accuracy of failure predictions, optimize designs to reduce singular effects, and create more resilient structures and materials. These methods enhance simulation accuracy and drive progress in fields like fracture mechanics, fatigue analysis, and the design of composite and layered structures.

Several widely used computational methods are available for solving boundary value problems in science and engineering. Among those, the Finite Difference Method (FDM), the Finite Volume Method (FVM), the Finite Element Method (FEM) [92], and the Boundary Element Method (BEM) [93–97], are the most prominent. These techniques can be classified by their discretization approach.

The FDM, FVM, and FEM rely on domain-discretization, where the entire computational region is subdivided into smaller elements or volumes. In contrast, the BEM uses a boundarydiscretization approach, requiring discretization only along the boundary or surface, which significantly reduces meshing time and computational load, especially for problems confined to boundary regions.

To maintain the boundary-only discretization feature of the BEM [98–100], fundamental solutions or **Green's functions** that satisfy the governing differential equations must be known in advance. This makes the BEM particularly well-suited

for problems involving unbounded domains or thin structures, where meshing the entire domain would be computationally prohibitive.

Moreover, the BEM can integrate seamlessly with Computer-Aided Design (CAD) tools via Isogeometric Analysis (IGA) [101, 102]. This integration benefits from the BEM's reliance on boundary representations, allowing for efficient compatibility with CAD geometries. This approach has been applied successfully to various elliptic problems, such as the Laplace equation [103–105], the Helmholtz equation [106–109], and in fields like electromagnetics [110], elastodynamics [111], and fracture mechanics [112, 113].

Despite its advantages, the BEM faces challenges related to the computation of **singular integrals** inherent in the use of fundamental solutions. These integrals are often complex and time-consuming, making efficient numerical techniques for handling them essential. Research continues to develop better methods to address these computational difficulties.

To overcome the limitations of singular integrals in conventional BEM [114–119], one approach involves introducing a fictitious boundary that does not overlap with the actual physical boundary. This category includes methods such as the Method of Fundamental Solutions (MFS) [120–123], the Virtual BEM [124], and the Distributed Source Boundary Point Method [125]. These techniques shift the complexity away from the physical boundary, simplifying the handling of singularities. However, the accuracy and stability of these methods are highly sensitive to the placement of the fictitious boundary. Determining the optimal location remains a challenge, particularly for geometrically complex or multiply connected domains.

Another strategy to avoid singular integrals is to use nonsingular semi-analytical basis functions instead of fundamental solutions. Techniques in this category include the Trefftz Method [126, 127], the Boundary Knot Method (BKM) [128], the Boundary Collocation Method (BCM) [129], and the Plane Wave Expansion (PWE) Method [130]. These methods avoid singularities by employing basis functions that do not exhibit singular behavior. However, deriving these nonsingular basis functions is challenging, especially for high-dimensional partial differential equations (PDEs). The difficulty increases with the complexity and dimensionality of the problem, making generalization difficult.

In conclusion, while both fictitious boundary approaches and nonsingular basis function methods offer promising alternatives to traditional BEM, each has unique challenges. The choice of the best method depends on factors such as domain complexity, the type of PDE, and the desired accuracy and computational efficiency. In 2009, Chen et al. [131, 132], proposed the **Source-Intensity-Based Method** (SBM) as an effective approach to address the challenges associated with the singularities of fundamental solutions in conventional Boundary Element Methods (BEM). The core innovation of the SBM lies in the introduction of Origin Intensity Factors (OIFs), also known as Source Intensity Factors in some studies. These factors serve to eliminate the singular behavior of the fundamental solutions, thereby simplifying the computational process.

The SBM achieves de-singularization by replacing the singular fundamental solutions with OIFs, which quantify the intensity of sources located near the boundary. This modification allows the method to retain the accuracy of traditional BEM while avoiding the computational difficulties of singular integrals. Consequently, the SBM is particularly well-suited for problems involving stress singularities, such as those

found at cracks, notches, and sharp corners.

One of the primary advantages of the SBM is its ability to circumvent the need for complex singular integral evaluations, which are a significant challenge in standard BEM implementations. By eliminating these singularities, the method improves both the numerical stability and the computational efficiency of the solution process. This makes the SBM an attractive option for analyzing problems in fracture mechanics, elasticity, and potential theory, where stress concentrations and discontinuities are prevalent.

However, the successful application of SBM relies on accurately determining the source intensity factors and appropriately positioning the source points. This requirement can become challenging for domains with intricate geometries or high-dimensional problems. Despite these challenges, the SBM remains a promising technique for enhancing the accuracy of boundary-based numerical methods and has seen applications beyond elasticity, including areas like heat transfer, acoustics, and electromagnetics. Research efforts continue to refine the SBM, exploring improvements in source placement algorithms and extending its compatibility with isogeometric analysis (IGA) and meshless methods. These advancements aim to broaden the applicability and efficiency of the SBM in solving complex engineering and scientific problems.

Most physical and engineering problems can be simplified to boundary value problems, whose numerical solution must satisfy the related partial differential equations (PDEs) subjected to the boundary conditions. Without loss of generality, the following elliptical PDE problems are considered

$$Ru(x) = f(x), \quad x \in \Omega, \tag{2.6a}$$

$$Bu(x) = g(x), \quad x \in \partial\Omega, \tag{2.6b}$$

where, $u(x)$ is the vector of the unknown physical quantities (such as temperature, pressure and displacements etc.) to be determined, $f(x)$ and $g(x)$ denote, respectively, the vectors of known source functions and boundary condition functions. Finally, R and B stand for the partial differential operator matrix and boundary differential operator matrix, respectively so, they will appear according to constitutive relations of the elastic problem. In case of plane stress problems in linear theory of elasticity we will have:

$$\begin{aligned} u(x) &= [u_1(x), u_2(x)]^T, \\ f(x) &= [f_1(x), f_2(x)]^T, \\ g(x) &= [g_1(x), g_2(x)]^T. \end{aligned} \tag{2.7}$$

The remainder of this chapter focuses on reviewing the two most common techniques for solving boundary value problems of (2.6).

2.6.1 Formulation of Collocation Methods

The solution to the boundary value problem described by Equations (2.6) can be approached using the Weighted Residual Method (WRM) [133]. In WRM, the

starting assumption is an approximate (trial) solution (u) for a general elliptic partial differential equation (PDE), expressed as: $u = \sum_{j=1}^{J} \alpha_j \phi_j$ or in matrix form as $\boldsymbol{u} = \boldsymbol{\Phi}\boldsymbol{\alpha}$. where, $\boldsymbol{\alpha} = \{\alpha_j\}$ represents the vector of unknown coefficients, and $\boldsymbol{\Phi} = \{\phi_j\}$ is a set of known linearly independent trial functions.

Substituting this trial solution into the boundary value problem introduces errors, since the equations are no longer satisfied exactly. These errors or residual functions, are defined as:

$$R_\Omega := R\bar{u} - f, \quad x \in \Omega, \tag{2.8a}$$

$$R_{\partial\Omega} := B\bar{u} - g, \quad x \in \partial\Omega. \tag{2.8b}$$

where $\boldsymbol{R}_\Omega$ is the residual associated with the governing equations, and $\boldsymbol{R}_{\partial\Omega}$ is the residual for the boundary conditions. The goal is to determine the coefficients $\{\alpha_j\}$, by minimizing the residuals through weighted integrals. Specifically, the weighted residuals are minimized as follows:

$$\int_\epsilon \mathbf{w}_\Omega^T R_\Omega d\Omega + \int_{\partial\Omega} \mathbf{w}_{\partial\Omega}^T R_{\partial\Omega} d(\partial\Omega), \tag{2.9}$$

In this formulation, $\mathbf{w}_\Omega$ and $\mathbf{w}_{\partial\Omega}$ are weighting functions that depend on the independent variables and are chosen to ensure the integrals are well-defined. In the collocation method, rather than integrating over the entire domain, the residuals are forced to vanish at specific **collocation points** within the domain $\boldsymbol{x}^\Omega = \left\{\boldsymbol{x}_1^\Omega, \cdots, \boldsymbol{x}_{\boldsymbol{n}_1}^\Omega\right\}$ and on the boundary $\boldsymbol{x}^{\partial\Omega} = \left\{\boldsymbol{x}_1^{\partial\Omega}, \cdots, \boldsymbol{x}_{\boldsymbol{n}_2}^{\partial\Omega}\right\}$, The weighting functions in this case are expressed as **Dirac-delta functions** centered at these collocation points:

$$\mathbf{w}_\Omega = \sum_{m=1}^{m_1} \beta_m^\Omega \delta\left(\mathbf{x} - \mathbf{x}_m^\Omega\right), \qquad \mathbf{w}_{\partial\Omega} = \sum_{m=1}^{m_2} \beta_m^{\partial\Omega} \delta\left(\mathbf{x} - \mathbf{x}_m^{\partial\Omega}\right), \tag{2.10}$$

Substituting these weighting functions into the weighted residual equation results in a system of equations for the coefficients $\{\alpha_j\}$ as

$$\mathbf{A}\alpha = \mathbf{b}, \quad \text{with: } \mathbf{A} = \begin{bmatrix} R\boldsymbol{\Phi} \\ B\boldsymbol{\Phi} \end{bmatrix}^T \& \quad \mathbf{b} = \begin{Bmatrix} \mathbf{f} \\ \mathbf{g} \end{Bmatrix}^T, \tag{2.11}$$

Once these coefficients are determined, the approximate solution to the boundary value problem can be obtained using the trial solution.

2.6.2 Formulation of the Singular Boundary Method (SBM)

The Singular Boundary Method (SBM) is a boundary-type numerical approach designed to handle boundary value problems (BVPs) involving partial differential equations (PDEs). Central to the SBM is the use of fundamental solutions $\phi(r)$ as trial functions, which inherently satisfy the governing equations. This solution is expressed as a function of the Euclidean distance r between a field point x and an origin O

$$R(\phi(r)) = -\delta(r), \tag{2.12}$$

In the SBM framework, the approximate solution $u(x)$ for a boundary value problem with a homogeneous source term $f = 0$, can be represented as a linear combination

of fundamental solutions $\phi(\boldsymbol{x}, \boldsymbol{s}j) = \phi\left(\|\boldsymbol{x} - \boldsymbol{s}j\|_2\right)$, centered at a set of source points $\{\boldsymbol{s}_j\}$ located on the physical boundary $\partial\Omega$:

$$\overline{u} = \begin{cases} \sum_{j=1}^{J} \alpha_j \phi\left(\mathbf{x}, \mathbf{s}_j\right), & \mathbf{x} \in \Omega, \\ \sum_{j=1, j\neq m}^{J} \alpha_j \phi\left(\mathbf{x}, \mathbf{s}_j\right) + \alpha_m \beta^m, & \mathbf{x} \in \partial\Omega, \end{cases} \tag{2.13}$$

Where, J is the number of source points and α_j are unknown coefficients. When the collocation points $\{x_m\}$ are positioned to coincide with the source points $\{s_j\}$, the fundamental solutions exhibit singular behavior. To address these singularities, the SBM introduces Origin Intensity Factors (OIFs), $\{\beta^j\}$, which act as regularization parameters to eliminate the singularities effectively.

The primary challenge in SBM lies in determining the OIFs for the associated source points. Over the past decade, several strategies have been developed to compute these factors efficiently. These methods can be categorized into three main approaches:

1. Inverse Interpolation Technique (IIT) [131, 132].
2. Subtracting and Adding-Back Technique (SABT) [134].
3. Integral Mean Value (IMV) Technique [135].

To illustrate these techniques, consider the **Laplace equation** defined within a bounded, homogeneous, isotropic domain Ω^{I} :

$$\nabla^2 u(x) = 0 \text{ for } x \in \Omega^I, \tag{2.14}$$

The boundary conditions consist of Dirichlet conditions on Γ_D and Neumann conditions on Γ_N, such that:

$$\begin{aligned} u(x) &= g_D(x) \quad \text{on } \Gamma_D, \\ \frac{\partial u(x)}{\partial n_x} &= g_N(x) \quad \text{on } \Gamma_N. \end{aligned} \tag{2.15}$$

where, n_x is the outward unit normal vector at the collocation points on the boundary $\partial\Omega^I = \Gamma_D \cup \Gamma_N$. The SBM approximate solution $\bar{u}_L$ for the Laplace problem can be expressed as:

$$\bar{u}_L(x) = \begin{cases} \sum_{j=1}^{J} \alpha_j \phi_L\left(\mathbf{x}, \mathbf{s}_j\right), & \mathbf{x} \in \Omega^I, \\ \sum_{j=1, j\neq m}^{J} \alpha_j \phi_L\left(\mathbf{x}, \mathbf{s}_j\right) + \alpha_m \beta_{L1}^m, & \mathbf{x} \in \partial\Omega^I, \end{cases}$$

$$\frac{\partial \bar{u}_L(x)}{\partial n_x} = \sum_{j=1, j\neq m}^{J} \alpha_j \frac{\partial \phi_L\left(\mathbf{x}, \mathbf{s}_j\right)}{\partial \mathbf{n}_x} + \alpha_m \beta_{L2}^m, \mathbf{x} \in \partial\Omega^I, \tag{2.16}$$

Here, the OIFs β_{L1}^j and β_{L2}^j are applied to regularize the Laplace fundamental solution $\phi_L\left(\mathbf{x}, \mathbf{s}_j\right)$ and its normal derivative $\partial\phi_L\left(\mathbf{x}, \mathbf{s}_j\right)/\partial\mathbf{n}_x$. By incorporating these OIFs, the SBM maintains numerical stability and accuracy while avoiding the computational challenges posed by singularities. This approach has been successfully applied to various boundary value problems, demonstrating its robustness and versatility in handling PDEs with complex boundary conditions.

Chapter 3

Problems Statement

Study of singularities in linear elasticity often draws upon fundamental problems that reveal intricate mathematical behaviors and inform practical engineering solutions. These singularities, while initially perceived as mathematical anomalies, frequently correspond to critical physical phenomena that are essential for understanding failure mechanisms in materials and structures. Here, we introduce two cases of singular stresses in the linear theory of elasticity, both of which challenge conventional frameworks in classical elasticity theory while simultaneously offering opportunities for methodological innovation and deeper insight.

As discussed in Section 4 of Chapter 1, the elimination of stress singularities is often unattainable due to the inherent complexity and constraints of the governing relations. Instead, singularities can be reinterpreted and analysed as intrinsic properties of the system, offering a pathway to extract meaningful insights into stress behavior under extreme conditions. This reinterpretation allows us to move beyond the limitations of classical analytical methods and to approach these singular behaviors with a perspective grounded in both theoretical rigor and practical relevance. By employing this strategy, the present study aims to reinterpret and regenerate solutions to the following problems;

The first problem examines the wedge geometry under a concentrated moment at its vertex, exploring the stress field and its behavior at critical angles where classical solutions fail. The wedge problem is a foundational case in theory of elasticity that has far-reaching applications in modern engineering fields such as fracture mechanics, composite materials, and structural design. Understanding the behavior of singular stresses in a wedge can offer valuable insights into scenarios involving stress concentrations near cracks, notches, and material interfaces.

The second problem investigates the influence of thermal expansion within a sectorial region of an infinite two dimensional elastic plate, focusing on the interplay between material properties and thermal effects that lead to discontinuities in stress and strain. Thermal stresses in elastic materials are critical to numerous engineering applications, including aerospace structures, electronic devices, and composite materials. Understanding how thermal expansion induces stresses in specific regions of a structure helps in predicting failure points and optimizing material design. In particular, the sectorial thermal stress problem serves as a fundamental case for analyzing how localized thermal variations can cause stress discontinuities and potential failure mechanisms. In real-world scenarios, thermal mismatches often arise in components with regions exposed to differential heating, such as turbine blades, welded joints,

or semiconductor devices. Accurate modeling of these thermal stresses is essential for ensuring structural integrity, especially under extreme operating conditions.

Together, these problems provide a framework for understanding singularities not merely as limitations of the model but as critical features that must be addressed to develop robust and applicable solutions.

3.1 First problem: an elastic wedge under the action of a concentrated moment at its vertex

The wedge problem emerged as a pivotal challenge in the early 20th century when engineers and mathematicians sought to understand stress behavior in materials with sharp geometrical features. Carothers [26] was the first to present a solution within linear elasticity theory for an infinitely extending, homogeneous, and isotropic wedge with a total opening angle of 2α, operating under generalized plane stress or plane strain conditions. Independently, Inglis [136] later arrived at the same solution. As depicted in Figure 3.1, the scenario involves applying a concentrated moment M exclusively at the wedge's vertex, while the remaining boundaries are free from any traction.

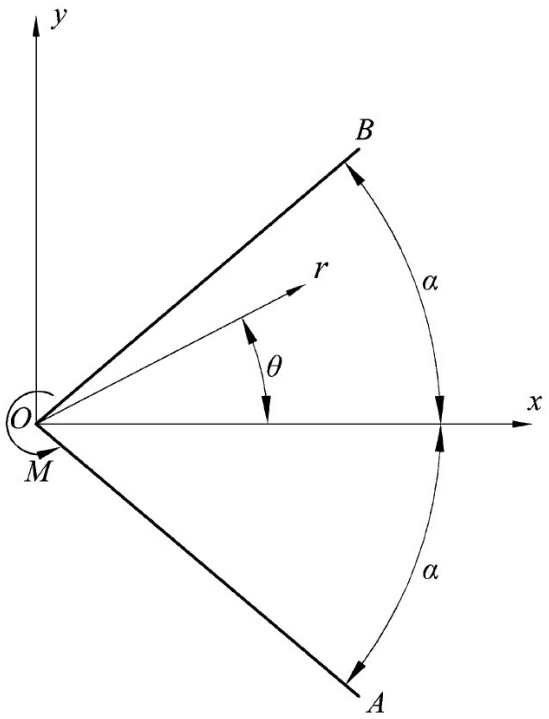

Figure 3.1: The plane linear elasticity problem for an infinite wedge of opening angle 2α loaded at the vertex by forces equipollent to a concentrated couple of moment M, with indication of the polar coordinate system.

In the polar coordinate system (r, θ) illustrated in the same figure, the stress components derived from Carothers' solution can be represented as

$$\sigma_{rr}(r,\theta) = \frac{2M\sin 2\theta}{(\sin 2\alpha - 2\alpha\cos 2\alpha)r^2}, \tag{3.1a}$$

$$\sigma_{\theta\theta}(r,\theta) = 0, \tag{3.1b}$$

$$\sigma_{r\theta}(r,\theta) = \frac{M(\cos 2\alpha - \cos 2\theta)}{(\sin 2\alpha - 2\alpha\cos 2\alpha)r^2}. \tag{3.1c}$$

Interestingly, Sternberg and Koiter [69] highlighted that as the angle α approaches a critical value of $\alpha^* \simeq 0.715\pi$, satisfying the condition $\sin 2\alpha^* - 2\alpha^* \cos 2\alpha^* = 0$, the solution becomes untenable because the stress theoretically becomes infinite throughout the entire structure. This unrealistic phenomenon is commonly referred to as the **wedge paradox**.

The spurious behavior of Carothers' solution at this critical angle has ignited a prolonged debate that continues to this day. Numerous studies [22, 137, 138] have been undertaken in an effort to develop alternative solutions.

In practical applications, a wedge subjected to a concentrated couple at its vertex serves as a fundamental case study for a variety of engineering scenarios. This configuration acts as a mathematical model applicable to numerous situations involving cracks, anti-cracks, notches, bi-material interfaces, and re-entrant corners. In these contexts, the initiation of failure is typically linked to the coefficient associated with the singular component of the stress fields. Consequently, understanding these singularities is crucial not only from a theoretical standpoint but also for practical engineering purposes.

In the current work, we do not introduce a new solution for a wedge experiencing a nonzero tip couple at the critical angle. Instead, connecting to the concept of singularity interpretation (Section 4 of Chapter 1), our focus is on analysing the stress states that exhibit a singularity of order $\mathrm{O}(r^{-2})$. These stress states correspond to the eigenfunctions that Leguillon [77] disregarded because, at the critical angle, they were linked to tip actions with neither a resultant force nor a moment resultant. Our approach eschews complex analytical methods in favour of an intuitive strategy that enhances the visualization of such stress states. Specifically, we demonstrate that when $\alpha = \alpha^*$, the stress state cannot be represented by Equations (3.1a)-(3.1c). This is because it involves the action of a system of dipoles with a zero-moment resultant concentrated at the wedge's vertex. We then propose a generalized framework that eliminates any spurious behavior and remains valid for all opening angles α. Notably, Carothers' solution is retrieved when $\alpha \neq \alpha^*$.

To elucidate our findings, an auxiliary problem will be introduced (Section 1 of Chapter 5) according to that, an elastic wedge with a width of 2α (where $\pi/2 < \alpha < \pi$) is ideally partitioned into three subwedges, each subjected to concentrated couples. The compatibility conditions at the interfaces between these sub-wedges determine the relationship between the applied couples and their moment resultants. Interestingly, at $\alpha = \alpha^*$ this relationship results in a zero-moment resultant, even though the stress state remains nonzero. The derivation of these compatibility conditions, expressed in terms of displacement, utilizes Cesàro's line integral representation, following the methodology outlined by Fosdick and Royer-Carfagni [139, 140], as detailed in the Appendix A. The generalized solution for the wedge will be presented by utilizing an alternative derivation of the stress state through the examination of nuclei of strain, as defined by Love [10]. This approach

considers the influence of two double forces (dipoles) with moments. We confirm that at the critical angle, the moment resultant of these dipoles is zero. This framework not only resolves the wedge paradox but also provides a robust and adaptable solution that can be applied to a wide range of engineering problems involving singular stress fields.

By extending the classical solutions and providing a generalized approach, this study contributes to a deeper understanding of singularities in elastic fields and offers practical tools for addressing these challenges in engineering applications.

3.2 Second problem: an elastic disk under sectorial uniform temperature rise

The problem under consideration involves an infinite, homogeneous, isotropic, linear elastic plate subjected to thermal effects. As shown in Figure 3.2, the plate is modelled in either generalized plane stress or plane strain conditions and is exposed to a uniform temperature increase, ΔT, within a sector of angle 2β (region "I"), contrasting with the remaining part of the plate (region "II"). The material properties of interest include the thermal expansion coefficient α_M, Young's modulus E, elastic shear modulus μ, Poisson's ratio ν, and Kolosov's constant κ, which equals $3 - 4\nu$ for plane strain and $(3 - \nu)/(1 + \nu)$ for generalized plane stress.

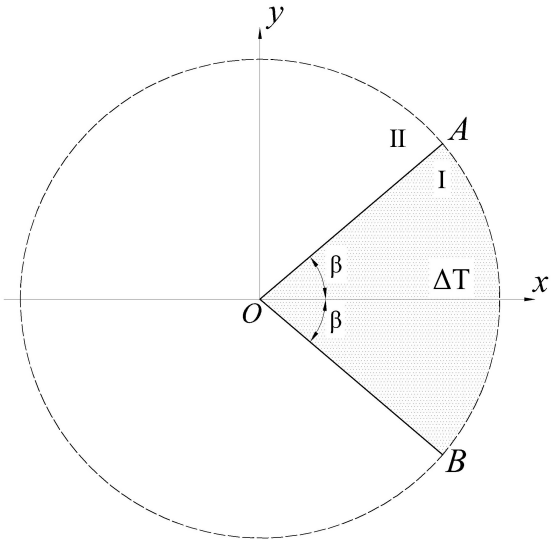

Figure 3.2: Schematic representation of the elastic plate with a sectorial region experiencing a uniform temperature rise of ΔT. The system uses polar coordinates for analysis.

The main objective is to characterize the stress field induced by the thermal expansion of the heated sector. To this end, a polar coordinate system (r, θ) is adopted, where the heated sector is defined as $-\beta \leq \theta \leq \beta$ for $r \geq 0$. The stress components $\sigma_{rr}, \sigma_{\theta\theta}$ and $\sigma_{r\theta}$, along with their corresponding strain components $\varepsilon_{rr}, \varepsilon_{\theta\theta}$ and $\varepsilon_{r\theta}$ are governed by two factors: elastic deformation (derived from Hooke's law) and thermal expansion.

For generalized plane stress, the thermal strain is given by $\varepsilon_{rr}^T = \varepsilon_{\theta\theta}^T = \alpha_M \Delta T$, with $\varepsilon_{r\theta}^T = 0$. The thermal expansion also causes a thickness variation, which could create an out-of-plane mismatch at the interface between regions I and II. However, under the assumption of an infinitesimal plate thickness, this effect is neglected. In contrast, for plane strain, the out-ofplane deformation is constrained, resulting in thermal strains of $\varepsilon_{rr}^T = \varepsilon_{\theta\theta}^T = (1+\nu)\alpha_M \Delta T$ and $\varepsilon_{r\theta}^T = 0$. To unify both cases, an effective coefficient of thermal expansion α is introduced: $\alpha = \alpha_M$ for generalized plane stress and $\alpha = (1+\nu)\alpha_M$ for plane strain.

This problem, with the above-mentioned conditions, governed by the principles of plane linear elasticity, can be expressed using the Airy stress function ϕ, which satisfies the biharmonic equation. Then, the stress components are related to ϕ by:

$$\sigma_{rr} = \frac{1}{r}\frac{\partial \phi}{\partial r} + \frac{1}{r^2}\frac{\partial^2 \phi}{\partial \theta^2}, \tag{3.2a}$$

$$\sigma_{\theta\theta} = \frac{\partial^2 \phi}{\partial r^2}, \tag{3.2b}$$

$$\sigma_{r\theta} = \frac{1}{r^2}\frac{\partial \phi}{\partial \theta} - \frac{1}{r}\frac{\partial^2 \phi}{\partial r \partial \theta}. \tag{3.2c}$$

Since the thermal strain is discontinuous, two Airy stress functions should be defined for regions I and II. However, within each region, since the thermal strain is constant, the stress function shall satisfy the biharmonic equation

$$\Delta\Delta\phi = \left[\frac{1}{r}\frac{\partial}{\partial r}\left(r\frac{\partial}{\partial r}\right) + \frac{1}{r^2}\frac{\partial^2}{\partial \theta^2}\right]^2 \phi = 0 \tag{3.3}$$

Given the lack of an intrinsic length scale in this infinite geometry, the stress field becomes independent of r, leading to spurious behaviours. On the other hand, the thermal variation is applied on an infinite sector which, if not constrained, would imply an infinite displacement for $r \to \infty$. To address this, the problem is approached as the limit of a sequence of subproblems, progressively reducing the thermal mismatch between the heated and unheated regions. While a finite solution exists for the special case $\beta = \pi/2$, the general case yields a divergent limit. Nevertheless, this approach provides insights into approximate solutions for finite geometries, such as a circular disk, where the radius introduces a natural **length scale** and allows for r-dependent solutions.

In the theory of elasticity, a length scale is a characteristic dimension that defines the size or extent of a system or structure under analysis. This concept helps to contextualize and constrain theoretical models, making them applicable to real-world scenarios. In practical terms, the length scale might be defined by:

- The radius of a circular plate or disk.
- The thickness of a thin sheet or beam.
- The distance between supports in structural elements.
- The crack length in fracture mechanics problems.

In infinite or unbounded geometries, the absence of a finite length scale often leads to unbounded displacements or singularities (e.g., stress fields that tend toward infinity). Introducing a finite length scale [141, 142] imposes boundary constraints, which ensure that solutions remain bounded and physically realistic.

In thermoelasticity, where thermal effects induce stresses and deformations in elastic materials, the concept of length scale plays a crucial role. Some key applications include:

- Thermal stress analysis:

In structural elements such as plates, disks, or beams, a finite length scale limits how much the material can expand or contract due to thermal effects. This constraint helps avoid infinite or unrealistic thermal displacements. As an example, in composite structures, different materials may have different thermal expansion coefficients. The interface length scale influences how thermal stresses develop and how mismatches between the materials are managed. Another example in engineering fields can be "Turbine Blades" where, the length scale of a turbine blade dictates how it handles rapid heating and cooling cycles in jet engines. Also in welded Joints that the dimensions of the weld and surrounding material influence how thermal stresses are distributed during cooling. In a similar scenario, when a structure experiences localized heating (e.g., a sector of a plate), the finite boundaries influence how thermal stresses are distributed. The length scale determines the extent to which thermal mismatches between heated and unheated regions affect the overall stress field.

- Fracture and failure analysis:

In fracture mechanics, the length scale associated with a crack tip or a defect helps predict how thermal stresses will influence crack propagation. Finite geometries ensure that stress intensity factors remain meaningful.

- Material behavior in small structures:

In micro-electro-mechanics and nano-technology, components often have extremely small length scales. Thermal effects at these scales are significant, and the finite dimensions constrain how materials respond to thermal loads.

The subsequent discussion underscores the delicate balance between mathematical rigor and practical engineering relevance, emphasizing the importance of extracting actionable insights from theoretical models. While precise mathematical solutions provide a robust framework for understanding the problem, they often involve complexities that may obscure their practical implications. This interplay between precision and applicability opens avenues for extending the derived solutions to a broader range of engineering scenarios, including finite and non-ideal geometries.

To bridge the gap between theory and application, it is beneficial to first analyze the qualitative aspects of the problem. By employing dimensional analysis, we can uncover fundamental relationships and scaling laws that govern the systems' behavior. This approach not only simplifies the interpretation of the results but also offers a pathway to identify critical parameters influencing the thermal stress field. Consequently, this preliminary investigation lays a foundation for understanding the core physical principles before moving to the precise mathematical formulations that capture the finer details of the problem.

Chapter 4

Considerations From Dimensional Analysis

The core concept behind dimensional analysis is remarkably straightforward: physical laws remain unaffected by the arbitrary selection of measurement units. From this foundational idea, a key conclusion arises through a simple reasoning process: the mathematical expressions describing physical laws must exhibit a fundamental property known as generalized homogeneity or symmetry. This property simplifies complex mathematical expressions by reducing the number of variables involved, thereby facilitating their derivation-whether through calculation or experimentation. This principle encapsulates the essence of dimensional analysis. Despite its simplicity, the method has led to profound scientific discoveries that have transformed entire fields. The tools required to apply dimensional analysis are accessible and straightforward, as evidenced by its application by luminaries such as Newton, Fourier, Maxwell, and Rayleigh [143].

4.1 Correlation with self-similarity

Scaling, or power-law relationships, finds widespread application in science and engineering. A basic example is the scaling law for velocity distribution u near a wall in turbulent shear flow, expressed as $u = Ay^n$, where y is the distance from the wall, and A and n are constants.

Although often viewed as mere approximations of experimental data, scaling laws hold deeper significance: they reflect the **self-similarity** inherent in the phenomena under study. Self-similar systems replicate their structure across time and space. This concept first emerged in mathematical physics, notably in Fourier's work on heat conduction [143]. Fourier introduced the "source-type" solution as

$$\theta(x,t) = \frac{A}{\sqrt{t}} f\left(\frac{x}{\sqrt{t}}\right), \quad f(\xi) = e^{-\xi^2/4}, \tag{4.1}$$

where, A is a constant, for the heat conduction equation of

$$\frac{\partial \theta}{\partial t} = \frac{\partial^2 \theta}{\partial x^2}, \tag{4.2}$$

As problems and their mathematical models grew increasingly complex-often in-

volving nonlinearity-finding self-similar solutions became a significant achievement, particularly before the advent of computational methods. These solutions simplified analysis by reducing partial differential equations to ordinary differential equations. In self-similar coordinates, such as $x/\sqrt{t}$, phenomena appear time-independent, providing insights into stabilization processes. For many problems, selfsimilar solutions were crucial to understanding qualitative behavior.

Dimensional analysis plays a critical role in determining the exponents in self-similar variables, as seen in the heat conduction example. However, finding these exponents is not always straightforward. Barenblatt and Sivashinsky [144, 145] investigated cases where a parameter intrinsic to the problem's formulation influenced the results. For a specific value of this parameter, classical self-similar solutions emerged, with exponents deduced from dimensional considerations. In contrast, for other parameter values, "anomalous dimensions" arose as continuous functions of the parameter, determined through solving a nonlinear eigenvalue problem. These findings clarified the distinction between two types of self-similar solutions.

Self-similar solutions generally represent "intermediate asymptotics", valid when the influence of initial and boundary conditions has faded, but the system remains far from equilibrium. The complexity in determining exponents stems from the nature of these asymptotics. If the asymptotics approach a finite limit, **self-similarity of the first kind** occurs. When no finite limit exists, but the asymptotics follow a power-law scaling influenced by pre-self-similar behavior, **self-similarity of the second kind** arises.

This discussion draws extensively from Barenblatt's seminal work, including his analysis of equilibrium on an elastic wedge under a concentrated tip couple, as outlined in Section 1 of Chapter 9 in [143]. Using Barenblatt's approach, two singular problems, previously introduced in chapter 3 of the study at hand are investigated.

4.2 First problem: elastic wedge

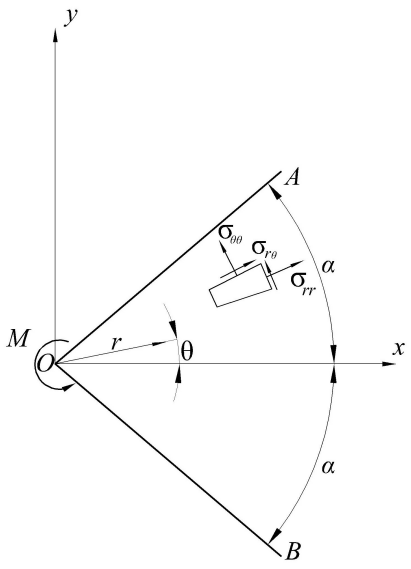

Figure 4.1: An infinite elastic wedge subjected to a concentrated couple at the tip.

This section examines an infinite elastic wedge with an opening angle of 2α, subjected to a concentrated moment M at its apex, as illustrated in Figure 4.1. The elastic field in this setup is characterized by a stress function, ψ, which depends on the parameters M, r, θ, and α. These variables have the following dimensional attributes: M corresponds to force (F), r to length (L), while θ and α are dimensionless. It is noteworthy that in plane elasticity, the moment of a couple shares the same dimension as force because the problem is inherently two-dimensional, implying force per unit thickness.

The components of stress in this system are expressed using the Airy stress function, ψ, as follows:

$$\sigma_{rr} = \frac{1}{r}\frac{\partial \psi}{\partial r} + \frac{1}{r^2}\frac{\partial^2 \psi}{\partial \theta^2}, \tag{4.3a}$$

$$\sigma_{\theta\theta} = \frac{\partial^2 \psi}{\partial r^2}, \tag{4.3b}$$

$$\sigma_{r\theta} = \frac{1}{r^2}\frac{\partial \psi}{\partial \theta} - \frac{1}{r}\frac{\partial^2 \psi}{\partial r \partial \theta}. \tag{4.3c}$$

The equilibrium equations governing the plane strain state are:

$$\frac{\partial}{\partial r}\left(\sigma_{rr}\right) + \frac{1}{r}\frac{\partial}{\partial \theta}\left(\sigma_{r\theta}\right) + \frac{1}{r}\left(\sigma_{rr} - \sigma_{r\theta}\right) = 0, \tag{4.4a}$$

$$\frac{\partial}{\partial r}\left(\sigma_{r\theta}\right) + \frac{1}{r}\frac{\partial}{\partial \theta}\left(\sigma_{\theta\theta}\right) + \frac{2}{r}\left(\sigma_{r\theta}\right) = 0. \tag{4.4b}$$

From these equations, the stress function ψ is inferred to have the dimension of force. Subsequently, using dimensional analysis, a specific relationship is established:

$$\psi = M\phi(\alpha, \theta), \tag{4.5}$$

While the stress function is independent of r, substituting the relations (4.3) into equilibrium equations of (4.4), results the biharmonic equation

$$\Delta^2 \psi = \left[\frac{1}{r}\frac{\partial}{\partial r}\left(r\frac{\partial}{\partial r}\right) + \frac{1}{r^2}\frac{\partial^2}{\partial \theta^2}\right]^2 \psi = 0, \tag{4.6}$$

Then, replacing (4.5) into (4.6) yields to the following equation for ϕ

$$\phi^{\mathrm{IV}} + 4\phi'' = 0, \tag{4.7}$$

To solve this differential equation specific boundary conditions should be satisfied. These include ensuring that the faces of the wedge are traction-free:

$$\sigma_{\theta\theta}\left(r, \pm\alpha\right) = \sigma_{r\theta}\left(r, \pm\alpha\right) = 0, \tag{4.8}$$

Also, from (4.3) and (4.5) one can obtain

$$\frac{\partial \phi}{\partial \theta}|_{(\theta=\pm\alpha)} = 0, \tag{4.9}$$

Previously, in Section 1 of Chapter 3, the stress state associated with this problem was described using Equations (3.1a)-(3.1c). It is now essential to elaborate on the process that led to the adoption of the Airy stress function (4.10). This procedure as mentioned in [26, 136] includes the following three steps:

- Firstly, a circular cut of arbitrary radius is made.
- Secondly, the total moment of the stresses acting on this cut is calculated.
- Finally, the result is equated to M, ensuring equilibrium state of the removed part of the wedge that leads to

$$\phi = \frac{M(2\theta\cos 2\alpha - \sin 2)}{2(\sin 2\alpha - 2\alpha\cos 2\alpha)}, \tag{4.10}$$

In Section 1 of Chapter 3, the anomalous behavior of the stress state derived from Equation (4.10) was previously examined. Specifically, when the wedge's opening angle is $\alpha = \alpha^* = 0.715\pi$, the stress state diverges to infinity. Connecting to the concept of self-similar behaviour of second type, this raises an important question: Can the self-similar solution of the idealized problem described by Equation (4.10) serve as an asymptotic representation of a non-self-similar solution for a more realistic, non-idealized problem? In other words, does this solution hold any intrinsic physical significance?

Sternberg and Koiter [69] addressed the limitations of the idealized model by studying a non-self-similar scenario. Here, a distributed normal load is applied over finite segments of the wedge's lateral faces, as shown in Figure 4.2. This loading is statically equivalent to a couple producing moment M, while the tangential stress remains zero along the wedge flanks.

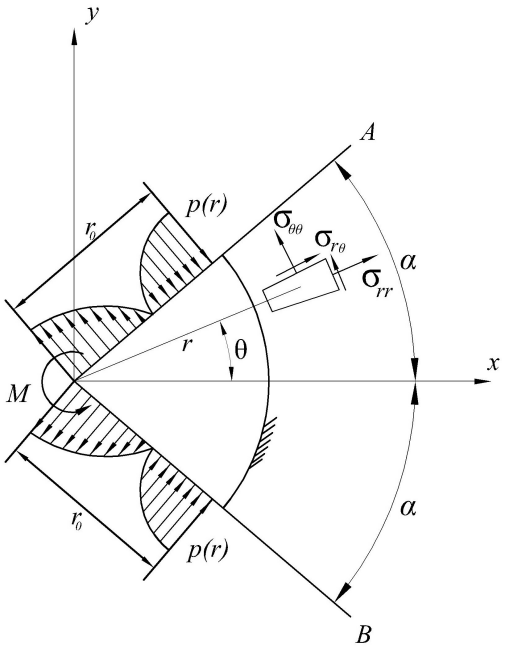

Figure 4.2: non-idealized problem of a wedge under the action of a moment M at the tip [26].

For this configuration, the boundary conditions are expressed as:

$$\begin{aligned} \sigma_{\theta\theta}(r,\alpha) &= -\sigma_{\theta\theta}(r,-\alpha) = p(r), \\ \sigma_{\tau\theta}(r,\alpha) &= \sigma_{r\theta}(r,-\alpha) \equiv 0 \quad (0 < r < \infty). \end{aligned} \tag{4.11}$$

Wherein, $p(r)$ vanishes outside the loaded segments $r \geq r_0$ and satisfies the following

$$\int_0^{r_0} p(r)dr = 0, \quad \int_0^{r_0} p(r)rdr = \frac{M}{2}, \tag{4.12}$$

Additionally, the uniqueness of solution must be guaranteed by imposing the boundedness of the resultant force on any radial cut through the wedge

$$\int_0^{\infty} \sigma_{\theta\theta}(r,\theta)dr < \infty, \quad \int_0^{\infty} \sigma_{r\theta}(r,\theta)dr < \infty, \tag{4.13}$$

Taking into consideration the above-mentioned conditions and utilizing the and Mellin transformation [146] to the biharmonic equation (4.6), Sternberg and Koiter [69] obtained the stress state for the non-idealized problem through solving the transformed ordinary differential equation. Depend on the governing parameter α, their findings reveal three distinct solutions for; $0 < \alpha < \alpha^*$ which is the same as Equation (3.1), $\alpha = \alpha^*$ and $\alpha^* < \alpha$.

Connecting to Sternberg's solution for the non-self-similar problem, Barenblatt [143], investigated the same problem using dimensional analysis. Considering the effect of the r_0 on the stress state, the stress function ψ is modified to account for it. So, it can be expressed first by introducing the distributed load in the form:

$$p(r) = \frac{M}{2r_0^2}\varphi\left(\frac{r}{r_0}\right), \tag{4.14}$$

Utilizing $p(r)$, one can realize that the stress function ψ, will be governed by the parameters listed in Table 4.1.

Parameter	Description	Dimension
M	moment	F
r_0, r	radius	L
θ, α	angle	1
φ	distribution function	1

Table 4.1: governing quantities of stress function ψ for the non-idealized problem in Figure 4.2.

Consequently, implementing the standard procedure of dimensional analysis yields

$$\Psi = M\Phi\left(\frac{r}{r_0}, \theta, \alpha\right), \tag{4.15}$$

It should be noted that the derivation of equation (4.5) relied on the implicit assumption that r/r_0, is extremely large at considerable distances from the wedge tip. As a result, the length r_0, which corresponds to the segment of the wedge's lateral surface where the load is applied, becomes a negligible factor.

Barenblatt's findings demonstrated that the assumption is valid only within the range $0 < \alpha < \alpha^*$. For $\alpha > \alpha^*$, the parameter r_0 retains its importance, irrespective of how far one moves from the wedge tip. Despite this, the stress function and all stress tensor components display self-similar behavior. This self-similarity, is of the second kind so cannot be addressed via dimensional analysis.

In other words, for $\alpha^* < \alpha \leq \pi$, when the loaded area shrunk to zero, in order to preserving the effect of the distributed load equal to M, though the solution shows an asymptotic behavior but in a more complicated way, this behavior is in correlation with a more complex fractional power moment of the acting load on the wedge's flanks, not the ordinary one given by Equation (4.12). Regarding that, Barenblatt [143] suggested a more general form of stress function like

$$\Psi = \mathrm{M} \left(\frac{r_0}{r}\right)^{\lambda} \Phi_1(\theta, \alpha)\,, \tag{4.16}$$

Inserting (4.16) into (4.6) results

$$\Phi_1^{IV} + \left[\lambda^2 + (\lambda+2)^2\right] \Phi_1'' + \lambda^2(\lambda+2)^2 \Phi_1 = 0\,, \tag{4.17}$$

Finally, it is shown that the characteristic equation of Equation (4.17), for both ranges of $0 < \alpha < \alpha^*$, and $\alpha^* < \alpha < \pi$, has the real roots (λ). So, the exponent to which the radius appears in the moment depends on the opening angle of the wedge α, and is determined by solving the eigenvalue problem for the linear Equation of (4.17) under the conditions that the solution and its derivative vanish at the endpoints of the interval.

In conclusion to this part, it is noteworthy to emphasize on the key role of dimensional analysis in study of wedge problem. The analysis highlights the significance of the wedge angle α in determining the solution's behaviour. For $\alpha < \alpha^*$, dimensional analysis suffices, yielding a self-similar solution of the first kind (3.1a)-(3.1c) based on the prescribed moment of forces (4.12). However, for $\alpha > \alpha^*$ dimensional arguments fail because r_0 cannot be excluded from the governing parameters. In this case, a selfsimilar solution of the second kind emerges, determined only up to a constant, which is resolved by matching with a non-self-similar solution and expressed in terms of a fractional moment. For the critical angle $\alpha = \alpha^*$, dimensional considerations and similarity arguments break down entirely, as no simplification of the solution is possible, regardless of the scale of the loading region.

4.3 Second problem: elastic disk

Building upon the second problem outlined in Section 2 of Chapter 3, the Airy stress function ϕ depends on parameters: $r, \theta, \beta, \Delta T, \alpha$ (the effective coefficient of thermal expansion), and a material elasticity parameter $\mathcal{E}$, which characterizes the elasticity of the material and shares the dimensionality of an elastic modulus. To analyze the

problem systematically using dimensional analysis, the governing parameters and their dimensions are introduced as in Table 4.2.

Parameter	Description	Dimension
F	force	F
ϕ	stress function	F
$\mathcal{E}$	elasticity factor	FL^{-2}
r	radius	L
θ, β	angle	1
α	thermal expansion coefficient	θ^{-1}
ΔT	temperature change	θ

Table 4.2: governing quantities of stress function ψ for the problem introduced in Figure 3.2.

Using standard dimensional analysis, we obtain the following non-dimensional form of the Airy stress function:

$$\frac{\phi}{\varepsilon r^2} = \alpha \Delta T \Phi(\theta, \beta), \tag{4.18}$$

This form reflects the linear dependence of the stress state on ΔT, a consequence of the linearity of the governing equations. Defining $\Phi' = \partial\Phi/\partial\theta$, substituting (4.18) into the biharmonic equation (3.3) yields:

$$\Phi^{IV} + 4\Phi'' = 0, \tag{4.19}$$

This differential equation governs the behavior of the stress function in both regions "I" and "II" (as depicted in Figure 3.2). While the stress field remains continuous across these regions, the interface at $\theta = \pm\beta$, may exhibit discontinuities in other quantities due to differences in thermal expansion. Thus, two distinct Airy stress functions, ϕ^I and ϕ^{II}, are introduced, each of the form:

$$\phi^I = \alpha \Delta T \mathcal{E} r^2 \left[C_1^I + C_2^I \theta + C_3^I \cos(2\theta) + C_4^I \sin(2\theta)\right], \tag{4.20a}$$

$$\phi^{II} = \alpha \Delta T \mathcal{E} r^2 \left[C_1^{II} + C_2^{II} \theta + C_3^{II} \cos(2\theta) + C_4^{II} \sin(2\theta)\right]. \tag{4.20b}$$

Here, C_i^I and $C_i^{II}, i = 1 \dots 4$ are coefficients dependent on the sector angle β. Using (3.2), the stress components in region S ($S = I$ or $S = II$) can be expressed as:

$$\sigma_{rr}^S = 2\alpha \Delta T \mathcal{E} \left[C_1^S + C_2^S \theta - C_3^S \cos(2\theta) - C_4^S \sin(2\theta)\right], \tag{4.21a}$$

$$\sigma_{\theta\theta}^S = 2\alpha \Delta T \mathcal{E} \left[C_1^S + C_2^S \theta + C_3^S \cos(2\theta) + C_4^S \sin(2\theta)\right], \tag{4.21b}$$

$$\sigma_{r\theta}^S = -\alpha \Delta T \mathcal{E} \left[C_2^S - 2C_3^S \sin(2\theta) + 2C_4^S \cos(2\theta)\right]. \tag{4.21c}$$

Continuity of the displacement field and of the stress vector on interface surfaces

$\theta = \pm\beta$ need to be added. These provide a liner system of 8 equations in the unknown 8 parameters $C_i^S, i = 1 \dots 4, S = I,\, II$.

To ensure physical continuity across the interface at $\theta = \pm\beta$, additional boundary conditions must be satisfied. These include:

4.3.1 Continuity of circumferential stress

$$\begin{aligned}&\sigma^I_{\theta\theta}|_{\theta=\beta} = \sigma^{II}_{\theta\theta}|_{\theta=\beta} \Rightarrow (C_1^I - C_1^{II}) \\ &+ (C_2^I - C_2^{II})\beta + (C_3^I - C_3^{II})\cos(2\beta) + (C_4^I - C_4^{II})\sin(2\beta) = 0\,,\end{aligned} \tag{4.22a}$$

$$\begin{aligned}&\sigma^I_{\theta\theta}|_{\theta=-\beta} = \sigma^{II}_{\theta\theta}|_{\theta=-\beta} \Rightarrow (C_1^I - C_1^{II}) \\ &- (C_2^I - C_2^{II})\beta + (C_3^I - C_3^{II})\cos(2\beta) - (C_4^I - C_4^{II})\sin(2\beta) = 0\,.\end{aligned} \tag{4.22b}$$

4.3.2 Continuity of shear stress:

$$\begin{aligned}&\sigma^I_{r\theta}|_{\theta=\beta} = \sigma^{II}_{r\theta}|_{\theta=\beta} \\ &\Rightarrow (C_2^I - C_2^{II}) - 2(C_3^I - C_3^{II})\sin(2\beta) + 2(C_4^I - C_4^{II})\cos(2\beta) = 0\,,\end{aligned} \tag{4.23a}$$

$$\begin{aligned}&\sigma^I_{r\theta}|_{\theta=-\beta} = \sigma^{II}_{r\theta}|_{\theta=-\beta} \\ &\Rightarrow (C_2^I - C_2^{II}) + 2(C_3^I - C_3^{II})\sin(2\beta) + 2(C_4^I - C_4^{II})\cos(2\beta) = 0\,.\end{aligned} \tag{4.23b}$$

Note that the calculations can be streamlined by exploiting symmetry: the shear stress vanishes at $\theta = 0$ and $\theta = \pi$, which directly yields, from (4.21)

$$\sigma^I_{r\theta}|_{\theta=0} = 0 \Rightarrow C_2^I + 2C_4^I = 0\,, \tag{4.24a}$$

$$\sigma^{II}_{r\theta}|_{\theta=\pi} = 0 \Rightarrow C_2^{II} + 2C_4^{II} = 0\,. \tag{4.24b}$$

4.3.3 Interface conditions

The continuity of displacement at $\theta = \pm\beta$ can be determined using the methodology outlined in [147], and exactly presented in the Appendix A, which employs Cesaro's line integral representation as discussed in [139, 140]. Noting that the shear stress $\sigma_{r\theta}$, and the corresponding shear strain $\varepsilon_{r\theta}$ remain continuous at the interface and are independent of r, the conditions for the radial and circumferential displacements, u_r and u_θ, can be expressed as follows:

$$u_r^I|_{\theta=\pm\beta} = u_r^{II}|_{\theta=\pm\beta} \Rightarrow \varepsilon^I_{rr}|_{\theta=\pm\beta} = \varepsilon^{II}_{rr}|_{\theta=\pm\beta}, \tag{4.25a}$$

$$u_\theta^I|_{\theta=\pm\beta} = u_\theta^{II}|_{\theta=\pm\beta} \Rightarrow \frac{\partial}{\partial\theta}\varepsilon_{rr}^I|_{\theta=\pm\beta} = \frac{\partial}{\partial\theta}\varepsilon_{rr}^{II}|_{\theta=\pm\beta}, \tag{4.25b}$$

From the continuity conditions for the shear stress in (4.23), we derive the following relationship:

$$\left(C_3^I - C_3^{II}\right)\sin(2\beta) = 0, \tag{4.26}$$

For cases where $\beta \neq \pi/2$, this implies:

$$C_3^I = C_3^{II}, \tag{4.27}$$

Using this result in conjunction with the conditions in (4.23) and (4.24), it can be shown that:

$$C_2^I = C_2^{II}, \quad \text{and} \quad C_4^I = C_4^{II}, \tag{4.28}$$

Substituting these into (4.22) reveals that:

$$C_1^I = C_1^{II}\,, \tag{4.29}$$

Thus, the coefficients determining the stress components are identical in regions "I" and "II." Furthermore, condition (4.25b) is naturally satisfied. However, this conclusion is incompatible with condition (4.25a). Specifically, for generalized plane stress (with analogous behavior for plane strain), a discontinuity in the radial stress arises at the interface, expressed as:

$$\left[\sigma_{rr}^{II} - \sigma_{rr}^I\right]_{\theta=\pm\beta} = E\alpha\Delta T, \tag{4.30}$$

In conclusion to this part, dimensional analysis suggests that the stress components are a function of θ alone, due to the absence of a natural length scale in this infinite geometry. However, this lack of dependence on r, leads to unrealistic physical outcomes, such as the discontinuity in radial stress described in (4.30). To address these inconsistencies, a length scale must be introduced into the problem. For example, the radius of a finite disk could serve as a characteristic length, allowing for stress solutions that vary with r. This adjustment ensures a more physically accurate representation of the stress field.

In chapter 6, the problem is reformulated through a sequence of subproblems, where the thermal mismatch at the interface is gradually reconciled. This iterative approach ultimately provides a consistent and physically meaningful solution.

Chapter 5

Analytical Solution to The First Problem

5.1 Generalized solution of the wedge (Carothers') problem

Figure 5.1 depicts an infinite two-dimensional wedge with a total opening angle 2α, where $\pi < 2\alpha < 2\pi$. The system is subjected to actions equivalent to a concentrated couple with a resultant moment M, applied at its vertex. The boundaries of the wedge, denoted by $\overline{OA}$ and $\overline{OB}$, are assumed to be traction-free. For the analysis, first consider the case where $\alpha \neq \alpha^*$. From Equation (3.1c), the tangential stress component $\sigma_{r\theta}$ can be expressed as:

$$\sigma_{r\theta}(r,\theta) = \frac{M(\cos 2\alpha - \cos 2\theta)}{(\sin 2\alpha - 2\alpha\cos 2\alpha)r^2} = 0 \Rightarrow \cos 2\theta = \cos 2\alpha\,, \tag{5.1}$$

This condition is satisfied when $\cos 2\theta = \cos 2\alpha$. This implies that $\theta = \pm\alpha$ and $\theta = \pm(\pi - \alpha)$. The lines $\theta = \pm\alpha$, correspond to the traction-free surfaces of the wedge, while $\theta = \pm(\pi - \alpha)$ are identified as complementary lines $\overline{OC}$ and $\overline{OD}$, as shown in Figure 5.1. These lines remain traction-free, as verified by equation (3.1b), where $\sigma_{\theta\theta}(r,\theta) = 0$ at every point.

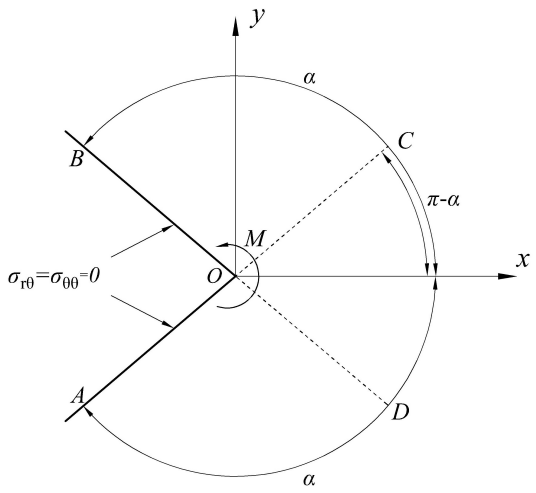

Figure 5.1: A wedge with opening angle of $\pi < 2\alpha < 2\pi$, under the action of a concentrated couple M at its tip.

The above observations suggest that an alternative approach to solving this problem involves partitioning the original wedge (Figure 5.1), into three sub-wedges. These sub-wedges are defined by the traction-free boundaries of the original system. This division is illustrated in Figure 5.2. In this configuration, the wedge is split into:

1. Central Wedge (I): This wedge has a width of 2β, with $\beta = \pi - \alpha$. A concentrated moment M_1 is applied at its tip.

2. Side Wedges (II): These two wedges have opening angles of $\pi - 2\beta$ and both are subjected to moment M_2 applied at their respective vertices.

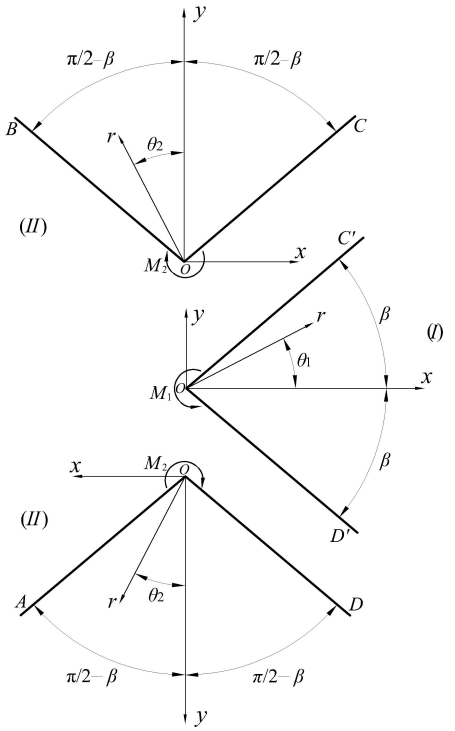

Figure 5.2: Ideal splitting of the body into three sub-wedges, defined by the traction-free lines for original wedge problem of width 2α, with $\pi/2 < \alpha < \pi$ and $\beta = \pi - \alpha$.

To reconcile the solution for the sub-wedges with the original wedge problem, it is essential to determine the values of M_1 and M_2. These values ensure that the three sub-wedges can be "welded" back together seamlessly, maintaining compatibility and continuity of displacements and tractions across the boundaries. Specifically, the following conditions must be satisfied:

1. Traction Continuity: The stresses along the interfaces $\overline{OC}$ with $\overline{OC'}$ and $\overline{OD}$ with $\overline{OD'}$ must match.

2. Displacement Compatibility: The displacements along these boundaries must also be continuous.

Additionally, the total moment M of the original wedge must equal the combined moments applied to the sub-wedges, such that; $M = M_1 - 2M_2$.

The stress state for each part is provided by (3.1a)-(3.1c). With the notation of Figure 5.1, on wedge I, for $-\beta \leq \theta_1 \leq \beta$ one has

$$\sigma_{rr}^{(1)}(r,\theta_1) = \frac{2M_1 \sin 2\theta_1}{(\sin 2\beta - 2\beta\cos 2\beta)r^2}\,, \tag{5.2a}$$

$$\sigma_{\theta\theta}^{(1)}(r,\theta_1) = 0\,, \tag{5.2b}$$

$$\sigma_{r\theta}^{(1)}(r,\theta_1) = \frac{M_1(\cos 2\beta - \cos 2\theta_1)}{(\sin 2\beta - 2\beta\cos 2\beta)r^2}\,. \tag{5.2c}$$

In case of the wedges II, for $\beta - \pi/2 \leq \theta_2 \leq \pi/2 - \beta$, substitution of $\alpha = \pi/2 - \beta$ into (3.1a)-(3.1c) provides

$$\sigma_{rr}^{(2)}(r,\theta_2) = -\frac{2M_2 \sin 2\theta_2}{[\sin(\pi - 2\beta) - (\pi - 2\beta)\cos(\pi - 2\beta)]\, r^2}\,, \tag{5.3a}$$

$$\sigma_{\theta\theta}^{(2)}(r,\theta_2) = 0\,, \tag{5.3b}$$

$$\sigma_{r\theta}^{(2)}(r,\theta_2) = -\frac{M_2\,(\cos(\pi - 2\beta) - \cos 2\theta_2)}{[\sin(\pi - 2\beta) - (\pi - 2\beta)\cos(\pi - 2\beta)]\, r^2}\,. \tag{5.3c}$$

Clearly, since $0 < \beta < \pi$, these stress representations are consistent and valid.

5.1.1 Traction continuity

Traction continuity along the inclined boundaries is inherently satisfied. Specifically, from Equations (5.2) and (5.3), the following conditions hold:

$$\sigma_{r\theta}^{(1)}(r,\pm\beta) = \sigma_{r\theta}^{(2)}(r,\mp(\pi/2 - \beta)) = 0\,, \tag{5.4a}$$

$$\sigma_{\theta\theta}^{(1)}(r,\pm\beta) = \sigma_{\theta\theta}^{(2)}(r,\mp(\pi/2 - \beta)) = 0\,. \tag{5.4b}$$

5.1.2 Displacement compatibility

To ensure a seamless transition between the sub-wedges, displacement compatibility must also be maintained along the interfaces $\overline{OC}$ with $\overline{OC'}$ and $\overline{OD}$ with $\overline{OD'}$. Using Hooke's law, the strain field can be expressed in terms of the stress field, allowing compatibility conditions to be derived. These conditions were extensively analyzed by Fosdick and Royer-Carfagni [139, 140], such as those relying on Cesaro's integral representation, as proposed in [148]. The details of this method, along with the required expressions in polar coordinates, are available in the Appendix A.

As illustrated in Figure 5.3, two radial paths converge on the lines, $\overline{OC}$ and $\overline{OC'}$ (and similarly on $\overline{OD}$ and $\overline{OD'}$)). Along these paths, the strain field components for the respective sub-wedges I and II can be denoted as $\varepsilon_{ij}^{(1)}(r,\theta_1)$ and $\varepsilon_{ij}^{(2)}(r,\theta_2)$ wherein $i,j = r,\theta$. By analyzing these components, displacement continuity at the interfaces can be guaranteed.

The displacement field components for each sub-wedge, both radial (v_r) and tangential (v_θ), are derived in Appendix A, Equations (A.5) and (A.8), respectively. Since the stress component $\sigma_{\theta\theta}$ is zero, the radial strain ε_{rr} is simplified as $\varepsilon_{rr} = \sigma_{rr}/E'$, where E is the Young's modulus. Depending on the problem type, E

can be modified for generalized plane stress as $E' = E$ or $E' = E/(1 - v^2)$ for plane strain conditions. Here, v represents the Poisson's ratio of the material.

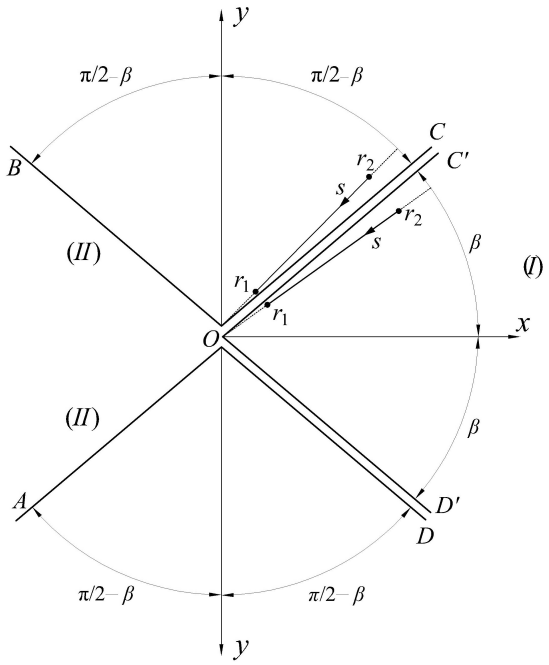

Figure 5.3: The two radial paths for Cesaro's integral representation, tending to the common lines $\overline{OC}$ and $\overline{OC}$, on wedges II and I, respectively.

These considerations lead to the following continuity conditions at the interfaces:

$$\sigma_{rr}^{(1)}(r, \beta^-) = \sigma_{rr}^{(2)}(r, -(\pi/2 - \beta)^+)\,, \tag{5.5a}$$

$$\sigma_{rr,\theta_1}^{(1)}(r, \beta^-) = \sigma_{rr,\theta_2}^{(2)}(r, -(\pi/2 - \beta)^+)\,. \tag{5.5b}$$

Taking into account the expressions (5.2a)-(5.2c) and (5.3a)-(5.3c), from (5.5a) one obtains the condition

$$\frac{2M_1 \sin 2\beta}{(\sin 2\beta - 2\beta\cos 2\beta)r^2} = -\frac{2M_2 \sin(2\beta - \pi)}{[\sin(\pi - 2\beta) - (\pi - 2\beta)\cos(\pi - 2\beta)]r^2}\,, \tag{5.6}$$

This relationship establishes the following formula linking the moments M_1 and M_2:

$$M_2 = M_1 \left[1 + \frac{\pi \cos 2\beta}{\sin 2\beta - 2\beta\cos 2\beta}\right]\,. \tag{5.7}$$

The same result will be obtained from (5.5b). Then, the total moment at the tip of the three subwedges is represented as:

$$M = M_1 - 2M_2 = M_1 \frac{\sin 2\beta + 2(\pi - \beta)\cos 2\beta}{2\beta\cos 2\beta - \sin 2\beta}, \tag{5.8}$$

It is particularly insightful to evaluate this expression at $\beta = \beta^* = \pi - \alpha^*$, where $\alpha^* \simeq 0.715\pi$, denotes the critical angle for the wedge problem, as previously detailed in Section 1 of Chapter 3. This critical angle satisfies the condition $\sin 2\alpha^* - 2\alpha^* \cos 2\alpha^* = 0$. At this specific value of β, the configuration obtained by joining the three sub-wedges seamlessly mirrors the original setup associated with the wedge paradox. What is particularly noteworthy is that at $\beta = \beta^*$, the relationship between M_1 and M_2, as defined by Equation (5.7), remains entirely coherent. Importantly, none of the stress component expressions, as given in Equations (5.2a)-(5.2c) and (5.3a)-(5.3c), exhibit any unbounded growth, ensuring a physically meaningful solution.

It is crucial to emphasize, however, that at $\beta = \beta^*$, the resultant moment M of the applied couples reduces to zero, as demonstrated by Equation (5.8). This implies that the following relationship holds: $M_1 = 2M_2$. This critical observation underlines the significance of the auxiliary problem, as it elegantly resolves the singularity issues while maintaining consistency with the physical constraints of the original wedge problem.

Using Equation (5.7), the stress component expressions from Equations (5.2a)-(5.2c) and (5.3a)-(5.3c) can be combined into a single, more compact form. Setting $\beta = \pi - \alpha, \theta_1 = 0$ in Equations (5.2a)-(5.2c), and $\theta_2 = \theta - \pi/2$ in Equations (5.3a)-(5.3c), we obtain a unified representation of the stress field that is valid for $-\alpha \leq \theta \leq \alpha$:

$$\sigma_{rr}(r,\theta) = \frac{2M_1 \sin 2\theta}{(-\sin 2\alpha + 2(\alpha - \pi)\cos 2\alpha)\, r^2}\,, \tag{5.9a}$$

$$\sigma_{\theta\theta}(r,\theta) = 0\,, \tag{5.9b}$$

$$\sigma_{r\theta}(r,\theta) = \frac{M_1(\cos 2\alpha - \cos 2\theta)}{(-\sin 2\alpha + 2(\alpha - \pi)\cos 2\alpha)\, r^2}\,. \tag{5.9c}$$

These expressions are valid for $\pi/2 < \alpha < \pi$, and here M_1 represents the couple applied to sub-wedge I, as per the configuration in Figure 5.2. This formulation demonstrates that, regardless of the opening angle α, the stress state is both well-defined and free of nonphysical behavior.

We conclude that analyzing the wedge problem with a width of 2α, where $\pi/2 < \alpha < \pi$, through the auxiliary formulation involving three sub-wedges (as depicted in Figure 5.2), reveals no anomalous behavior, irrespective of the angle α. The stress state is consistently described by Equations (5.2a)-(5.2c) and (5.3a)-(5.3c), with the conditions for M_1 and M_2 established by Equation (5.7) or, equivalently, (5.9a)-(5.9c). However, it is critical to highlight that at the specific angle α^*, the tip couple diminishes to zero, yet the stress state remains finite and nonzero. This scenario, as elaborated in Section 2 of the present chapter, corresponds to a wedge loaded by two concentrated dipoles without a resultant moment, located precisely at the tip.

Furthermore, the stress distribution derived from Equations (5.9a)-(5.9c) aligns with eigenfunctions of Airy's stress function of the form $\Psi(r,\theta,\alpha) = \Phi(\theta,\alpha)$, which exhibit a singularity of order $(r)^{-2}$. dependence. As discussed in [90], this three-wedge configuration offers an intuitive and smooth representation of the stress field as a function of the opening angle α, with no anomalous behavior observed at $\alpha = \alpha^*$.

In contrast, Carothers' solution, given by Equations (3.1a)-(3.1c), is problematic at the critical angle since $M = 0$, thereby leading to the well-known wedge paradox. The presented approach effectively resolves this issue by addressing the wedge with a critical angle subjected to a nonzero tip couple.

However, alternative solutions, such as those introduced by Sternberg and Koiter [69], must be considered to accommodate non-quadratic stress singularities. It should also be noted that the uniqueness of the solution and the convergence of the energy integral are not addressed here. For instance, if a truncated wedge bounded by an arc of radius r_0 is considered, various distributed traction systems along the arc could satisfy equilibrium with zero resultant force and a moment different from zero. As $r_0 \to 0$, these configurations may lead to distinct stress states. Our primary aim has been to propose a physically meaningful representation for those stress states associated with eigenfunctions exhibiting quadratic singularities at the wedge tip.

Finally, we observe that the proposed solution relies on an ideal separation of the wedge (Figure 5.1) into three sub-wedges (Figure 5.2), a strategy inspired by the form of Carothers' solution [26], particularly condition (5.1). It is natural to question whether other configurations could exist by altering the orientation of the separation line, defined by the angle β. To explore this, let β represent an arbitrary angle within $0 < \beta < \pi/2$, as illustrated in Figure 5.4a. The revised separation, shown in Figure 5.4b, assumes wedge I has a width of 2β, while wedges II have an opening angle of $\alpha - \beta$. The analysis proceeds with similar arguments to those discussed earlier.

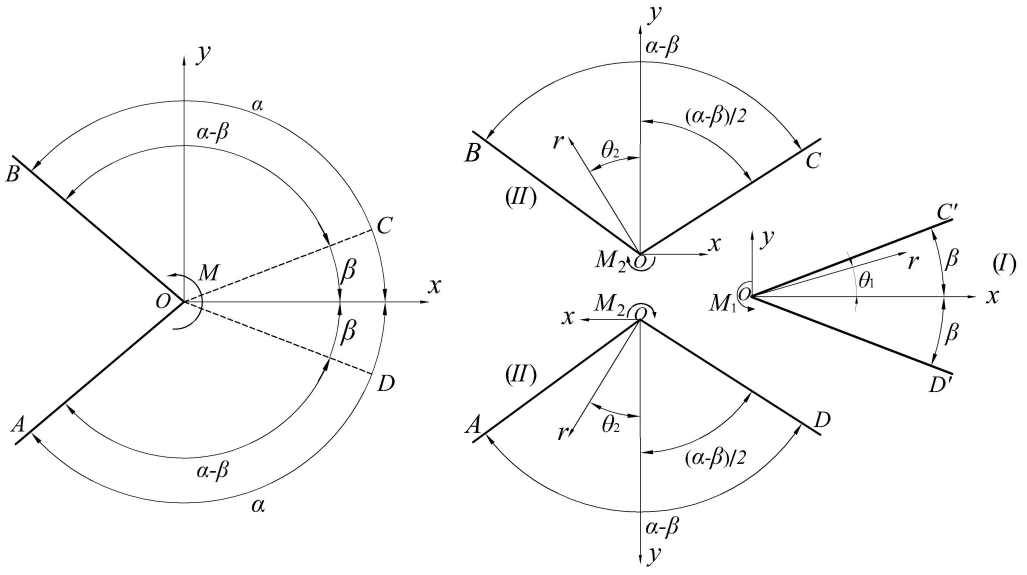

Figure 5.4: Alternative ideal splitting of the wedge of width 2α loaded by a tip couple M. (a) Arbitrary angle $0 < \beta < \pi/2$ for the cutting line. (b) The auxiliary problem where the wedge I of opening angle 2β is loaded by the tip couple M_1 and the two wedges II, of width $\alpha - \beta$ are loaded by M_2.

The stress components in wedge I are still defined by Equations (5.2a)-(5.2c). In wedges II, the stress components are analogous to Equations (5.3a)-(5.3c), with $(\pi - 2\beta)$ replaced by $(\alpha - \beta)$. Continuity of traction along the inclined lines is

inherently satisfied due to the symmetry of the problem. Compatibility conditions for displacements, derived using Cesaro's integral representation for radial lines $\overline{OC}$ and $\overline{OC'}$ (similarly for $\overline{OD}$ and $\overline{OD'}$) approaching the boundaries of the wedges, are met provided:

$$\sigma_{rr}^{(1)}(r,\beta^-) = \sigma_{rr}^{(2)}(r,-(\alpha/2-\beta/2)^+)\,, \tag{5.10a}$$

$$\sigma_{rr,\theta_1}^{(1)}(r,\beta^-) = \sigma_{rr,\theta_2}^{(2)}(r,-(\alpha/2-\beta/2)^+)\,. \tag{5.10b}$$

From these, one respectively obtains

$$\frac{M_1 \sin 2\beta}{\sin 2\beta - 2\beta\cos 2\beta} = -\frac{M_2 \sin(\beta-\alpha)}{\sin(\alpha-\beta)-(\alpha-\beta)\cos(\alpha-\beta)}, \tag{5.11a}$$

$$\frac{M_1 \cos 2\beta}{\sin 2\beta - 2\beta\cos 2\beta} = -\frac{M_2 \cos(\beta-\alpha)}{\sin(\alpha-\beta)-(\alpha-\beta)\cos(\alpha-\beta)}, \tag{5.11b}$$

These equations are satisfied if

$$\cos(2\beta)\,\sin(\beta-\alpha) = \sin 2\beta\,\cos(\beta-\alpha)\,, \quad \Rightarrow \quad \sin(\beta+\alpha) = 0\,. \tag{5.12a}$$

Taking into account that, for the problem at hand, $0 < \beta < \pi/2$ and $\pi/2 < \alpha < \pi$, with $\alpha - \beta < \pi$, this condition yields

$$\beta + \alpha = \pi\,. \tag{5.12b}$$

Consequently, $\beta = \pi - \alpha$, bringing us back to the original three-wedge configuration depicted in Figure 5.2. This result confirms that the only viable splitting of the original wedge problem into three sub-wedges is as shown in Figure 5.2. This outcome reinforces the validity of the proposed generalized solution for a wedge under a tip couple, as provided by Equations (5.2a)-(5.2c), (5.3a)-(5.3c), (5.7), and (5.8), or equivalently, Equations (5.9a)-(5.9c).

5.2 Stress state derived from nuclei of strain

In this section, we introduce an alternative derivation of the generalized solution for the wedge problem, initially proposed in previous section. This method examines potential singularities of varying intensities within linear elastic materials, which are referred to as "nuclei of strain" by Love [10].

For an infinite, isotropic, three-dimensional linear elastic solid, Kelvin's fundamental solution [32] describes the singular displacement field resulting from a point force. Love [10] explored stress states in certain plane strain scenarios where stresses exhibit singularities at specific points, either within cavities, along boundaries, or outside the body. We refer to Love's analysis in [10], Section 152, for examining solutions of plane strain equations that include such singularities.

5.2.1 Stress state due to a single force

Equation (5.13) defines the stress state due to a single force of magnitude $2\pi A$, applied at the origin of an infinite plane elastic body and acting in $-x$ direction. It is expressed in Cartesian coordinates (x, y) by setting $r^2 = x^2 + y^2$.

$$\sigma_{xx} = A\frac{x}{r^2}\left[(\eta+\gamma) - \eta\frac{y^2}{r^2}\right], \tag{5.13a}$$

$$\sigma_{yy} = A\frac{x}{r^2}\left(-\gamma + \eta\frac{y^2}{r^2}\right), \tag{5.13b}$$

$$\sigma_{xy} = A\frac{y}{r^2}\left(\gamma + \eta\frac{x^2}{r^2}\right), \tag{5.13c}$$

with $\eta = 2(\lambda+\mu)/(\lambda+2\mu), \gamma = \mu/(\lambda+2\mu)$, being λ and μ the Lamé's constants.

5.2.2 Stress state due to a double-forces with moment

Figure 5.5 , depicts the concept of nuclei of strain within an infinite elastic plane. Assume that, along with the single force acting at the origin, a counterforce of equal magnitude $2\pi A$ but in the positive direction of x acts at $(0, h)$, as indicated in Figure 5.5. By allowing parameter A to approach infinity and the distance h to shrink to zero, while ensuring the product Ah remains finite, one derives stress state corresponding to a double-force with moment, act along the x-axis as

$$\sigma_{xx} = Ah\frac{\partial}{\partial y}\left\{\frac{x}{r^2}\left[(\eta+\gamma) - \eta\frac{y^2}{r^2}\right]\right\}, \tag{5.14a}$$

$$\sigma_{yy} = Ah\frac{\partial}{\partial y}\left[\frac{x}{r^2}\left(-\gamma + \eta\frac{y^2}{r^2}\right)\right], \tag{5.14b}$$

$$\sigma_{xy} = Ah\frac{\partial}{\partial y}\left[\frac{y}{r^2}\left(\gamma + \eta\frac{x^2}{r^2}\right)\right], \tag{5.14c}$$

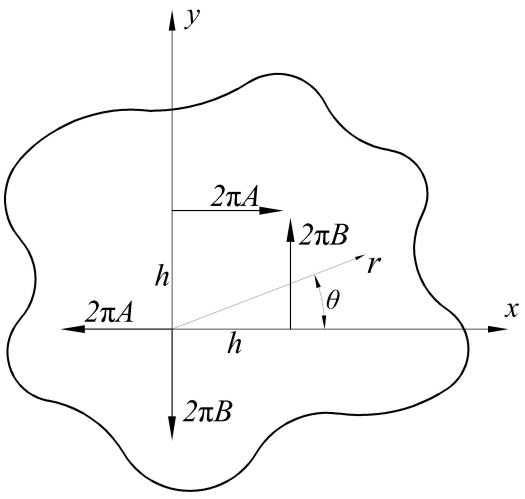

Figure 5.5: Nuclei of strain in an infinite plane body. In the limit $(A, B) \to +\infty$ and $h \to 0$ while Ah and Bh remain constant and finite, one obtains two double forces with moment, respectively acting in the direction of the x and the y axis.

5.2.3 Stress state due to two double forces with moment

Consider now another nuclei of strain, derived from double forces of magnitude $2\pi B$ acting in the direction of the y axis, also represented in Figure 5.5. The stress state for the fundamental problem of the force acting at the origin, can be obtained from earlier solution by substituting B for A and interchanging x and y. Taking again the limit for $B \to +\infty, h \to 0$ such that Bh remains finite, one obtains

$$\sigma_{xx} = Bh\frac{\partial}{\partial x}\left[\frac{y}{r^2}\left(-\gamma + \eta\frac{x^2}{r^2}\right)\right], \tag{5.15a}$$

$$\sigma_{yy} = Bh\frac{\partial}{\partial x}\left\{\frac{y}{r^2}\left[(\eta+\gamma) - \eta\frac{x^2}{r^2}\right]\right\}, \tag{5.15b}$$

$$\sigma_{xy} = Bh\frac{\partial}{\partial x}\left[\frac{x}{r^2}\left(\gamma + \eta\frac{y^2}{r^2}\right)\right]. \tag{5.15c}$$

Let us define $T_A := 2\pi Ah$ and $T_B =: 2\pi Bh$. By superimposing the stress states described by Equations (5.14a)-(5.14c) and (5.15a)-(5.15c), we obtain:

$$\sigma_{xx} = \frac{xy}{\pi r^4}\left\{T_A\left[-(2\eta+\gamma) + 2\eta\frac{y^2}{r^2}\right] + T_B\left[(\eta+\gamma) - 2\eta\frac{x^2}{r^2}\right]\right\}, \tag{5.16a}$$

$$\sigma_{yy} = \frac{xy}{\pi r^4}\left\{T_A\left[(\eta+\gamma) - 2\eta\frac{y^2}{r^2}\right] + T_B\left[-(2\eta+\gamma) + 2\eta\frac{x^2}{r^2}\right]\right\}, \tag{5.16b}$$

$$\begin{aligned}\sigma_{xy} = \frac{1}{2\pi r^2}\Bigg\{&T_A\left[\gamma\left(1-2\frac{y^2}{r^2}\right) + \eta\frac{x^2}{r^2}\left(1-4\frac{y^2}{r^2}\right)\right] \\ &+ T_B\left[\gamma\left(1-2\frac{x^2}{r^2}\right) + \eta\frac{y^2}{r^2}\left(1-4\frac{x^2}{r^2}\right)\right]\Bigg\}.\end{aligned} \tag{5.16c}$$

This state of stress corresponds to the limit of the full load condition represented in Figure 5.5, and characterized in [10] as two double forces with moment.
The state of stress given by (5.16a)-(5.16c) can be expressed in the polar coordinate system indicated in Figure 5.5, in the form

$$\sigma_{rr}(r,\theta) = -\frac{\eta\,(T_A+T_B)}{2\pi r^2}\sin 2\theta, \tag{5.17a}$$

$$\sigma_{\theta\theta}(r,\theta) = 0\,, \tag{5.17b}$$

$$\sigma_{r\theta}(r,\theta) = \frac{\eta\,(T_A+T_B)}{4\pi r^2}\left[\cos 2\theta + \frac{2(T_A-T_B)}{\eta\,(T_A+T_B)}\right]. \tag{5.17c}$$

Equations (5.17a)-(5.17c) describe the stress state in the infinite plane. The solution can be tailored to describe the stress state in an elastic wedge with an angular width 2α, with $\pi/2 < \alpha < \pi$. To achieve this, and based on the conditions illustrated in Figure 5.1 and Equation (5.1), T_A and T_B must be chosen so satisfy the following relationships:

$$\sigma_{r\theta}\,(r,\pm\alpha) = 0 \;\;,\;\; \sigma_{r\theta}\,(r,\pm(\pi-\alpha)) = 0\,. \tag{5.18}$$

From (5.17c), one finds that this requirement is satisfied provided that

$$\cos 2\alpha = -\frac{2(T_A - T_B)}{\eta(T_A + T_B)}\,. \tag{5.19}$$

In this case, one can rewrite the stress state of (5.17a)-(5.17c) as

$$\sigma_{rr} = -\frac{\eta\,(T_A + T_B)}{2\pi r^2}\sin 2\theta, \tag{5.20a}$$

$$\sigma_{\theta\theta} = 0, \tag{5.20b}$$

$$\sigma_{r\theta} = \frac{\eta\,(T_A + T_B)}{4\pi r^2}\left(\cos 2\theta - \cos 2\alpha\right)\,. \tag{5.20c}$$

The stress state described by Equations (5.20a)-(5.20c) is consistently achieved for an elastic wedge with a width of 2α, where $\pi < 2\alpha < 2\pi$, and with traction-free boundaries. The concentrated forces act solely at the vertex of the wedge. This state exhibits the same singularity order as Carothers' solution, Equations (3.1a)-(3.1c), and the two formulations align perfectly under the condition:

$$\frac{\eta(T_A + T_B)}{4\pi} = -\frac{M}{\sin 2\alpha - 2\alpha\cos 2\alpha}\,. \tag{5.21}$$

However, a key distinction exists: the form represented by Equation (5.21) remains valid for any opening angle α, ensuring consistency across the range of interest.

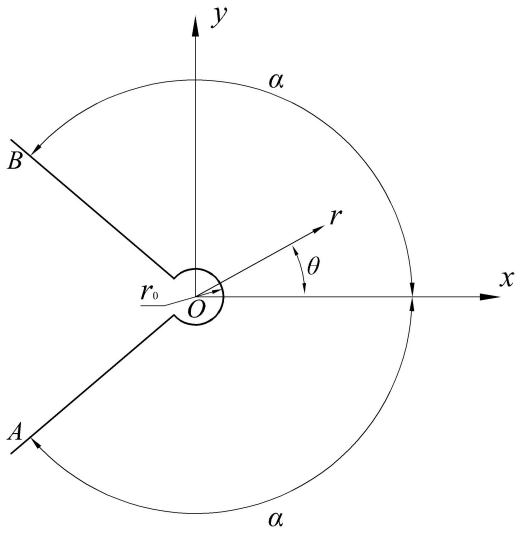

Figure 5.6: The wedge of width 2α, from which a circular cavity of radius r_0, concentric with respect to the center, has been cut.

Furthermore, the stress representation outlined in Equations (5.9a)-(5.9c), derived in Section 1 of the present chapter, for the three-wedge problem, can also be deduced from Equations (5.20a)-(5.20c), by appropriately setting the following conditions for $\pi/2 < \alpha < \pi$,

$$-\frac{\eta\,(T_A+T_B)}{2\pi}=\frac{2M_1}{-\sin 2\alpha+2(\alpha-\pi)\cos 2\alpha}\,, \tag{5.22}$$

To analyze the forces acting at the tip, as described in [10], consider the geometry depicted in Figure 5.6. This figure shows an elastic wedge with a width of 2α, where a small circular cavity of radius r_0 is removed near the vertex. It can be easily verified that the net force resulting from the surface stresses along the cavity boundary equals zero. The moment M caused by these surface stresses about the origin is given by the relation:

$$\begin{aligned} M=-\int_{-\alpha}^{+\alpha}\sigma_{r\theta}\,(r_0,\theta)\,r_0^2 d\theta &= -\frac{\eta}{4\pi}\,(T_A+T_B)\int_{-\alpha}^{+\alpha}(\cos 2\theta-\cos 2\alpha)d\theta \\ &= -\frac{\eta}{4\pi}\,(T_A+T_B)\,(\sin 2\alpha-2\alpha\cos 2\alpha)\,. \end{aligned} \tag{5.23}$$

It is important to note that only when $\sin 2\alpha - 2\alpha\cos 2\alpha \neq 0$, the term $T_A + T_B$ can be expressed as a function of M and substituted into Equations (5.20a)-(5.20c) to recover Carothers' solution (3.1a)-(3.1c). When $\sin 2\alpha - 2\alpha\cos 2\alpha = 0$, this substitution is not possible.

In general, $T_A + T_B$ can assume any value, independent of α, as these quantities represent the moments of the dipoles applied to the infinite plane used to derive the elastic solution for the wedge problem. Therefore, the stress state defined by Equations (5.20a)-(5.20c) corresponds to the stresses in an elastic wedge subjected to dipoles applied at the vertex. These dipoles produce no net force, while the moment M is determined by Equation (5.23).
At $\alpha = \alpha^*$, it is found that $M = 0$. Thus, at the critical angle, Equations (5.20a)-(5.20c) describe the stress state in the wedge resulting from dipoles without a resultant moment. Carothers' formulation conceals this potential static condition because it requires $T_A + T_B$ to be expressed as a function of M via Equation (5.23).

5.3 Conclusions

This chapter introduced a generalized framework for representing the stress state in a linear elastic wedge with stress-free boundaries, characterized by a singularity of order $(r)^{-2}$. The applied forces are localized exclusively at the vertex and are generally equivalent to a tip couple with moment M. The new solution is intuitively constructed by analysing an auxiliary problem where the wedge is divided into three sub-wedges subjected to tip couples. The relative magnitudes of these couples are determined through compatibility conditions involving stress and displacement. This approach accommodates scenarios where the net moment M equals zero, even though a non-zero stress field persists within the material. Unlike the classical solution proposed by Carothers, which exhibits spurious behavior at the critical wedge angle by predicting unbounded stress throughout the domain, the presented solution remains valid for any wedge angle. Interestingly, as the wedge angle approaches the critical value, the resultant moment M vanishes. The proposed formulation, derived intuitively through the concept of nuclei of strain, implies that at the critical angle, the forces act as moment-free dipoles concentrated at the vertex.

This study does not aim to resolve the problem of a wedge subjected to a nonzero concentrated tip couple at the critical opening angle. As several researchers have observed, it appears that a solution involving an eigenfunction with a stress singularity of order $(r)^{-2}$ is unattainable in such cases. Alternative solutions, potentially involving different singularity strengths, would need to be explored, but this lies beyond the scope of the current work. In the classical sense, as described by Quine [149], a paradox arises when a seemingly valid argument leads to a conclusion that appears implausible or contradictory. Carothers' formulation is effective in many cases but breaks down in a specific scenario, leading to absurd results. Does this flaw undermine the integrity of the classical solution to this longstanding elasticity problem? Our findings suggest that the issue lies in the problem's formulation rather than its solution. Instead of framing the problem as "a linear elastic wedge subjected to a concentrated couple at its vertex," we propose reformulating it as "a linear elastic wedge subjected to dipoles at its vertex." This reinterpretation naturally resolves the paradox.

Chapter 6

Analytical Solution to The Second Problem

6.1 Problem statement in terms of distributed dislocations

The stress state in a linear elastic body experiencing a specified temperature variation can be determined by superimposing the effects of "dilatation centers." These centers act as strain nuclei, simulating the thermal expansion of the material as if it were composed of infinitesimal spherical inclusions undergoing uniform expansion [150]. For the sake of completeness, this classical method is revisited in the Appendix B. However, this section introduces an alternative approach based on the distributed dislocation method. Distributed dislocations, briefly studied in Section 2.5 of Chapter 2, are a widely used tool for representing the stress states of elastic bodies containing cracks and inclusions. In the present context, they are employed to counterbalance the thermal mismatch between distinct regions of the body.

Consider the problem illustrated in Figure 3.2 of Chapter 3. Suppose that cuts are made along the straight boundaries separating regions I and II. A temperature variation is then applied to the isolated wedge (region I). Assuming the material is thermally homogeneous and isotropic, the resulting deformation is homothetic and devoid of stress, implying that the wedge's opening angle, 2β, remains unchanged. If the position of the center O is held fixed, the thermal expansion induces a relative displacement between the wedge and the adjacent portions of the plate on either side of the cut. This displacement is depicted schematically in Figure 6.1.

This approach provides a robust framework for analyzing the interaction between thermally induced strain and the elastic constraints of the surrounding material. By utilizing distributed dislocations, the thermal mismatch is effectively modeled, offering insights into the stress redistribution mechanisms within the body.

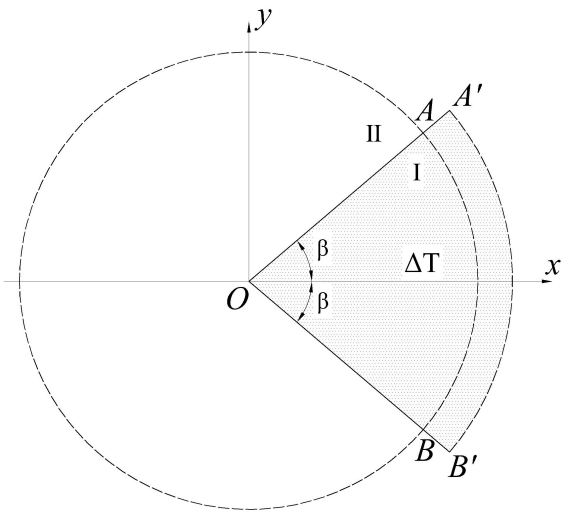

Figure 6.1: thermal expansion of the heated wedge portion after cuts have been made along the radii that delimit the sector.

Let A and B represent the positions of two material particles lying on the radii that define sector I, equidistant from the center O. Following the cutting of the plate, thermal expansion affects the material such that the portion in region II retains its original positions A and B. In contrast, the portion in region I undergoes radial displacement, shifting outward to new positions A' and B'. This displacement is quantified as $\alpha\Delta\mathrm{T}r$, in the outward direction, where α is the thermal expansion coefficient of the material, $\Delta\mathrm{T}$ is the temperature change, and r represents the radial distance from the center. To restore continuity between regions I and II, the displaced points A' and B' must be forced back to coincide with their original counterparts A and B, as depicted schematically in Figure 6.2a.

The reconciliation of regions I and II is achieved through a two-step process. First, the regions are welded back together, ensuring physical continuity. Second, arrays of dislocations are introduced to accommodate the misfit caused by thermal expansion. The creation of a dislocation involves a series of steps [151]. Initially, the material is cleaved along a specified trajectory extending from the dislocation core to the boundary (or to infinity in the case of an infinite solid). Next, a relative displacement, referred to as the Burgers vector component (Section 2.5) or the dislocation strength, is imposed between adjacent points on either side of the cleaved surface. Finally, the material is welded back together [152].

This process ensures that the thermal mismatch and its resulting stress redistribution are systematically addressed, enabling an accurate representation of the elastic body's response to temperature variations. The use of distributed dislocations allows for precise control over the localized deformation and stress fields, making this approach particularly effective for complex thermal-structural problems.

The resulting stress state corresponds to that in an infinite elastic plate where two arrays of dislocations are distributed along the interface radii separating regions I and II. These dislocations are arranged to generate a relative radial displacement that counteracts the thermal mismatch induced by expansion. This targeted adjustment restores compatibility between the adjoining regions, ensuring a balanced stress distribution within the elastic plate. The required type of dislocation to effectively neutralize the thermal strain, by introducing localized deformation along the

interface, is a glide dislocation [153], characterized by a Burgers vector, b, oriented radially. This configuration is schematically illustrated in Figure 6.2b. Bergers vector and glide dislocation previously reviewed in Section 2.5 of Chapter 2.

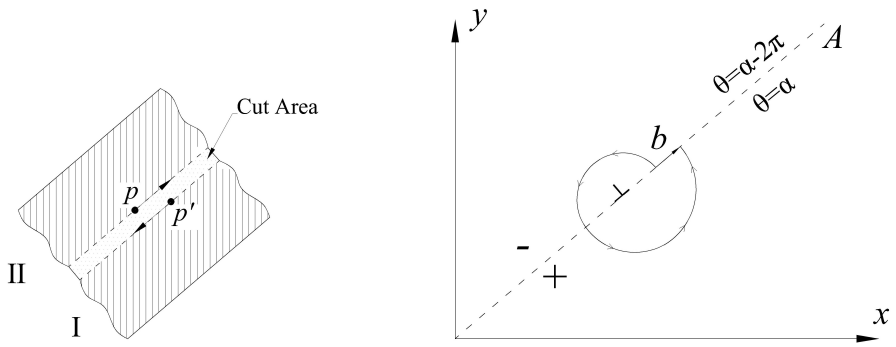

Figure 6.2: System of dislocation required to annihilate the thermal mismatch. (a) Required relative displacement between points A and A'; (b) Burgers vector for a glide dislocation on the interface radius.

Solutions addressing various types of point singularities, including poles, dipoles, and dislocations, are extensively documented in the literature [10, 55, 154]. In the context of a polar coordinate system $(\bar{r}, \bar{\theta})$, let us examine the case of a glide dislocation in an infinite elastic body. This dislocation introduces a discontinuity in the radial displacement, $u_{\bar{r}}$, such that $u_{\bar{r}}(\bar{r}, 2\pi) - u_{\bar{r}}(\bar{r}, 0) = db_0$. Here, db_0 represents the radial component of the Burgers vector associated with the dislocation. This discontinuity effectively models the strain resulting from the glide dislocation, capturing the localized deformation in the material.

To describe the stress state induced by such a dislocation, the Airy stress function is employed. For this specific scenario, the stress function can be expressed, detailed in reference [155], as

$$d\phi = -\frac{2\mu\, db_0}{\pi(\kappa+1)}\, \bar{r} \log \bar{r} \sin\bar{\theta}\,, \tag{6.1}$$

Where, μ is the shear elastic modulus and κ is Kolosov's constant. In this approach, arrays of glide dislocations are distributed along the interface radii, as depicted in Figure 6.3. A polar coordinate system (r, θ), centered at O, is introduced to describe the geometry of the problem, as shown in the figure. Consider a uniformly distributed array of glide dislocations along the radii, where the Burgers vector per unit length remains constant and is equal to $\alpha\Delta T$. This configuration generates a relative displacement along the interface that varies linearly with the distance from the center. This displacement effectively counteracts and neutralizes the thermal mismatch between the adjoining regions.

Specifically, the cumulative effect of radial glide dislocations is evaluated as follows:

- On the upper radius OA, located at $(r, \theta) = (r_0, \beta)$, the Burgers vector is given by; $db_{r_0^+} = -\alpha\Delta T dr_0$.

- On the lower radius OB, situated at $(r, \theta) = (r_0, -\beta)$, the Burgers vector is equal to; $db_{r_0^-} = +\alpha \Delta T dr_0$

Summing these contributions results in a net displacement at the interface, which restores compatibility by eliminating the thermally induced strain mismatch. This technique leverages the properties of glide dislocations to achieve a controlled adjustment of the relative positions of the regions, ensuring a stress-free interface. So, one can obtain the following total displacements;

$$\begin{aligned} u_r(r, \beta + 2\pi) - u_r(r, \beta) &= \int_0^r -\alpha \Delta T dr_0 = -\alpha \Delta T r \,, \\ u_r(r, -\beta + 2\pi) - u_r(r, -\beta) &= \int_0^r \alpha \Delta T dr_0 = \alpha \Delta T r \,. \end{aligned} \tag{6.2}$$

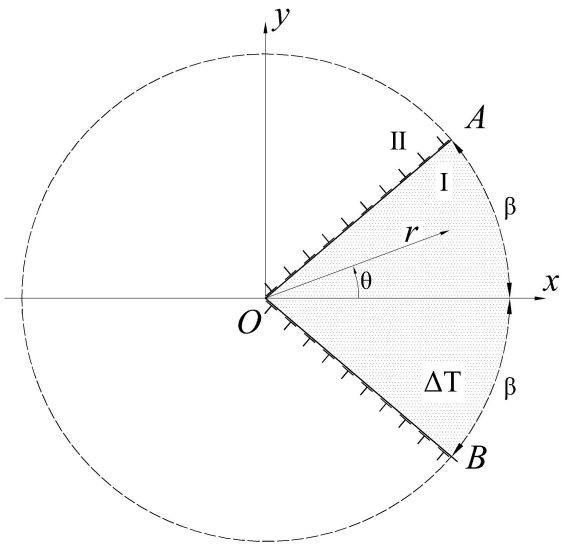

Figure 6.3: Distributed array of dislocations along the interface radii and general polar system (r, θ) of coordinates.

In order to determine the Airy stress function, one can use the expression (6.1). The correspondences between the global polar coordinate system (r, θ) and the local systems $(\bar{r}, \bar{\theta})$ for radial glide dislocations applied at point D distant r_0 from the center, either on the upper radius OA or the lower radius OB, are respectively shown in Figures 6.4a and 6.4b. Let

$$A = -\frac{2\mu}{\pi(\kappa + 1)} \alpha \Delta T \,, \tag{6.3}$$

denote the dislocation density. For the radius OA, since $\bar{r}^2 = r^2 + r_0^2 - 2 r r_0 \cos\theta_1$ and $\bar{r} \sin\bar{\theta} = r \sin\theta_1$, with $\theta_1 = \theta - \beta$, from Equation (6.1), one obtains

$$d\phi^+ = -\frac{1}{2} A dr_0 \, r \sin(\theta - \beta) \log[r^2 + r_0^2 - 2 r r_0 \cos(\theta - \beta)] \,. \tag{6.4}$$

On the radius OB one has $\bar{r}^2 = r^2 + r_0^2 - 2rr_0\cos\theta_2$ and $\bar{r}\sin\bar{\theta} = r\sin\theta_2$, with $\theta_2 = \theta + \beta$. Hence

$$d\phi^- = \frac{1}{2}Adr_0\, r\sin(\theta+\beta)\log[r^2 + r_0^2 - 2rr_0\cos(\theta+\beta)]\,. \tag{6.5}$$

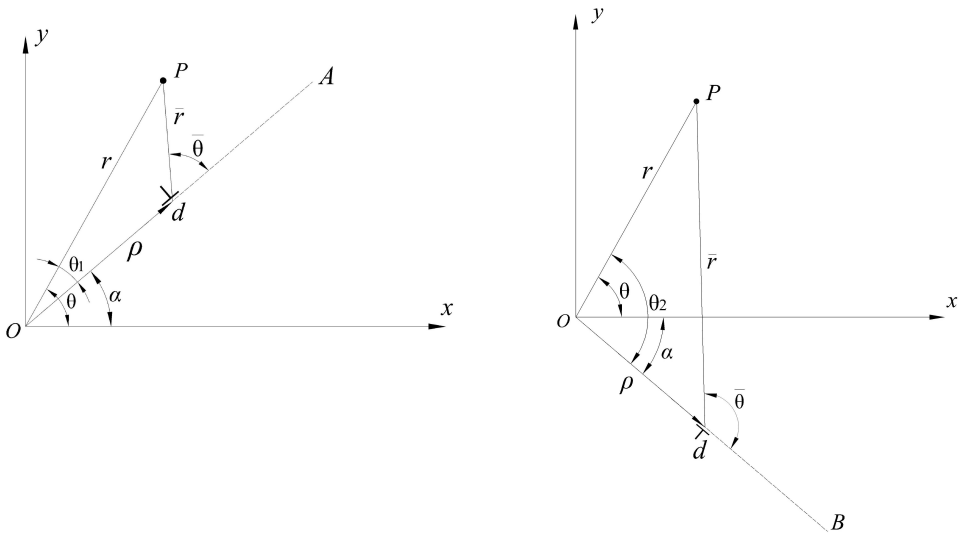

(a) (b)

Figure 6.4: Reference coordinate system for a single dislocation applied at (a) the upper interface radius at $(r,\theta) = (r_0,\beta)$ and (b) at the lower interface radius at $(r,\theta) = (r_0,-\beta)$.

Considering the linear nature of the elasticity equations, the contributions of the dislocations along the radii OA and OB can be summed symmetrically at the same radial distance r_0 from the center. This yields the total differential stress function as: $d\phi = d\phi^+ + d\phi^-$.

Here, $d\phi^+$and $d\phi^-$represent the stress function contributions from the dislocations on the upper radius OA and the lower radius OB, respectively. To determine the overall stress function resulting from the aggregation of these dislocations distributed along the segments $\overline{OA}$ and $\overline{OB}$, spanning the radial range between $r_0 = R_-$and $r_0 = R_+$, integration is performed over the radial coordinate. It leads to

$$\begin{aligned}\phi = \int_{r_0=R_-}^{r_0=R_+} d\phi^+ + d\phi^- = -\frac{A}{2}r\int_{R_-}^{R_+}\Big\{&\sin(\theta_1)\log\left[r^2 + r_0^2 - 2rr_0\cos(\theta_1)\right] \\ &- \sin(\theta_2)\log\left[r^2 + r_0^2 - 2rr_0\cos(\theta_2)\right]\Big\}dr_0\,.\end{aligned} \tag{6.6}$$

Performing the integration, one finds

$$
\begin{aligned}
\phi = A\Big\{ & \frac{r}{2}\Big\{ \Big(\frac{r}{2}\sin(2\theta_1) - R_+\sin(\theta_1)\Big)\log\left[r^2 + {R_+}^2 - 2R_+ r\cos(\theta_1)\right] \\
& \quad - \Big(\frac{r}{2}\sin(2\theta_2) - R_+\sin(\theta_2)\Big)\log\left[r^2 + {R_+}^2 - 2R_+ r\cos(\theta_2)\right] \Big\} \\
& -r^2\Big\{ \sin^2(\theta_1)\tan^{-1}\left[\frac{R_+}{r\sin(\theta_1)} - \cot(\theta_1)\right] \\
& \quad - \sin^2(\theta_2)\tan^{-1}\left[\frac{R_+}{r\sin(\theta_2)} - \cot(\theta_2)\right] \Big\} \\
& -\frac{r}{2}\Big\{ \Big(\frac{r}{2}\sin(2\theta_1) - R_-\sin(\theta_1)\Big)\log\left[r^2 + {R_-}^2 - 2R_- r\cos(\theta_1)\right] \\
& \quad - \Big(\frac{r}{2}\sin(2\theta_2) - R_-\sin(\theta_2)\Big)\log\left[r^2 + {R_-}^2 - 2R_- r\cos(\theta_2)\right] \Big\} \\
& +r^2\Big\{ \sin^2(\theta_1)\tan^{-1}\left[\frac{R_-}{r\sin(\theta_1)} - \cot(\theta_1)\right] \\
& \quad - \sin^2(\theta_2)\tan^{-1}\left[\frac{R_-}{r\sin(\theta_2)} - \cot(\theta_2)\right] \Big\} \\
& \quad + r\left(\sin\theta_1 - \sin\theta_2\right)\left(R_+ - R_-\right)\Big\}.
\end{aligned}
\tag{6.7}
$$

Hence, from Equations (3.2a)-(3.2c), one obtains the state of stress

$$
\begin{aligned}
\sigma_{rr}/A = & -\frac{1}{2}\Big\{ \sin(2\theta_1)\log\left[r^2 + {R_+}^2 - 2rR_+\cos(\theta_1)\right] \\
& \quad - \sin(2\theta_2)\log\left[r^2 + {R_+}^2 - 2rR_+\cos(\theta_2)\right] \Big\} \\
& -\frac{r^2}{2}\Big\{ \frac{\sin(2\theta_1)}{r^2 + {R_+}^2 - 2rR_+\cos(\theta_1)} - \frac{\sin(2\theta_2)}{r^2 + {R_+}^2 - 2rR_+\cos(\theta_2)} \Big\} \\
& +rR_+\Big\{ \frac{\sin(\theta_1)\cos(2\theta_1)}{r^2 + {R_+}^2 - 2rR_+\cos(\theta_1)} - \frac{\sin(\theta_2)\cos(2\theta_2)}{r^2 + {R_+}^2 - 2rR_+\cos(\theta_2)} \Big\} \\
& -2\Big\{ \cos^2(\theta_1)\tan^{-1}\left[\frac{R_+}{r\sin(\theta_1)} - \cot(\theta_1)\right] \\
& \quad - \cos^2(\theta_2)\tan^{-1}\left[\frac{R_+}{r\sin(\theta_2)} - \cot(\theta_2)\right] \Big\} \\
& +\frac{1}{2}\Big\{ \sin(2\theta_1)\log\left[r^2 + {R_-}^2 - 2rR_-\cos(\theta_1)\right] \\
& \quad - \sin(2\theta_2)\log(r^2 + {R_-}^2 - 2rR_-\cos(\theta_2)) \Big\} \\
& +\frac{r^2}{2}\Big\{ \frac{\sin(2\theta_1)}{r^2 + {R_-}^2 - 2rR_-\cos(\theta_1)} - \frac{\sin(2\theta_2)}{r^2 + {R_-}^2 - 2rR_-\cos(\theta_2)} \Big\} \\
& -rR_-\Big\{ \frac{\sin(\theta_1)\cos(2\theta_1)}{r^2 + {R_-}^2 - 2rR_-\cos(\theta_1)} - \frac{\sin(\theta_2)\cos(2\theta_2)}{r^2 + {R_-}^2 - 2rR_-\cos(\theta_2)} \Big\} \\
& +2\Big\{ \cos^2(\theta_1)\tan^{-1}\left[\frac{R_-}{r\sin(\theta_1)} - \cot(\theta_1)\right] \\
& \quad - \cos^2(\theta_2)\tan^{-1}\left[\frac{R_-}{r\sin(\theta_2)} - \cot(\theta_2)\right] \Big\},
\end{aligned}
\tag{6.8a}
$$

$$
\begin{aligned}
\sigma_{\theta\theta}/A = \frac{1}{2}\Big\{ & \sin(2\theta_1)\log\left[r^2 + {R_+}^2 - 2rR_+\cos(\theta_1)\right] \\
& - \sin(2\theta_2)\log\left[r^2 + {R_+}^2 - 2rR_+\cos(\theta_2)\right] \Big\} \\
& + \frac{r^2}{2}\Big\{ \frac{\sin(2\theta_1)}{r^2 + {R_+}^2 - 2rR_+\cos(\theta_1)} - \frac{\sin(2\theta_2)}{r^2 + {R_+}^2 - 2rR_+\cos(\theta_2)} \Big\} \\
& - (rR_+)\Big\{ \frac{\sin(\theta_1)\cos(2\theta_1)}{r^2 + {R_+}^2 - 2rR_+\cos(\theta_1)} - \frac{\sin(\theta_2)\cos(2\theta_2)}{r^2 + {R_+}^2 - 2rR_+\cos(\theta_2)} \Big\} \\
& - 2\Big\{ \sin^2(\theta_1)\tan^{-1}\left[\frac{R_+}{r\sin(\theta_1)} - \cot(\theta_1)\right] \\
& - \sin^2(\theta_2)\tan^{-1}\left[\frac{R_+}{r\sin(\theta_2)} - \cot(\theta_2)\right] \Big\} \\
& - \frac{1}{2}\Big\{ \sin(2\theta_1)\log\left[r^2 + {R_-}^2 - 2rR_-\cos(\theta_1)\right] \\
& - \sin(2\theta_2)\log(r^2 + {R_-}^2 - 2rR_-\cos(\theta_2)) \Big\} \\
& - \frac{r^2}{2}\Big\{ \frac{\sin(2\theta_1)}{r^2 + {R_-}^2 - 2rR_-\cos(\theta_1)} - \frac{\sin(2\theta_2)}{r^2 + {R_-}^2 - 2rR_-\cos(\theta_2)} \Big\} \\
& + (rR_-)\Big\{ \frac{\sin(\theta_1)\cos(2\theta_1)}{r^2 + {R_-}^2 - 2rR_-\cos(\theta_1)} - \frac{\sin(\theta_2)\cos(2\theta_2)}{r^2 + {R_-}^2 - 2rR_-\cos(\theta_2)} \Big\} \\
& + 2\Big\{ \sin^2(\theta_1)\tan^{-1}\left[\frac{R_-}{r\sin(\theta_1)} - \cot(\theta_1)\right] \\
& - \sin^2(\theta_2)\tan^{-1}\left[\frac{R_-}{r\sin(\theta_2)} - \cot(\theta_2)\right] \Big\},
\end{aligned}
\tag{6.8b}
$$

$$
\begin{aligned}
\sigma_{r\theta}/A = -\frac{1}{2}\Big\{ & \cos(2\theta_1)\log\left[r^2 + {R_+}^2 - 2rR_+\cos(\theta_1)\right] \\
& - \cos(2\theta_2)\log\left[r^2 + {R_+}^2 - 2rR_+\cos(\theta_2)\right] \Big\} \\
& - (R_+)^2\Big\{ \frac{\sin^2(\theta_1)}{r^2 + {R_+}^2 - 2rR_+\cos(\theta_1)} - \frac{\sin^2(\theta_2)}{r^2 + {R_+}^2 - 2rR_+\cos(\theta_2)} \Big\} \\
& + \Big\{ \sin(2\theta_1)\tan^{-1}\left[\frac{R_+}{r\sin(\theta_1)} - \cot(\theta_1)\right] \\
& - \sin(2\theta_2)\tan^{-1}\left[\frac{R_+}{r\sin(\theta_2)} - \cot(\theta_2)\right] \Big\} \\
& + \frac{1}{2}\Big\{ \cos(2\theta_1)\log\left[r^2 + {R_-}^2 - 2rR_-\cos(\theta_1)\right] \\
& - \cos(2\theta_2)\log\left[r^2 + {R_-}^2 - 2rR_-\cos(\theta_2)\right] \Big\} \\
& + (R_-)^2\Big\{ \frac{\sin^2(\theta_1)}{r^2 + {R_-}^2 - 2rR_-\cos(\theta_1)} - \frac{\sin^2(\theta_2)}{r^2 + {R_-}^2 - 2rR_-\cos(\theta_2)} \Big\} \\
& - \Big\{ \sin(2\theta_1)\tan^{-1}\left[\frac{R_-}{r\sin(\theta_1)} - \cot(\theta_1)\right] \\
& - \sin(2\theta_2)\tan^{-1}\left[\frac{R_-}{r\sin(\theta_2)} - \cot(\theta_2)\right] \Big\}.
\end{aligned}
\tag{6.8c}
$$

The expressions above entail the bounds $R_+$and R_-, which define the length of the

dislocation arrays.

6.2 Discussion of the solution based on distributed dislocations

To find the solution of the problem, it is necessary to calculate the limits of the expressions (6.8a)-(6.8c) as $R_- \to 0$ and $R_+ \to \infty$. For $R_- \to 0$, recalling that $\theta_1 = \theta - \beta$ and $\theta_2 = \theta + \beta$, one finds

$$\begin{aligned}\lim_{R_-\to 0} \sigma_{rr}/A = &-\sin(2\beta)\cos(2\theta)\left[1+\log(r/R_+)^2\right] \\ &-2\cos^2(\theta-\beta)\Big\{\tan^{-1}\left[\frac{R_+}{r\sin(\theta-\beta)}\right]+\tan^{-1}\left[\cot(\theta-\beta)\right]\Big\} \\ &+2\cos^2(\theta+\beta)\Big\{\tan^{-1}\left[\frac{R_+}{r\sin(\theta+\beta)}\right]+\tan^{-1}\left[\cot(\theta+\beta)\right]\Big\},\end{aligned} \tag{6.9a}$$

$$\begin{aligned}\lim_{R_-\to 0} \sigma_{\theta\theta}/A = &\sin(2\beta)\cos(2\theta)\left[1+\log(r/R_+)^2\right] \\ &-2\sin^2(\theta-\beta)\Big\{\tan^{-1}\left[\frac{R_+}{r\sin(\theta-\beta)}\right]+\tan^{-1}\left[\cot(\theta-\beta)\right]\Big\} \\ &+2\sin^2(\theta+\beta)\Big\{\tan^{-1}\left[\frac{R_+}{r\sin(\theta+\beta)}\right]+\tan^{-1}\left[\cot(\theta+\beta)\right]\Big\},\end{aligned} \tag{6.9b}$$

$$\begin{aligned}\lim_{R_-\to 0} \sigma_{r\theta}/A = &\sin(2\beta)\sin(2\theta)\left[1+\log(r/R_+)^2\right] \\ &+\sin 2(\theta-\beta)\Big\{\tan^{-1}\left[\frac{R_+}{r\sin(\theta-\beta)}\right]+\tan^{-1}\left[\cot(\theta-\beta)\right]\Big\} \\ &-\sin 2(\theta+\beta)\Big\{\tan^{-1}\left[\frac{R_+}{r\sin(\theta+\beta)}\right]+\tan^{-1}\left[\cot(\theta+\beta)\right]\Big\}.\end{aligned} \tag{6.9c}$$

Now it is obvious that, as the array of dislocations extends infinitely ($R_+ \to \infty$), the stress state throughout the entire body grows without bounds. This outcome is consistent with the dimensional analysis presented in Section 4.3 of Chapter 4, where it was noted that the absence of an intrinsic length scale in the infinite body problem inherently leads to such behavior.

- Remark 1. A noteworthy special case arises when the condition $\beta = \pi/2$ is satisfied. Under this scenario, the expressions (6.9a)-(6.9c) yield a finite solution even as $R_+ \to \infty$,. This corresponds to the situation of an infinite elastic plate with a heated half-plane. In this particular case, the stress state remains well-defined because there is no conflicting intersection of dislocation arrays at the center of the disk.

The solution for this case has been directly derived by considering dislocations distributed along a single line at the interface separating the heated and unheated regions. When analyzing a finite array of dislocations limited to the segment defined by ($\theta = \pm\pi/2, 0 \le r \le R_+$), the resulting stress state can be explicitly computed.

This setup represents a simplified yet physically meaningful configuration where the thermal mismatch is effectively modeled through a single line of dislocations. Hence, one can obtain

$$\sigma_{rr}/A = 4\sin^2(\theta)\tan^{-1}\left(\frac{R_+}{r\cos(\theta)}\right), \tag{6.10a}$$

$$\sigma_{\theta\theta}/A = 4\cos^2(\theta)\tan^{-1}\left(\frac{R_+}{r\cos(\theta)}\right), \tag{6.10b}$$

$$\sigma_{r\theta}/A = 2\sin(2\theta)\tan^{-1}\left(\frac{R_+}{r\cos(\theta)}\right). \tag{6.10c}$$

These expressions coincide with the limit of Equations (6.9a)-(6.9c) as $\beta \to \pi/2$. Now, as $R_+ \to +\infty$, the function $\tan^{-1}\left(\frac{R_+}{r\cos(\theta)}\right)$ tends to $+\pi/2$ or $-\pi/2$ according to the sign of $\cos(\theta)$. The state of stress is not defined right at the interfaces $\theta = \pi/2$, and $\theta = -\pi/2$. Therefore, one obtains

$$\lim_{R_+\to+\infty} \sigma_{rr}/A = \begin{cases} 2\pi\sin^2(\theta), & \text{if } -\pi/2 < \theta < \pi/2\,, \\ -2\pi\sin^2(\theta), & \text{if } \pi/2 < \theta < 3\pi/2\,, \end{cases} \tag{6.11a}$$

$$\lim_{R_+\to+\infty} \sigma_{\theta\theta}/A = \begin{cases} 2\pi\cos^2(\theta), & \text{if } -\pi/2 < \theta < \pi/2\,, \\ -2\pi\cos^2(\theta), & \text{if } \pi/2 < \theta < 3\pi/2\,, \end{cases} \tag{6.11b}$$

$$\lim_{R_+\to+\infty} \sigma_{r\theta}/A = \begin{cases} \pi\sin(2\theta), & \text{if } -\pi/2 < \theta < \pi/2\,, \\ -\pi\sin(2\theta), & \text{if } \pi/2 < \theta < 3\pi/2\,. \end{cases} \tag{6.11c}$$

In the Cartesian reference frame (x, y) of Figure 6.3, recalling (6.3), this corresponds to the state of stress

$$\sigma_{xx} = \sigma_{xy} = 0\,, \quad \sigma_{yy} = \begin{cases} -\dfrac{4\mu}{\kappa+1}\,\alpha\Delta T, & \text{if } -\pi/2 < \theta < \pi/2\,, \\ \dfrac{4\mu}{\kappa+1}\,\alpha\Delta T, & \text{if } \pi/2 < \theta < 3\pi/2\,. \end{cases} \tag{6.12}$$

In this scenario, the heated region experiences uniaxial compression, while the unheated region undergoes uniaxial traction along the y-axis. This stress state serves to counteract the thermal mismatch between the two regions. Within each region, the stress state remains constant, aligning with the expressions previously provided in (4.21). Notably, the specific case where $2\beta = \pi$ is the only configuration that satisfies the condition $C_3^I - C_3^{II} \neq 0$, as given in (4.26). This observation reinforces the conclusions derived from the dimensional analysis in Section 4.3 of Chapter 4.

To incorporate a length scale into the problem, it becomes necessary to consider a plate with a finite size. However, deriving the Green's function for an arbitrarily positioned glide dislocation within such a configuration introduces significant complexity. As an alternative, an engineering solution can be achieved by adapting the

infinite disk problem. This involves restricting R_+ to a finite value, chosen such that the resulting stress field closely resembles the stress distribution within a finite disk, particularly near the center. By introducing this finite size constraint, the problem gains a physically meaningful length scale, enabling the analysis of stress distributions that are more representative of real-world applications.

Now, consider a circular plate of finite radius R subjected to a temperature increase ΔT over the sector $-\beta < \theta < \beta, 0 \leq r \leq R$. It is conjectured that the stress state near the center of this finite plate closely matches the stress distribution in an infinite plate with arrays of glide dislocations as described in Section 1 of the present chapter. These dislocations are assumed to be distributed along the segments $\theta = \pm\beta, 0 \leq r \leq R_+$. This setup is schematically illustrated in Figure 6.5.

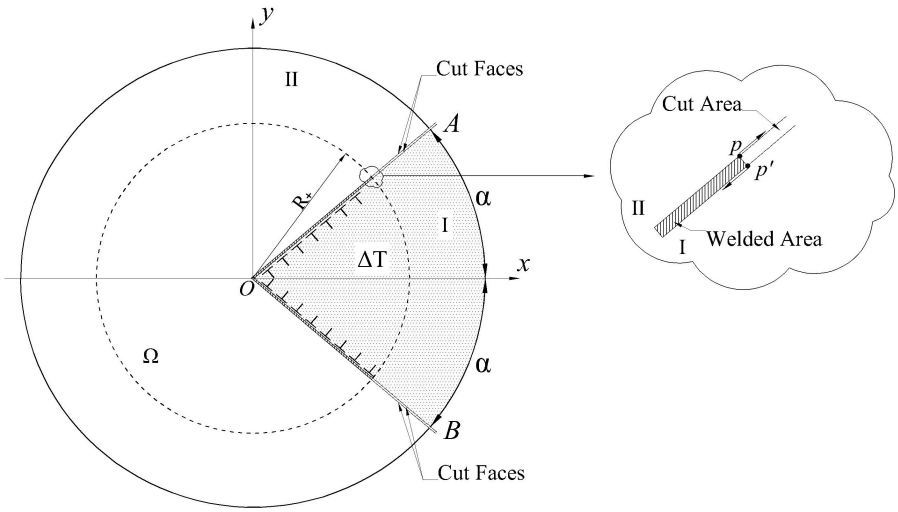

Figure 6.5: Engineering solution. Infinite disk with distributed arrays of dislocations on the segments $\theta = \pm\beta$, $0 \leq r \leq R_+$.

This means that the thermal mismatch is not compensated on the whole interface lines, but just in a portion of them of length R^+. In fact, one has that

$$u(r, \pm\beta + 2\pi) - u(r, \pm\beta) = \begin{cases} \mp\alpha\Delta T r\,, \text{ for } 0 \leq r \leq R_+\,, \\ \mp\alpha\Delta T R_+\,, \text{ for } r > R_+\,. \end{cases} \tag{6.13}$$

The stress state is still given by (6.9a)-(6.9c). It is now necessary to establish a correlation between the actual size of the plate R and the parameter R_+, which represents the length scale for the problem at hand.

6.3 From infinite to a finite disk with a sector at different temperature

The problem under consideration involves a circular disk of finite radius R, where a sector defined by $0 \leq r \leq$ R, and $-\beta \leq \theta \leq \beta$ is subjected to a temperature increment ΔT. To analyze this configuration, thermal stresses are first determined numerically for specific cases using the commercial finite element software Abaqus. Subsequently, an engineering solution based on the analytical model for the infinite plate is proposed, demonstrating excellent agreement with the numerical results.

6.3.1 Numerical solution

The case where $2\beta = \pi/3$ and $\Delta T = 30°\text{C}$ has been implemented in Abaqus/Standard. The model discretizes the disk using 3-node linear triangular elements (CPS3), assuming a generalized plane stress state. The material is considered to be glass with a radius R = 250 mm, Young's modulus E = 70GPa, Poisson's ratio $v = 0.22$, and a coefficient of thermal expansion $\alpha = 9 \times 10^{-6}$ K^{-1}. The resulting stress distribution is illustrated in Figure 6.6.

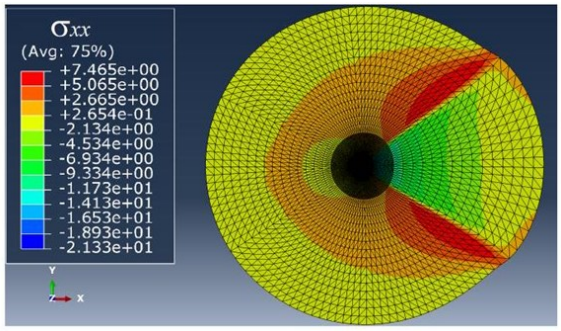

(a)

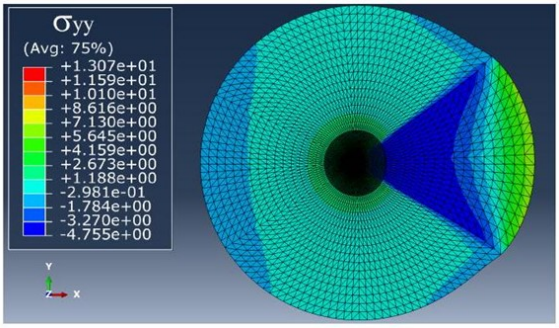

(b)

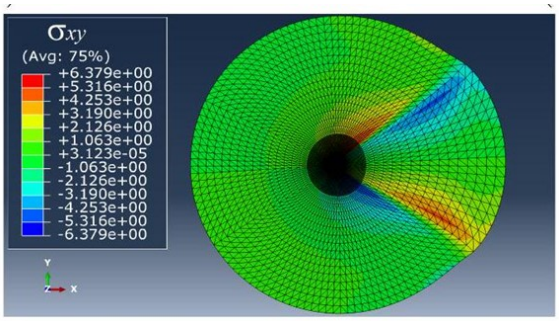

(c)

Figure 6.6: Stress state obtained with Abaqus/Standard software for the case $\Delta T = 30°\text{C}$, $2\beta = \pi/3$ and $R = 250\,\text{mm}$. Stress components: (a) σ_{xx}, (b) σ_{yy} and (c) σ_{xy}. The center of the disk appears black because here the mesh is so fine that it cannot be captured by the image resolution.

A comparison between the numerically obtained stress state and the analytical solution derived from Equations (6.9a)-(6.9c), for $R_+ = 250$ mm, is shown in Figure 6.7. The comparison focuses on the stress components $\sigma_{rr}(r,\theta), \sigma_{\theta\theta}(r,\theta)$ and $\sigma_{r\theta}(r,\theta)$, plotted as functions of the radial coordinate rrr on semi-logarithmic axes for the radial paths $\theta = 0$ and $\theta = \pi$.

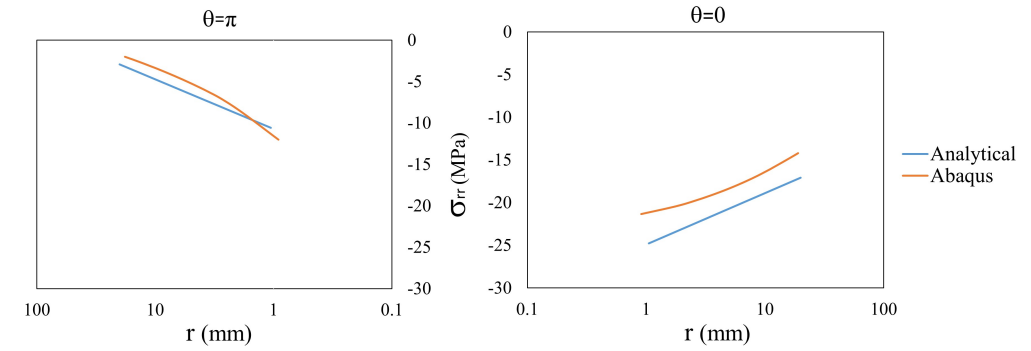

(a)

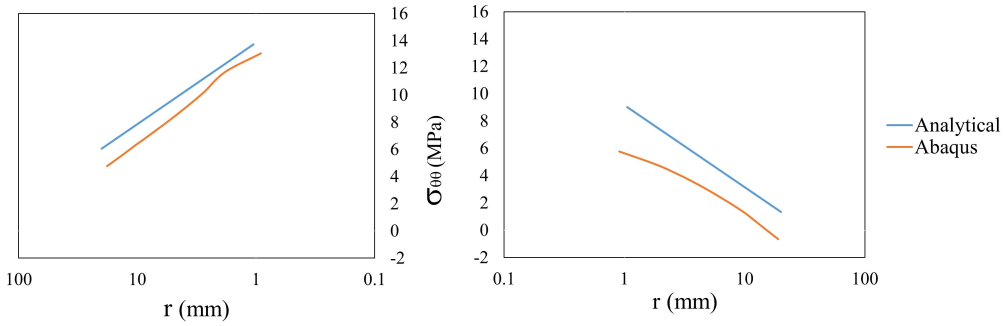

(b)

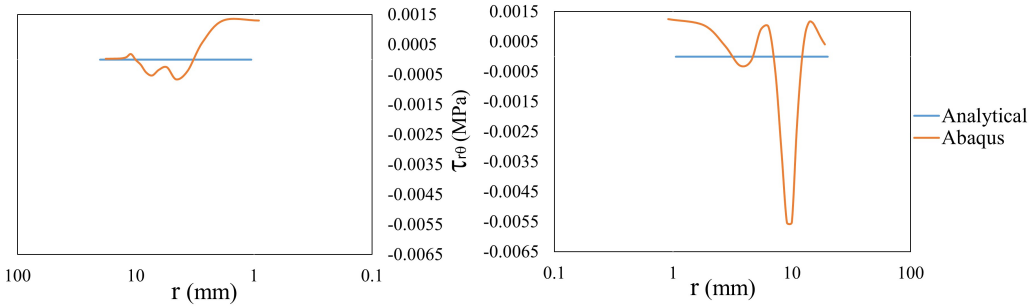

(c)

Figure 6.7: Comparison between the stress states obtained numerically for the finite plate of radius $R = 250\,\text{mm}$, and via the analytical solution for an infinite plate with $R_+ = R$. Stress components (a) $\sigma_{rr}(r,\theta)$, (b) $\sigma_{\theta\theta}(r,\theta)$, (c) $\sigma_{r\theta}(r,\theta)$ as a function of r, on the radial paths $\theta = 0$ and $\theta = \pi$.

Despite employing a highly refined mesh near the center of the disk, the numerical solution in Abaqus exhibits some approximation errors. In particular, the shear stress component $\sigma_{r\theta}$ displays oscillatory behavior around zero, even though it should theoretically vanish due to symmetry. This deviation likely stems from the logarithmic singularity in the stress field, as evident from the analytical expressions (6.9a)-(6.9c).

Furthermore, the numerical and analytical solutions show notable discrepancies for the normal stress components σ_{rr} and $\sigma_{\theta\theta}$. This inconsistency suggests that the assumption $R_+ = R$ does not adequately capture the physical behavior of the system.

6.3.2 Correlation with the infinite plate problem

To improve the agreement between the stress state of the finite-radius disk and the analytical solution (6.9a)-(6.9c) for the infinite disk, we propose a revised parameter selection with $R_+ = R/2$. This adjustment aims to better capture the stress distribution near the center of the finite disk while aligning more closely with the analytical model.
Figures 6.8 and 6.9 are the counterpart of Figure 6.7 for this choice. Here, two different radii, i.e. $R = 500$ mm and $R = 1000$ mm have been respectively considered for the disk; the analytical solutions for the infinite disk obviously correspond to $R_+ = 250$ mm and $R_+ = 500$ mm, respectively.

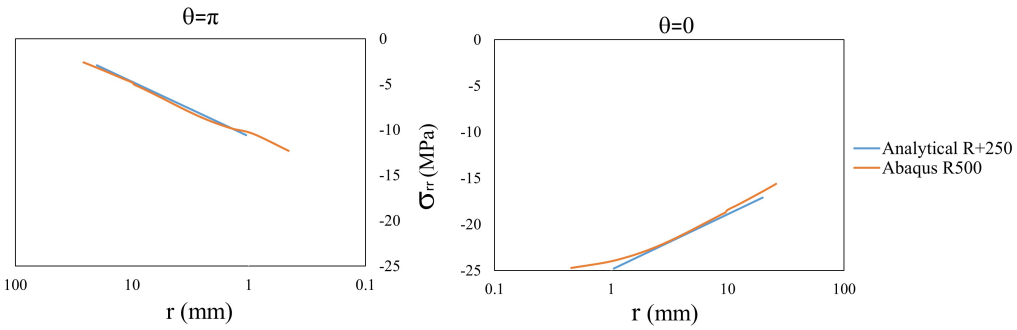

(a)

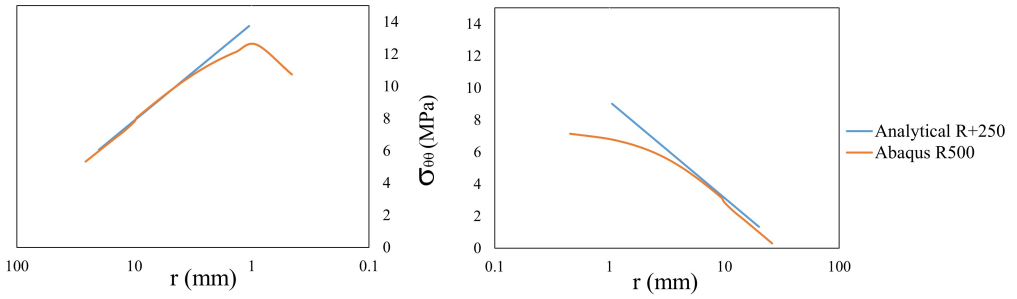

(b)

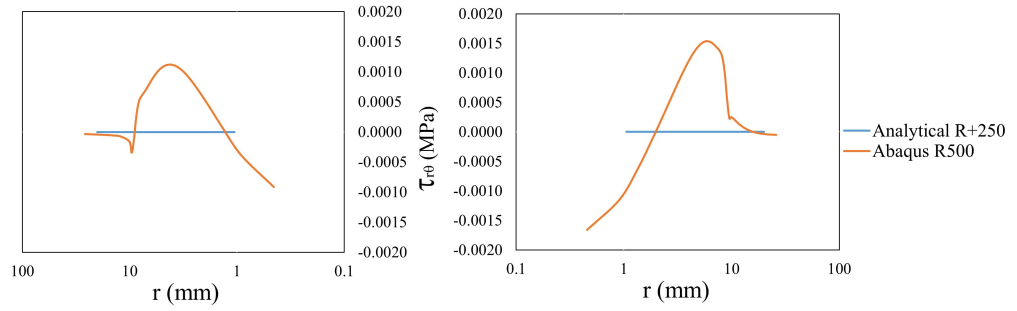

(c)

Figure 6.8: Comparison between the stress states obtained numerically for the finite plate of radius $R = 500\,\text{mm}$, and via the analytical solution for an infinite plate with $R_+ = R/2 = 250\,\text{mm}$. Stress components (a) $\sigma_{rr}(r,\theta)$, (b) $\sigma_{\theta\theta}(r,\theta)$, (c) $\sigma_{r\theta}(r,\theta)$, as a function of r, on the radial paths $\theta = 0$ and $\theta = \pi$.

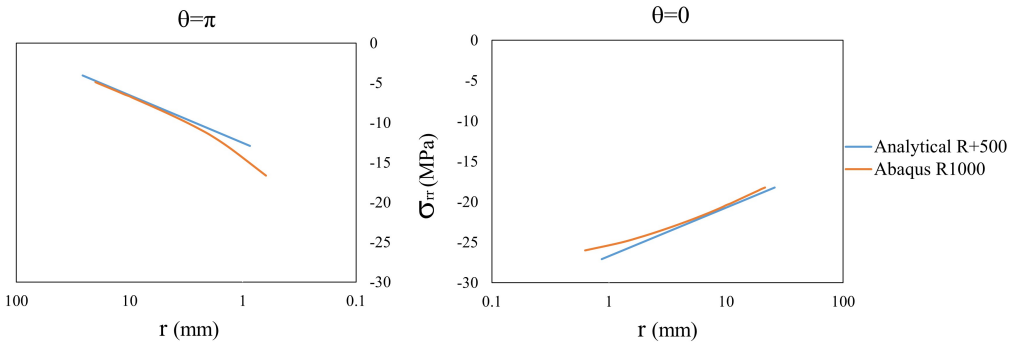

(a)

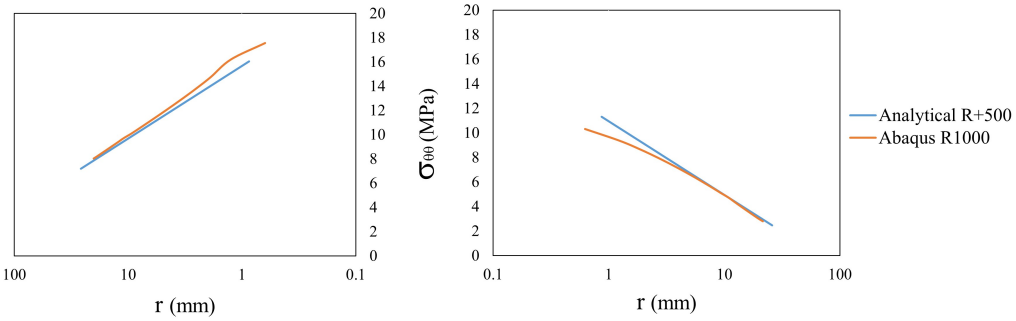

(b)

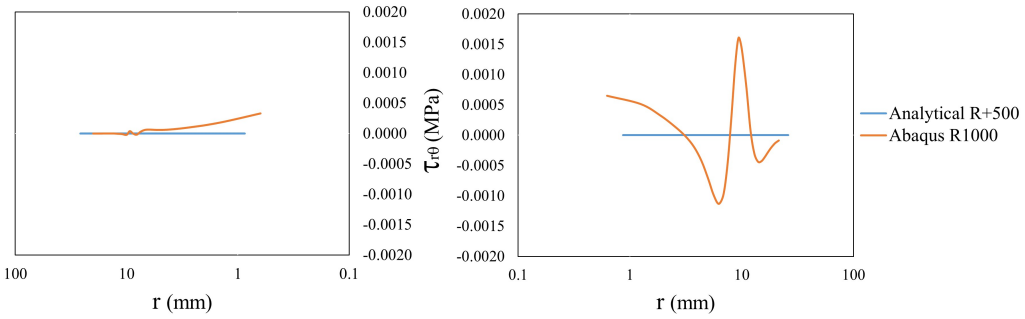

(c)

Figure 6.9: Comparison between the stress states obtained numerically for the finite plate of radius $R = 1000\,\text{mm}$, and via the analytical solution for an infinite plate with $R_+ = R/2 = 500\,\text{mm}$. Stress components (a) $\sigma_{rr}(r,\theta)$, (b) $\sigma_{\theta\theta}(r,\theta)$, (c) $\sigma_{r\theta}(r,\theta)$, as a function of r, on the radial paths $\theta = 0$ and $\theta = \pi$.

The comparison demonstrates a generally excellent agreement between the numerical and analytical solutions. Notably, the graphs show almost complete overlap for $r > 10^{-2}R$. In the vicinity of the center, as $r \to 0$, the analytical solution retains a linear trend in the semi-logarithmic plot. This behavior aligns with expectations, given that the expressions (6.9a)-(6.9c) for the stress components exhibit a logarithmic singularity. Conversely, the numerical solution for the finite-radius disk deviates slightly from this trend near $r = 0$. This deviation likely arises from limitations in the numerical method, particularly in capturing the behavior around singularities.

Additionally, the numerical solution for the shear stress component $\sigma_{r\theta}$ does not

accurately reflect the zero-value dictated by the symmetry of the problem. This discrepancy underscores the challenges associated with numerical modeling of stress states involving logarithmic singularities, even with a refined mesh near the center. Further numerical experiments were conducted for various opening angles 2β and disk radii R. Across all tested configurations, a consistent empirical finding emerged: the analytical solution for the infinite disk aligns well with the numerical solution for the finite disk when $R_+ = R/2$. This observation suggests that the choice $R_+ = R/2$ serves as a practical approximation for bridging the finite and infinite disk solutions.

This empirical result opens the door to the development of approximate engineering formulae for calculating thermal stress in finite disk problems. Such formulae would provide a straightforward and effective means to estimate stress distributions in practical applications, combining the accuracy of analytical solutions with the versatility of numerical methods.

6.3.3 Approximate formulae for the calculation of the thermal stress

As an approximate expression for the stress state in a circular disk of radius R, we propose using the analytical solution derived for the infinite disk, with $R_+ = R/2$. Substituting this value into the Equations (6.9a)-(6.9c) and replacing A with its expression from (6.3), the resulting stress state is obtained as

$$\begin{aligned}\sigma_{rr}\frac{\pi(\kappa+1)}{2\mu\alpha\Delta T} &= \sin(2\beta)\cos(2\theta)\left[1+\log(2r/R)^2\right]\\ &+2\cos^2(\theta-\beta)\Big\{\tan^{-1}\left[\frac{R}{2r\sin(\theta-\beta)}\right]+\tan^{-1}\left[\cot(\theta-\beta)\right]\Big\}\\ &-2\cos^2(\theta+\beta)\Big\{\tan^{-1}\left[\frac{R}{2r\sin(\theta+\beta)}\right]+\tan^{-1}\left[\cot(\theta+\beta)\right]\Big\},\end{aligned} \tag{6.14a}$$

$$\begin{aligned}\sigma_{\theta\theta}\frac{\pi(\kappa+1)}{2\mu\alpha\Delta T} &= -\sin(2\beta)\cos(2\theta)\left[1+\log(2r/R)^2\right]\\ &+2\sin^2(\theta-\beta)\Big\{\tan^{-1}\left[\frac{R}{2r\sin(\theta-\beta)}\right]+\tan^{-1}\left[\cot(\theta-\beta)\right]\Big\}\\ &-2\sin^2(\theta+\beta)\Big\{\tan^{-1}\left[\frac{R}{2r\sin(\theta+\beta)}\right]+\tan^{-1}\left[\cot(\theta+\beta)\right]\Big\},\end{aligned} \tag{6.14b}$$

$$\begin{aligned}\sigma_{r\theta}\frac{\pi(\kappa+1)}{2\mu\alpha\Delta T} &= -\sin(2\beta)\sin(2\theta)\left[1+\log(2r/R)^2\right]\\ &-\sin 2(\theta-\beta)\Big\{\tan^{-1}\left[\frac{R}{2r\sin(\theta-\beta)}\right]+\tan^{-1}\left[\cot(\theta-\beta)\right]\Big\}\\ &+\sin 2(\theta+\beta)\Big\{\tan^{-1}\left[\frac{R}{2r\sin(\theta+\beta)}\right]+\tan^{-1}\left[\cot(\theta+\beta)\right]\Big\}.\end{aligned} \tag{6.14c}$$

Next, we examine the stress distribution along a circular path of radius $r = 10$ mm centered within the disk. Figures 6.10 and 6.11 illustrate the stress components $\sigma_{rr}(r,\theta)$, $\sigma_{\theta\theta}(r,\theta)$ as functions of θ, calculated using the analytical expressions

(6.14a)-(6.14c). Results are presented for two cases: $R = 500$ mm and $R = 1000$ mm. These analytical results are compared with corresponding numerical solutions obtained through Abaqus.

The comparison reveals a highly satisfactory agreement between the analytical and numerical solutions. This consistency highlights the effectiveness of the proposed approach, where the analytical solution for the infinite disk with $R_+ = R/2$ is used to approximate the stress state in a finite-radius disk. The close match between the two methods reinforces the reliability of the analytical model for predicting thermal stress in circular disks and validates its use as an engineering approximation for practical applications.

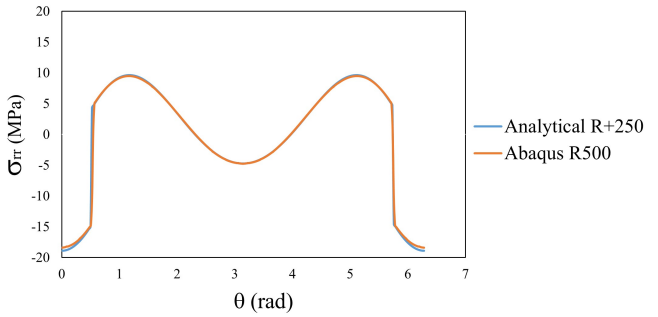

(a)

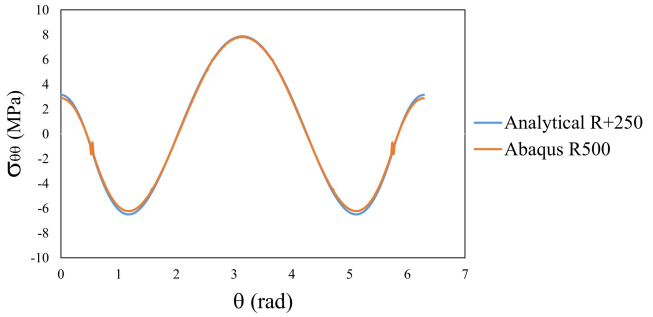

(b)

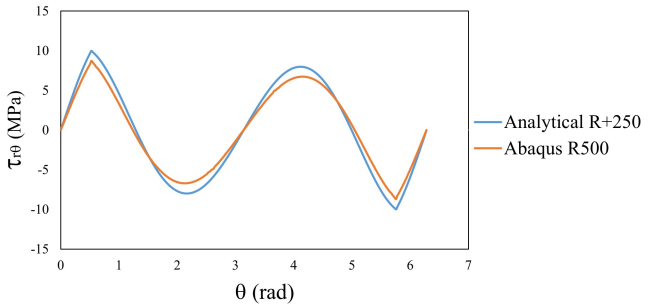

(c)

Figure 6.10: Circular plate of radius $R = 500\,\text{mm}$ subjected to a thermal increment $\Delta T = 30°\text{C}$ on a sector of width $2\beta = \pi/3$. Stress components (a) σ_{rr}. (b) $\sigma_{\theta\theta}$ on a circular path of radius $r = 10mm$ as a function of θ. Comparison between the approximate formulae (6.14) and the numerical solution obtained with Abaqus.

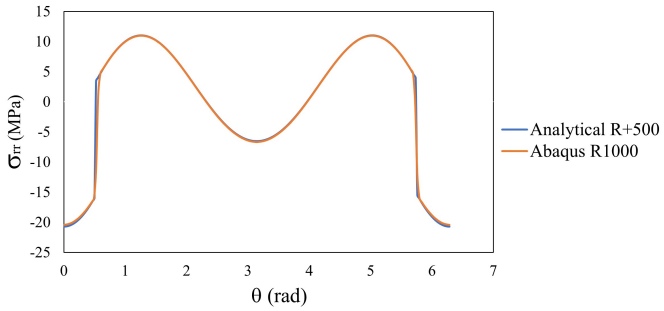

(a)

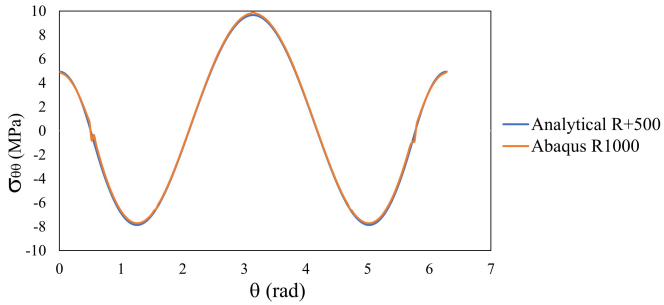

(b)

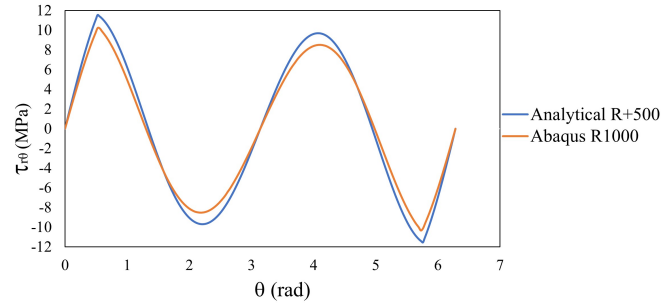

(c)

Figure 6.11: Circular plate of radius $R = 1000\,\text{mm}$ subjected to a thermal increment $\Delta T = 30°\text{C}$ on a sector of width $2\beta = \pi/3$. Stress components (a) σ_{rr}. (b) $\sigma_{\theta\theta}$ on a circular path of radius $r = 10mm$ as a function of θ. Comparison between the approximate formulae (6.14) and the numerical solution obtained with Abaqus.

6.4 Conclusions

The linear elastic problem of an infinite disk, where a sector with an opening angle 2β is subjected to a temperature variation, exhibits a peculiar and problematic behavior. The thermal strain generates an unbounded stress state across the disk, except in the special case where $2\beta = \pi$. This issue arises due to the absence of an intrinsic length scale in the problem, which prevents the deformation from being congruent between the sector and its complementary region. Consequently, when $2\beta \neq \pi$, the stresses cannot be reconciled, resulting in inconsistencies in the elastic solution.

To better understand and characterize this issue, an alternative approach was proposed. The method involves making ideal cuts along the sector boundaries, al-

lowing the sector to expand thermally, welding it back in its deformed state, and introducing distributed dislocations to counteract the mismatch. This approach reformulates the problem as a sequence of elastic solutions, with the length of the dislocation arrays gradually increasing toward infinity. Although this leads to stresses that grow without bounds, the sequence of solutions consistently exhibits a logarithmic singularity at the vertex of the sector. This singularity aligns with known results for elastic problems involving wedges and provides valuable insights into the stress state.

For a finite disk, the introduction of a physical length scale-the disk radius-results in a non-uniform thermal stress distribution. Numerical simulations using a finite element method (FEM) have confirmed this behavior. Based on these findings, an engineering approximation was proposed: the stress state near the center of a finite disk is correlated to the stress state of an infinite disk, with the reconciling dislocation length set to $R_+ = R/2$, where R is the disk radius. This approximation yielded excellent agreement with numerical results for various configurations. Such an approach has practical potential for applications, such as calculating thermal stresses in materials like glass panes exposed to uneven heating due to shadows.

While the proposed engineering approximation is still preliminary, it suggests a promising framework for addressing elastic problems in infinite bodies with non-physical behavior. The reformulation of these problems as a sequence of approximations allows for solutions that incorporate singularities, which can be adapted to finite-sized bodies. This approach circumvents the analytical challenges posed by finite geometries and provides a foundation for deriving stress approximations with theoretical support.

Future work should focus on further validation of the proposed method for finite disks, including experimental and numerical studies to refine the coefficients defining the stress values. These investigations could expand the method's applicability and enhance its reliability for practical engineering problems. By bridging theoretical insights and numerical results, this study highlights a robust pathway for analyzing thermal stresses in both infinite and finite elastic bodies.

Appendices

Appendix A

Displacement Field from Cesaro's Representation

Cesaro's line integral representation [148] permits a direct integration of the linearized straindisplacement equations. This is used here to state the compatibility conditions in terms of displacement on the common lines in the three-wedge problem of Figure 5.2 in Chapter 5. Although the displacement field for the wedge problem loaded by a tip couple is well known [73], we are interested in using the argument proposed in [139, 140] by Fosdick and Royer-Carfagni, whose major advantage is that the compatibility conditions can be directly stated in terms of stress components.

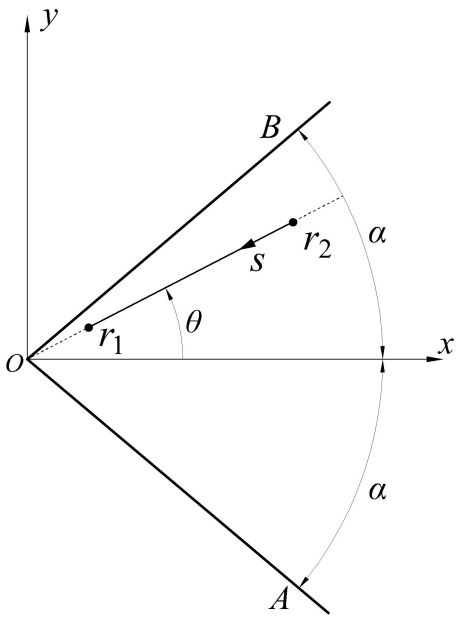

Figure A.1: Radial path for the application of Cesaro's line integral representation, for the wedge problem.

Denote with $\Gamma : [0, \bar{s}] \subset \mathbb{R} \to \mathcal{B}$ a regular curve in $\mathcal{B}$ via the parametrization $\boldsymbol{x} = \boldsymbol{x}(s), s \in [0, \bar{s}]$. If $\boldsymbol{E}(s) := \boldsymbol{E}(\boldsymbol{x}(s))$ is the infinitesimal strain tensor, Cesaro's Representation Theorem states that the displacement $\boldsymbol{v}(\bar{s}) := \boldsymbol{v}(\boldsymbol{x}(\bar{s}))$ at $\boldsymbol{x}(\bar{s}) \in \Gamma$, can be obtained as

$$\begin{aligned} \upsilon(\bar{s}) &= \mathbf{a} + \mathbf{W}\left(\mathbf{x}\left(\bar{s}\right) - \mathbf{x}\left(0\right)\right) \\ &\quad + \int_0^{\bar{s}} \left[\mathbf{E}\left(s\right) + \left(\nabla\mathbf{E}\left(s\right) - \nabla\mathbf{E}^T\left(s\right)\right)\left(\mathbf{x}\left(\bar{s}\right) - \mathbf{x}\left(s\right)\right)\right]\mathbf{x}'\left(s\right)\, ds\,, \end{aligned} \tag{A.1}$$

where $\mathbf{a} \in \mathbb{V}^3$ and $\mathbf{W} \in$ Skew are arbitrary constants, respectively representing a translation and an infinitesimal rigid body rotation about $\boldsymbol{x}(0)$.
Let $\boldsymbol{e}_r \in \mathbb{V}^2$ and $\boldsymbol{e}_\theta \in \mathbb{V}^2$ denote the unit reference vectors of the polar coordinate system, such that $\boldsymbol{E} = \varepsilon_{rr}\left(\boldsymbol{e}_r \otimes \boldsymbol{e}_r\right) + \varepsilon_{\theta\theta}\left(\boldsymbol{e}_\theta \otimes \boldsymbol{e}_\theta\right) + \varepsilon_{r\theta}\left(\boldsymbol{e}_r \otimes \boldsymbol{e}_\theta + \boldsymbol{e}_\theta \otimes \boldsymbol{e}_r\right)$. The transpose of a third order tensor $\mathbf{A}$ is defined as follows: $\mathbf{B} = \mathbf{A}^T$ if $((\mathbf{A}\mathbf{w})\boldsymbol{v}) \cdot \boldsymbol{u} = ((\mathbf{B}\boldsymbol{u})\boldsymbol{w}) \cdot \boldsymbol{v}$ for any arbitrary vectors $\boldsymbol{u}, \boldsymbol{v}$ and $\boldsymbol{w}$. In dyadic notation, if $\mathbf{A} = \boldsymbol{a} \otimes \boldsymbol{b} \otimes \boldsymbol{c}$, then $\mathbf{A}^T = \boldsymbol{b} \otimes \boldsymbol{c} \otimes \boldsymbol{a}$. For the case at hand, one finds that

$$\begin{aligned} \nabla\mathbf{E} - \nabla\mathbf{E}^T = &[\frac{1}{r}(\varepsilon_{rr,\theta} - 2\varepsilon_{r\theta}) - \varepsilon_{r\theta,r}](\mathbf{e}_r \otimes \mathbf{e}_r \otimes \mathbf{e}_\theta - \mathbf{e}_\theta \otimes \mathbf{e}_r \otimes \mathbf{e}_r) + \\ &[\frac{1}{r}(\varepsilon_{rr} + 2\varepsilon_{r\theta,\theta} - 2\varepsilon_{\theta\theta}) - \varepsilon_{\theta\theta,r}](\mathbf{e}_r \otimes \mathbf{e}_\theta \otimes \mathbf{e}_\theta - \mathbf{e}_\theta \otimes \mathbf{e}_\theta \otimes \mathbf{e}_r)\,. \end{aligned}$$

For the wedge problem, consider a radial path of the type represented in Fig. A.1, comprised between the points $r = r_1$ and $r = r_2$, defined by

$$\mathbf{x} = \mathbf{x}(s) = (r_2 - s)\,\mathbf{e}_r\,, \quad s \in [0, r_2 - r_1] \quad \text{and} \quad \theta = \text{const}\,. \tag{A.2}$$

The path is directed from the periphery towards the vertex because, on the one hand, there is a tip singularity in the wedge problem and the path should tend towards this point; on the other hand, we expect that the displacement tends to zero as $r \to \infty$. Since $s = r_2 - r$, one obtains

$$\mathbf{x}'\left(s\right) ds = \mathbf{e}_r\, dr, \tag{A.3a}$$

$$\mathbf{x}\left(r_2 - r_1\right) - \mathbf{x}(0) = -\left(r_2 - r_1\right)\mathbf{e}_r, \tag{A.3b}$$

$$\mathbf{x}\left(r_2 - r_1\right) - \mathbf{x}(s) = -\left(r - r_1\right)\mathbf{e}_r, \tag{A.3c}$$

Using (A.3a)-(A.3c) and (A.2), one finds the integral representation for the displacement field $\boldsymbol{v} = v_r\boldsymbol{e}_r + v_\theta\boldsymbol{e}_\theta$ in the form

$$\begin{aligned} \upsilon(r_1, \theta) &= \mathbf{a} - \mathbf{W}\left(r_2 - r_1\right)\mathbf{e}_r \\ &\quad - \int_{r_1}^{r_2} \left\{\varepsilon_{rr}\mathbf{e}_r + \left[\varepsilon_{r\theta} + \left(r - r_1\right)\left[\frac{1}{r}\left(\varepsilon_{rr,\theta} - 2\varepsilon_{r\theta}\right) - \varepsilon_{r\theta,r}\right]\right]\mathbf{e}_\theta\right\} dr\,. \end{aligned} \tag{A.4}$$

Hence, the components of $\boldsymbol{v}$ read

$$v_r(r_1, \theta) = a_r - \int_{r_1}^{r_2} \varepsilon_{rr} dr\,, \tag{A.5}$$

$$\begin{aligned} \upsilon_\theta(r_1,\theta) &= a_\theta - \omega(r_2 - r_1) \\ &\quad - \int_{r_1}^{r_2} \left[\varepsilon_{r\theta} + (r - r_1) \left(\frac{1}{r}(\varepsilon_{rr,\theta} - 2\varepsilon_{r\theta}) - \varepsilon_{r\theta,r} \right) \right] dr \,, \end{aligned} \tag{A.6}$$

where, a_r and a_θ are the components of $\boldsymbol{a}$, whereas, ω is the magnitude of the axial vector associated with the skew tensor $\boldsymbol{W}$.
We are interested in the particular case in which $\theta \to \pm\alpha$, i.e., when the radial path approaches the free borders of the wedge. Clearly, $\varepsilon_{r\theta} = \sigma_{r\theta}/G$, where G is the elastic shear modulus of the material. Since, from (3.1c),

$$\lim_{\theta\to\pm\alpha} \varepsilon_{r\theta}(r,\theta) = 0 \,, \quad \lim_{\theta\to\pm\alpha} \varepsilon_{r\theta,r}(r,\theta) = 0 \,, \tag{A.7}$$

the expression (A.6) can be further simplified as

$$\upsilon_\theta(r_1,\pm\alpha) = a_\theta - \omega(r_2 - r_1) - \int_{r_1}^{r_2} \frac{r - r_1}{r} \varepsilon_{rr,\theta} dr \,. \tag{A.8}$$

The equations (A.5) and (A.8), will be used to identify the compatibility condition for the three-wedge problem of Figure 5.2.

Appendix B

Centre of Dilatation; a Potential Solution to The Second Problem

Consider a two-dimensional linear elastic infinite body, in generalized plane stress or plane strain, a circular region of which, of radius a, is subjected to a temperature variation ΔT. As in Section 3.2 of Chapter 3, let α denote the effective coefficient of thermal expansion, μ the elastic shear modulus, ν the Poisson's ratio, κ Kolosov's constant.

With respect to a polar coordinate system (r, θ), the state of stress for $r \geq a$ is defined by the Airy stress function [150]

$$\phi = -\pi a^2 Q \Delta T \log r \,, \text{with } \; Q = \frac{4\alpha\mu}{\pi(\kappa+1)} \,. \tag{B.1}$$

A *center of dilatation* at $r = 0$ is defined by letting $a \to 0$ and $\Delta T \to \infty$ in such a way that $\pi a^2 \Delta T \to 1$, i.e., a unitary center of dilatation.

If a very small region dA, assimilable to infinitesimal circle centered at the origin, is subjected to a temperature variation ΔT, the resulting state of stress is, from (B.1), defined by the Airy stress function $d\phi = -Q dA \Delta T \log r$. If the heated area dA is located at $(r, \theta) = (r_0, \bar{\theta})$, reasoning as in Figure 6.5, one finds that the Airy stress function reads

$$d\phi = -\frac{1}{2} Q \Delta T \log[r^2 + r_0^2 - 2 r r_0 \cos(\theta - \bar{\theta})] dA \,. \tag{B.2}$$

If the region subjected to the temperature variation ΔT is defined by $R_- \leq r_0 \leq R_+$ and $-\beta \leq \bar{\theta} \leq \beta$, summing up the various contributions, one finds

$$\phi(r, \theta) = \int_{r_0=R_-}^{r_0=R_+} \int_{\bar{\theta}=-\beta}^{\bar{\theta}=\beta} -\frac{1}{2} Q \Delta T \log[r^2 + r_0^2 - 2 r r_0 \cos(\theta - \bar{\theta})] r_0 dr_0 d\bar{\theta} \,. \tag{B.3}$$

This is the counterpart of Equation (6.6), obtained with the distributed dislocation approach. There is a formal similarity between (6.6) and (B.3). In both cases, the limit exists for $R_- \to 0$, but the integral does not converge for $R_+ \to +\infty$. However, (6.6) requires a double integration in r_0 and $\bar{\theta}$, whereas only integration over r_0 is necessary for (6.6). Therefore, the approach proposed in Section 6.1 of Chapter 6 is reputed simpler.

There is however a substantial difference. Equation (B.3) provides the Airy function for an infinite disk with a heated portion of finite size. On the other hand, Equation (6.6) provides the solution for the case in which an infinite sector is heated, but the deformation is reconciled only a limited portion of the interface. The discussion of the sequence of solutions that can be obtained from (B.3) as $R_+ \to \infty$ follows the same lines of Section 6.2 of Chapter 6, but goes beyond the scope of this article.

Bibliography

[1] V. Ramachandran. *Failure analysis of engineering structures: methodology and case histories*. ASM International, 2005.

[2] Glenn B Sinclair. "Stress singularities in classical elasticity-I: Removal, interpretation, and analysis". In: *Journal of Applied Mechanics* 57.4 (2004), pp. 251–298.

[3] E. Sternberg. *On singular problems in linearized and finite elastostatics*. Amsterdam: North-Holland, Aug. 1980, pp. 33–43.

[4] Glenn B Sinclair. "Stress singularities in classical elasticity-II: Asymptotic identification". In: *Journal of Applied Mechanics* 57.5 (2004), pp. 385–439.

[5] William Thomson. "Note on the integration of the equations of equilibrium of an elastic solid". In: *Cambridge and Dublin Mathematical Journal* 3 (1848), pp. 87–89.

[6] J. Boussinesq. "Équilibre d'un demi-espace élastique isotrope supportant des charges variables en l'absence de gravité". French. In: *Comptes Rendus de l'Académie des Sciences de Paris* 86 (1878), pp. 1260–1263.

[7] Raymond D Mindlin. "Force at a point in the interior of a semi-infinite solid". In: *physics* 7.5 (1936), pp. 195–202.

[8] Harry George Poulos and Edward Hughesdon Davis. "Elastic solutions for soil and rock mechanics". In: *(No Title)* (1974).

[9] E. Sternberg and R. A. Eubanks. "On the concept of concentrated loads and an extension of the uniqueness theorem in the linear theory of elasticity". In: *Journal of Rational Mechanics and Analysis* 4.1 (1955), p. 135.

[10] A. E. H. Love. *A Treatise on the Mathematical Theory of Elasticity*. Cambridge: Cambridge University Press, 2013.

[11] M. J. Turteltaub and E. Sternberg. "On concentrated loads and Green's functions in elastostatics". In: *Archive for Rational Mechanics and Analysis* 29.3 (1968), p. 193.

[12] St Timoshenko. "Goodier. JN, Theory of Elasticity". In: *New. York McGraw—Hil1* 970.4 (1970), pp. 279–291.

[13] INGLIS CE. "Stresses in a plate due to the presence of cracks and sharp corners". In: *Trans Inst Naval Archit* 55 (1913), pp. 219–241.

[14] M. L. Williams. "Stress singularities resulting from various boundary conditions in angular corners of plates in extension". In: *Journal of Applied Mechanics* 19.4 (1952), pp. 526–528.

[15] ML102211 Williams. "The stresses around a fault or crack in dissimilar media". In: *Bulletin of the seismological society of America* 49.2 (1959), pp. 199–204.

[16] MA Sadowsky. "Two-dimensional problems of elasticity theory". In: *Z. Angew. Math. Mech* 8.2 (1928), pp. 107–121.

[17] BM Abramov et al. "The problem of contact of an elastic infinite half-plane with an absolutely rigid rough foundation". In: *CR (Dokl.) Acad. Sci. URSS*. Vol. 17. 1937, pp. 173–178.

[18] JP Dempsey and GB625955 Sinclair. "On the singular behavior at the vertex of a bi-material wedge". In: *Journal of Elasticity* 11.3 (1981), pp. 317–327.

[19] William Thomson and Peter Guthrie Tait. *Treatise on natural philosophy*. CUP Archive, 2022.

[20] Max Knein. *Zur theorie des druckversuchs*. Springer, 1926.

[21] G Kolossoff. "Über einige Eigenschaften des ebenen Problems der Elastizitätstheorie". In: *Ztschr. f. Math. u. Phys* (1914), pp. 383–409.

[22] J. P. Dempsey and G. B. Sinclair. "On the Stress Singularities in the Plane Elasticity of the Composite Wedge". In: *Journal of Elasticity* 9 (1979), pp. 373–391.

[23] E. Z. Lajtai. "A theoretical and experimental evaluation of the Griffith theory of brittle fracture". In: *Tectonophysics* 11.2 (1971), pp. 129–156.

[24] G. I. Barenblatt. "The formation of equilibrium cracks during brittle fracture. General ideas and hypotheses: axially-symmetric cracks". In: *Journal of Applied Mathematics and Mechanics (PMM)* 23 (1959), pp. 434–444.

[25] D. A. Hills et al. "A review of asymptotic procedures in stress analysis: known solutions and their applications". In: *The Journal of Strain Analysis for Engineering Design* 39.6 (2004), pp. 553–568.

[26] SD Carothers. "XXVI.—Plane strain in a wedge, with applications to masonry dams". In: *Proceedings of the Royal Society of Edinburgh* 33 (1914), pp. 292–306.

[27] L. Evangelisti et al. "An experimental investigation of the thermal performance of a building solar shading device". In: *Journal of Building Engineering* 28 (2020).

[28] L. Galuppi and G. Royer-Carfagni. "Thermal analysis of architectural glazing in uneven conditions based on Biot's variational principle: Part I–Description of the finite element modelling". In: *Glass Structures and Engineering* 8.1 (2023), pp. 41–56.

[29] L. Galuppi and G. Royer-Carfagni. "Thermal analysis of architectural glazing in uneven conditions based on Biot's variational principle: Part II–Validation and case-studies". In: *Glass Structures and Engineering* 8.1 (2023), pp. 57–80.

[30] *NF DTU 39 P3 Travaux de bâtiment - Travaux de vitrerie-miroiterie - Partie 3: Mémento calculs des contraintes thermiques*. 2006.

[31] C. Hwu. "Thermal stresses in an anisotropic plate disturbed by an insulated elliptic hole or crack". In: *Journal of Applied Mechanics* 57.4 (1990), pp. 916–922.

[32] W. Thompson and P. G. Tait. *Treatise on Natural Philosophy (reprinted as Principles of Mechanics and Dynamics)*. New York: Dover, 1962.

[33] E. Sternberg and F. Rosenthal. "The elastic sphere under concentrated loads". In: *Journal of Applied Mechanics* 19.4 (1952), p. 413.

[34] M. M. Frocht and Jr. Cuernsey R. *A special investigation to develop a general method for three-dimensional photoelastic stress analysis*. Tech. rep. Report under Contract NAw-5959. NACA, Sept. 1951.

[35] E. Sternberg and R. A. Eubanks. "On the singularity at a concentrated load applied to a curved surface". In: *Proceedings of the Second U.S. National Congress of Applied Mechanics*. Ann Arbor, Mich.: ASME, New York, 1954.

[36] G. L. Neidhardt and E. Sternberg. "On the transmission of a concentrated load into the interior of an elastic body". In: *Journal of Applied Mechanics* 23.4 (1956), p. 541.

[37] Andrzej Seweryn and Krzysztof Molski. "Elastic stress singularities and corresponding generalized stress intensity factors for angular corners under various boundary conditions". In: *Engineering Fracture Mechanics* 55.4 (1996), pp. 529–556.

[38] Chongmin Song. "Evaluation of power-logarithmic singularities, T-stresses and higher order terms of in-plane singular stress fields at cracks and multi-material corners". In: *Engineering Fracture Mechanics* 72.10 (2005), pp. 1498–1530.

[39] J. K. Knowles and T. A. Pucik. "Uniqueness for plane crack problems in linear elastostatics". In: *Journal of Elasticity* 1.3 (1973), p. 155.

[40] J. R. Rice. "Mathematical analysis in the mechanics of fracture". In: *Fracture*. Vol. 11. New York: Academic Press, 1968. Chap. 3.

[41] N. I. Muskhelishvili. *Some Basic Problems of the Mathematical Theory of Elasticity*. English translation. Groningen: Noordhoff, 1953.

[42] J. R. Rice. "A path-independent integral and the approximate analysis of strain concentrations by notches and cracks". In: *Journal of Applied Mechanics* 35.2 (1968), p. 379.

[43] J. D. Eshelby. "The continuum theory of lattice defects". In: *Progress in Solid State Physics*. Vol. 3. New York: Academic Press, 1956.

[44] L. B. Freund. "Stress intensity factor calculations based on a conservation integral". In: *International Journal of Solids and Structures* 14.3 (1978), p. 241.

[45] J. K. Knowles and E. Sternberg. "On a class of conservation laws in linearized and finite elastostatics". In: *Archive for Rational Mechanics and Analysis* 44.3 (1972), p. 187.

[46] Andrei Kotousov and Yaw Tong Lew. "Stress singularities resulting from various boundary conditions in angular corners of plates of arbitrary thickness in extension". In: *International Journal of Solids and Structures* 43.17 (2006), pp. 5100–5109.

[47] M. L. Williams. “On the stress distribution at the base of a stationary crack”. In: *Journal of Applied Mechanics* 24 (1957), pp. 109–114.

[48] M. L. Williams and R. L. Chapkis. “Stress singularities for a sharp-notched polar orthogonal plate”. In: *Proceedings of the 3rd U.S. National Congress of Applied Mechanics*. 1958, pp. 281–287.

[49] Marco Paggi and Alberto Carpinteri. “On the stress singularities at multi-material interfaces and related analogies with fluid dynamics and diffusion”. In: *Applied Mechanics Reviews* 61.2 (2008), p. 020801.

[50] Chiung-Shiann Huang and A. W. Leissa. “Stress singularities in bimaterial bodies of revolution”. In: *Computers and Structures* 82.4 (2008), pp. 488–498.

[51] Alberto Carpinteri and Marco Paggi. “Analytical study of the singularities arising at multi-material interfaces in 2D linear elastic problems”. In: *Engineering Fracture Mechanics* 74.1–2 (2007), pp. 59–74.

[52] Hua-Peng Chen. “Stress singularities in anisotropic multi-material wedges and junctions”. In: *International Journal of Solids and Structures* 35.11 (1998), pp. 1057–1073.

[53] Paul E. W. Labossiere and Martin L. Dunn. “Stress intensities at interface corners in anisotropic bimaterials”. In: *Engineering Fracture Mechanics* 62.6 (1999), pp. 555–576.

[54] Degang Zhao, Hanquan Wang, and Yang Xiang. “Asymptotic behaviors of the stress fields in the vicinity of dislocations and dislocation segments”. In: *Philosophical Magazine* 92.18 (2012), pp. 2351–2374.

[55] John Douglas Eshelby. “The force on an elastic singularity”. In: *Collected Works of J. D. Eshelby*. Dordrecht: Springer, 2006, pp. 61–86.

[56] Jacques Friedel. *Dislocations: International Series of Monographs on Solid State Physics*. Vol. 3. Elsevier, 2013.

[57] A. H. Cottrell. “Theory of dislocations”. In: *Progress in Metal Physics* 4 (1953), pp. 205–264.

[58] J. Dundurs and T. Mura. “Interaction between an edge dislocation and a circular inclusion”. In: *Journal of the Mechanics and Physics of Solids* 12 (1964), pp. 177–189.

[59] J. Dundurs and A. C. Gangadharan. “Edge dislocation near an inclusion with a slipping interface”. In: *Journal of the Mechanics and Physics of Solids* 17 (1969), pp. 459–471.

[60] J. Dundurs and X. Markenscoff. “A Green’s function formulation of anti-cracks and their interaction with load-induced singularities”. In: *ASME Journal of Applied Mechanics* 56 (1989), pp. 550–555.

[61] Vito Volterra. “Sur l’équilibre des corps élastiques multiplement connexes”. In: *Annales scientifiques de l’École normale supérieure* 24 (1907), pp. 401–517.

[62] Tomohito Tsuru. “Descriptions of Dislocation via First Principles Calculations”. In: *The Plaston Concept: Plastic Deformation in Structural Materials*. Springer Nature Singapore, 2022, pp. 91–115.

[63] Eli Sternberg. “On singular problems in linearized and finite elastostatics”. In: *Theoretical and Applied Mechanics*. North-Holland Amsterdam. 1980, pp. 33–43.

[64] R. J. Payne and Robin John Knops. *Uniqueness Theorems in Linear Elasticity*. Vol. 19. Springer Tracts in Natural Philosophy. Springer, 1971.

[65] R. Tiffen. “Uniqueness Theorems of Two-Dimensional Elasticity Theory”. In: *The Quarterly Journal of Mechanics and Applied Mathematics* 5.2 (1952), pp. 237–252.

[66] I. Guerrero and M. J. Turteltaub. “The Elastic Sphere Under Arbitrary Concentrated Surface Loads”. In: *Journal of Elasticity* 2 (1972), pp. 21–33.

[67] Antonino Favata. “On the Kelvin Problem”. In: *Journal of Elasticity* 109 (2012), pp. 189–204.

[68] Q. G. Liu and B. Šarler. “Non-Singular Method of Fundamental Solutions for Two Dimensional Isotropic Elasticity Problems”. In: *Computer Modeling in Engineering & Sciences* 91.4 (2013), pp. 235–266.

[69] E. Sternberg and W. T. Koiter. “The wedge under a concentrated couple: a paradox in the two-dimensional theory of elasticity”. In: *Journal of Applied Mechanics* 146 (1958), pp. 575–581.

[70] J. R. Barber. “Wedge Problems”. In: *Elasticity*. Springer Netherlands, 2009, pp. 149–170.

[71] Andreas Rössle. “Corner Singularities and Regularity of Weak Solutions for the Two-Dimensional Lamé Equations on Domains with Angular Corners”. In: *Journal of Elasticity and the Physical Science of Solids* 60 (2000), pp. 57–75.

[72] D. B. Bogy. “Two edge-bonded elastic wedges of different materials and wedge angles under surface tractions”. In: *Journal of Applied Mechanics* 38.2 (1971), pp. 377–386.

[73] J. Dundurs and X. Markenscoff. “The Sternberg-Koiter conclusion and other anomalies of the concentrated couple”. In: *Journal of Applied Mechanics* 56.2 (1989), pp. 240–245.

[74] H. Neuber. “Lösung des Carothers Problems mittels Prinzipien der Kraftübertragung (Keil mit Moment an der Spitze)”. In: *Zeitschrift für Angewandte Mathematik und Mechanik* 43.4–5 (1963), pp. 221–228.

[75] P. Villaggio. “Some extensions of Carothers’s paradox in plane elasticity”. In: *Mathematics and Mechanics of Solids* 3.1 (1998), pp. 17–28.

[76] J. P. Dempsey. “The wedge subjected to tractions: a paradox resolved”. In: *Journal of Elasticity* 11.1 (1981), pp. 1–10.

[77] D. Leguillon. “Sur le moment ponctuel appliqué à un secteur: le paradoxe de Sternberg-Koiter”. In: *Comptes Rendus de l’Académie des Sciences Paris, Series II* 307 (1988), pp. 1741–1746.

[78] D. B. Bogy. “On the problem of edge-bonded elastic quarter-planes loaded at the boundary”. In: *International Journal of Solids and Structures* 6.9 (1970), pp. 1287–1313.

[79] C. J. Tranter. “Integral transforms in mathematical physics”. In: *Bulletin of the American Mathematical Society* 58 (1952), pp. 102–103.

[80] D. B. Bogy and E. Sternberg. “The effect of couple-stresses on the corner singularity due to an asymmetric shear loading”. In: *International Journal of Solids and Structures* 4.2 (1968), pp. 159–174.

[81] X. Markenscoff and M. Paukshto. “The wedge paradox and a correspondence principle”. In: *Proceedings of the Royal Society of London. Series A, Mathematical, Physical and Engineering Sciences* 454.1968 (1998), pp. 147–154.

[82] M. Hetényi. “A method of solution for the elastic quarter-plane”. In: *Journal of Applied Mechanics* 27.2 (1960), pp. 289–296.

[83] Z. Yosibash. “Asymptotic Solution at the Intersection of Circular Edges in a 2-D Domain”. In: *Singularities in Elliptic Boundary Value Problems and Elasticity and Their Connection with Failure Initiation*. New York: Springer, 2012, pp. 411–416.

[84] R. D. Gregory. “Green’s functions, bi-linear forms, and completeness of the eigenfunctions for the elastostatic strip and wedge”. In: *Journal of Elasticity* 9.3 (1979), pp. 283–309.

[85] A. E. Green and W. Zerna. *Theoretical Elasticity*. Courier Corporation, 1992.

[86] K. Bertram Broberg. *Cracks and Fracture*. Elsevier, 1999.

[87] G. C. Sih. “Some Basic Problems in Fracture Mechanics and New Concepts”. In: *Engineering Fracture Mechanics* 5.2 (1973), pp. 365–377.

[88] Grigory Isaakovich Barenblatt. “The Mathematical Theory of Equilibrium Cracks in Brittle Fracture”. In: *Advances in Applied Mechanics* 7 (1962), pp. 55–129.

[89] Yu. P. Zheltov and S. A. Khristianovitch. “On the Mechanism of Hydraulic Fracture of an Oil Bearing Stratum”. In: *Izvestiya Akademiia Nauk SSSR, Otd. Tekhn. Nauk* 5 (1955), pp. 3–41.

[90] E. Sternberg. “Load-transfer and load-diffusion”. In: *Proceedings of the Sixth U.S. National Congress of Applied Mechanics*. Cambridge, MA: ASME, New York, 1970.

[91] Derek Hull and David J Bacon. *Introduction to dislocations*. Vol. 37. Elsevier, 2011.

[92] O. C. Zienkiewicz and R. L. Taylor. *The Finite Element Method, Vol. 2*. New York: McGraw-Hill, 1991.

[93] Y. J. Liu et al. “Recent advances and emerging applications of the boundary element method”. In: *Applied Mechanics Reviews* 64.3 (2012), p. 030802.

[94] J. T. Chen and H. K. Hong. “Review of dual boundary element methods with emphasis on hypersingular integrals and divergent series”. In: *Applied Mechanics Reviews* 52.1 (1999), pp. 17–33.

[95] N. Nishimura. “Fast multipole accelerated boundary integral equation methods”. In: *Applied Mechanics Reviews* 55.4 (2002), pp. 299–324.

[96] A. H. D. Cheng and D. T. Cheng. “Heritage and early history of the boundary element method”. In: *Engineering Analysis with Boundary Elements* 29.3 (2005), pp. 268–302.

[97] C. A. Brebbia, J. C. F. Telles, and L. C. L. Wrobel. *Boundary Element Techniques: Theory and Applications in Engineering*. New York: Springer, 1984.

[98] M. A. Jaswon and H. Jones. “Integral equation methods in potential theory. I”. In: *Proceedings of the Royal Society of London. Series A, Mathematical and Physical Sciences* 275 (1963), pp. 23–32.

[99] G. T. Symm and H. Jones. “Integral equation methods in potential theory. II”. In: *Proceedings of the Royal Society of London. Series A, Mathematical and Physical Sciences* 275 (1963), pp. 33–46.

[100] T. A. Cruse and F. J. Rizzo. “A direct formulation and numerical solution of the general transient elastodynamic problem. I”. In: *Journal of Mathematical Analysis and Applications* 22.1 (1968), pp. 244–259.

[101] T. J. R. Hughes, J. A. Cottrell, and Y. Bazilevs. “Isogeometric analysis: CAD, finite elements, NURBS, exact geometry and mesh refinement”. In: *Computer Methods in Applied Mechanics and Engineering* 194.39 (2005), pp. 4135–4195.

[102] G. Beer, B. Marussig, and C. Dünser. *The Isogeometric Boundary Element Method*. Berlin/Heidelberg, Germany: Springer, 2020.

[103] T. Takahashi and T. Matsumoto. “An application of fast multipole method to isogeometric boundary element method for Laplace equation in two dimensions”. In: *Engineering Analysis with Boundary Elements* 36.12 (2012), pp. 1766–1775.

[104] A. I. Ginnis et al. “Isogeometric boundary-element analysis for the wave-resistance problem using T-splines”. In: *Computer Methods in Applied Mechanics and Engineering* 279 (2014), pp. 425–439.

[105] A. Aimi et al. “Efficient assembly based on B-spline tailored quadrature rules for the IgA-SGBEM”. In: *Computer Methods in Applied Mechanics and Engineering* 331 (2018), pp. 327–342.

[106] L. Coox et al. “An isogeometric indirect boundary element method for solving acoustic problems in open-boundary domains”. In: *Computer Methods in Applied Mechanics and Engineering* 316 (2017), pp. 186–208.

[107] C. Liu et al. “Shape optimization of sound barrier using an isogeometric fast multipole boundary element method in two dimensions”. In: *Engineering Analysis with Boundary Elements* 85 (2017), pp. 142–157.

[108] J. Dölz et al. “A fast isogeometric BEM for the three dimensional Laplace- and Helmholtz problems”. In: *Computer Methods in Applied Mechanics and Engineering* 330 (2018), pp. 83–101.

[109] T. Takahashi et al. “A framework of shape optimisation based on the isogeometric boundary element method toward designing thin-silicon photovoltaic devices”. In: *Engineering with Computers* 35.2 (2019), pp. 423–449.

[110] T. Takahashi et al. “An isogeometric boundary element method for three-dimensional doubly-periodic layered structures in electromagnetics”. In: *Engineering Analysis with Boundary Elements* 136 (2022), pp. 37–54.

[111] C. Xu et al. “RI-IGABEM based on generalized-α method in 2D and 3D elastodynamic problems”. In: *Computer Methods in Applied Mechanics and Engineering* 383 (2021), p. 113890.

[112] M. A. Scott et al. “Isogeometric boundary element analysis using unstructured T-splines”. In: *Computer Methods in Applied Mechanics and Engineering* 254 (2013), pp. 197–221.

[113] B. H. Nguyen et al. “Isogeometric symmetric Galerkin boundary element method for three-dimensional elasticity problems”. In: *Computer Methods in Applied Mechanics and Engineering* 323 (2017), pp. 132–150.

[114] Z. N. Ba, X. Gao, and V. W. Lee. “Scattering of plane P- and SV-waves by periodic topography: Modeled by a PIBEM”. In: *Engineering Analysis with Boundary Elements* 106 (2019), pp. 320–333.

[115] Y. Sun et al. “A numerical method for filtering the noise in the heat conduction problem”. In: *Mathematics* 7.6 (2019), p. 502.

[116] E. Klaseboer et al. “Eliminating the fictitious frequency problem in BEM solutions of the external Helmholtz equation”. In: *Engineering Analysis with Boundary Elements* 109 (2019), pp. 106–116.

[117] H. Zhang et al. “Scattering of elastic waves by a 3-D inclusion in a poroelastic half space”. In: *Engineering Analysis with Boundary Elements* 108 (2019), pp. 133–148.

[118] Y. Sun. “Indirect Boundary Integral Equation Method for the Cauchy Problem of the Laplace Equation”. In: *Journal of Scientific Computing* 71.2 (2017), pp. 469–498.

[119] L. Huang et al. “A three-dimensional indirect boundary integral equation method for the scattering of seismic waves in a poroelastic layered half-space”. In: *Engineering Analysis with Boundary Elements* 135 (2022), pp. 167–181.

[120] V. D. Kupradze. “A method for the approximate solution of limiting problems in mathematical physics”. In: *USSR Computational Mathematics and Mathematical Physics* 4.6 (1964), pp. 199–205.

[121] V. D. Kupradze and M. A. Aleksidze. “The method of functional equations for the approximate solution of certain boundary value problems”. In: *USSR Computational Mathematics and Mathematical Physics* 4.4 (1964), pp. 82–126.

[122] G. Fairweather and A. Karageorghis. “The method of fundamental solutions for elliptic boundary value problems”. In: *Advances in Computational Mathematics* 9.1–2 (1998), pp. 69–95.

[123] C. S. Chen, A. Karageorghis, and Y. S. Smyrlis. *The Method of Fundamental Solutions – A Meshless Method*. Dynamic Publishers, 2008.

[124] X.-C. Li and W.-A. Yao. “Virtual boundary element-integral collocation method for the plane magnetoelectroelastic solids”. In: *Engineering Analysis with Boundary Elements* 30.8 (2006), pp. 709–717.

[125] C. X. Bi et al. “Reconstruction and separation in a semi-free field by using the distributed source boundary point method-based nearfield acoustic holography”. In: *Journal of Vibration and Acoustics* 129.3 (2007), pp. 323–329.

[126] B. Pluymers et al. “Trefftz-based methods for time-harmonic acoustics”. In: *Archives of Computational Methods in Engineering* 14.4 (2007), pp. 343–381.

[127] Z. C. Li et al. “Trefftz, collocation, and other boundary methods – A comparison”. In: *Numerical Methods for Partial Differential Equations* 23.1 (2007), pp. 93–144.

[128] W. Chen and M. Tanaka. “A meshless, integration-free, and boundary-only RBF technique”. In: *Computers & Mathematics with Applications* 43.3–5 (2002), pp. 379–391.

[129] J. T. Chen et al. “Boundary collocation method for acoustic eigenanalysis of three-dimensional cavities using radial basis function”. In: *Computational Mechanics* 29 (2002), pp. 392–408.

[130] M. Wilm et al. “A full 3D plane-wave-expansion model for 1-3 piezoelectric composite structures”. In: *The Journal of the Acoustical Society of America* 112.3 (2002), pp. 943–952.

[131] W. Chen and F. Z. Wang. “A method of fundamental solutions without fictitious boundary”. In: *Engineering Analysis with Boundary Elements* 34.5 (2010), pp. 530–532.

[132] W. Chen, Z. J. Fu, and X. Wei. “Potential problems by singular boundary method satisfying moment condition”. In: *CMES-Computer Modeling in Engineering & Sciences* 54.1 (2009), pp. 65–85.

[133] M. Hatami. *Weighted Residual Methods: Principles, Modifications and Applications*. Academic Press, 2017.

[134] W. Chen and Y. Gu. “An improved formulation of singular boundary method”. In: *Advances in Applied Mathematics and Mechanics* 4.5 (2012), pp. 543–558.

[135] Y. Gu, W. Chen, and X. Q. He. “Improved singular boundary method for elasticity problems”. In: *Computers & Structures* 135 (2014), pp. 73–82.

[136] C. E. Inglis. “Some special cases of two dimensional stress and strain”. In: *Transactions of the Institution of Naval Architects* 64 (1922), pp. 253–258.

[137] T. C. T. Ting. “The wedge subjected to tractions: a paradox re-examined”. In: *Journal of Elasticity* 14.3 (1984), pp. 235–247.

[138] X. Markenscoff. “Some remarks on the wedge paradox and Saint-Venant’s principle”. In: *Journal of Applied Mechanics* 61.3 (1994), pp. 519–523.

[139] R. Fosdick and G. Royer-Carfagni. “Hadamard’s conditions of compatibility from Cesaro’s line-integral representation”. In: *International Journal of Engineering Science* 146 (2020), p. 103174.

[140] R. Fosdick and G. Royer-Carfagni. “Erratum to: Hadamard’s conditions of compatibility from Cesaro’s line-integral representation”. In: *International Journal of Engineering Science* 154 (2020), p. 103345.

[141] Wai-Fah Chen and Da-Jian Han. *Plasticity for Structural Engineers*. J. Ross Publishing, 2007.

[142] Olek C. Zienkiewicz and Robert L. Taylor. *The Finite Element Method for Solid and Structural Mechanics*. Elsevier, 2005.

[143] G. I. Barenblatt. *Scaling, Self-Similarity, and Intermediate Asymptotics: Dimensional Analysis and Intermediate Asymptotics*. 14. Cambridge University Press, 1996.

[144] G. I. Barenblatt and G. I. Sivashinsky. "Self-similar solutions of the second kind in the problem of propagation of intense shock waves: PMM vol. 34, n. 4, 1970, pp. 685–692". In: *Journal of Applied Mathematics and Mechanics* 34.4 (1970), pp. 655–662.

[145] G. I. Barenblatt and G. I. Sivashinsky. "Self-similar solutions of the second kind in nonlinear filtration: PMM vol. 33, n. 5, 1969, pp. 861–870". In: *Journal of Applied Mathematics and Mechanics* 33.5 (1969), pp. 836–845.

[146] Ian N. Sneddon. *Fourier Transforms*. New York-Toronto-London: McGraw-Hill Book Company, 1951.

[147] G. Royer-Carfagni and S. Zandekarimi. "The linear elastic wedge under a tip couple at the critical angle: Where is the paradox?" In: *Journal of Elasticity* 154.1–4 (2023), pp. 275–291.

[148] E. Cesàro. "Sulle formole del Volterra fondamentali nella teoria delle distorsioni elastiche". In: *Nuovo Cimento (1901–1910)* 12.1 (1906), pp. 143–154.

[149] W. V. Quine. "Paradox". In: *Scientific American* 206.4 (1962), pp. 84–99.

[150] J. D. Eshelby. "The Determination of the Elastic Field of an Ellipsoidal Inclusion, and Related Problems". In: *Proceedings of the Royal Society of London. Series A* 241.1226 (1957), pp. 376–396.

[151] E. Mann. "An Elastic Theory of Dislocations". In: *Proceedings of the Royal Society of London. Series A* 199.1058 (1949), pp. 376–394.

[152] D. A. Hills et al. *Solution of Crack Problems: The Distributed Dislocation Technique*. New York: Springer Science & Business Media, 1996.

[153] J. R. Barber. *Elasticity*. Dordrecht, The Netherlands: Kluwer Academic Publishers, 2002.

[154] J. Koehler. "Elastic Centers of Strain and Dislocations". In: *Journal of Applied Physics* 37.12 (1966), pp. 4351–4357.

[155] J. Dundurs. "Elastic Interaction of Dislocations with Inhomogeneities". In: *Mathematical Theory of Dislocations*. Ed. by T. Mura. New York: American Society of Mechanical Engineers, 1969, pp. 70–115.